Non-Invasive Electrocardiographic Imaging of Ventricular Activities

Data-Driven and Model-Based Approaches

Zur Erlangung des akademischen Grades eines

DOKTOR-INGENIEURS

von der Fakultät für

Elektrotechnik und Informationstechnik

des Karlsruher Instituts für Technologie (KIT)

genehmigte

DISSERTATION

von

Danila Potyagaylo, Dipl.-Math.

geb. in Krasnodar, Russland

Tag der mündlichen Prüfung:	14. Juli 2016
Referent:	Prof. Dr. rer. nat. Olaf Dössel
Korreferent:	Ass. Prof. Dr. Thom F. Oostendorp
	Prof. Dr. rer. nat. Friedrich K. Jondral

Acknowledgments

The research leading to this thesis has been conducted at the Institute of Biomedical Engineering, Karlsruhe Institute of Technology (KIT).

First of all, I owe to thank Prof. Dr. Olaf Dössel for giving me the opportunity to work in an excellent research environment and supporting my ideas and initiatives as well as for his continuous commitment to my project. I thank Dr. Thom Oostendorp for motivating collaborative work and his referee on this thesis. Furthermore, I would like to thank Prof. Dr. Friedrich Jondral for the interest in my work and for refereeing the thesis.

As I was lucky to be a part of a great team with a unique working culture of fostering the academic spirit, a number of people have contributed to my work. I would like to express my gratitude to Dr. Gunnar Seemann for technical discussions as well as for organizing multiple outdoor activities and sharing his rich personal experience. My deepest thanks go to Walther Schulze for introducing me to the field and for many adventures that we undertook together. For being great colleagues, I thank Axel Loewe, Tobias Oesterlein, Stefan Pollnow, Gustavo Lenis, Michael Kircher, Bhawna Verma, Jochen Schmidt, Lukas Baron, Markus Rottmann,Thomas Fritz, Matthias Keller, Mathias Wilhelms, David Keller, Tobias Baas, Martin Krüger, Oussama Jarrousse, Christopher Schilling, Julia Bohnert, Frank Weber, Irene Günter, Manfred Schroll, Ramona Modery, Charis Kahlmeyer and Dirk Falkenberg.

My further thanks go to Vynnie Kong, Antonia Reinke, Elisenda Gil Córtes and Max Segel for contributing to the present work through their own theses.

Without cooperation with the best people in the 'inverse' community this thesis could not have been possible. I would like to thank Thom Oostendorp, Peter van Dam and Arno Janssen from Radboud University Medical Center for excellent collaboration in the scope of source models. Many thanks go to Jaume Coll-Font, Burak Erem and Dana Brooks, Northeastern University, for the interesting scientific discussions and a joint project on spatio-temporal inverse methods. I also want to thank Matti Stenroos, Teijo Konttila and Ville Mäntynen from Aalto University and Hua Xiang, Wuhan University, for their efforts on Trilateral project.

For the financial support of the thesis, I wish to kindly thank the German Research Foundation (DFG). My further gratitude is expressed to the Karlsruhe House of Young Scientists (KHYS) for the networking scholarship.

I want to thank all my friends from Krasnodar for standing by me, even though we met seldom in the last years. Finally, I owe my warmest thanks to my family for believing in me

and supporting me throughout my studies as well as the course of this thesis. My deepest and greatest thanks go to my girlfriend Marie for her patience and support.

Contents

Zusammenfassung

Seit der Erfindung des ersten Elektrokardiographie-Geräts durch Willem Einthoven im Jahre 1903 wurden enorme Fortschritte sowohl im Bereich der theoretischen Bioelektrizität als auch bezüglich der technischen Entwicklung von Messinstrumenten erzielt. Mitte des letzten Jahrhunderts ermöglichten erste Computermodelle die numerische Berechnung der elektromagnetischen Felder im menschlichen Körper. Dieser Meilenstein in der Geschichte des EKG bildete den Ausgangspunkt für die fortlaufende Weiterentwicklung der computerbasierten Elektrokardiologie und somit für die Integration rechnergestützter Systeme in die klinische Praxis. Im klinischen Alltag kommt standardmäßig das konventionelle 12-Kanal-EKG zur Überwachung und Diagnostik von Herzerkrankungen zum Einsatz. In diesem Zusammenhang bietet die sogenannte EKG-Bildgebung (ECG Imaging) basierend auf dem inversen Problem der EKG vielfältige Möglichkeiten für präinterventionelle Behandlungsstrategie- und Therapie-Planung. Unter Verwendung patientenspezifischer Körpermodelle aus bildgebenden Verfahren wie MRT oder CT kann beispielsweise eine Echtzeit-Überwachung der Schlag-zu-Schlag-Variabilität anhand nichtinvasiv erstellter, hochaufgelöster Maps der elektrischen Potentiale durchgeführt werden. Jedoch ist das der EKG-Bildgebung zugrundeliegende mathematische Problem schlecht gestellt und erfordert folglich die Anwendung spezieller Regularisierungstechniken. Diese lassen sich in daten- und regelbasierte Algorithmen unterteilen. Während datenbasierte Methoden den Fehler zwischen simulierten und gemessenen EKG-Signalen durch „intelligente“ Invertierung der Übertragungsmatrix minimieren, passen regelbasierte Algorithmen ein Modell an die Ausbreitung der elektrischen Depolarisierung im Herzen an und erfassen so das gesamte zeitliche Muster. Die vorliegende Arbeit beleuchtet ausgewählte Aspekte der Vorwärtsmodellierung, so zum Beispiel die Simulation von Elektro- und Magnetokardiogrammen im Falle einer elektrisch stillen Ischämie sowie die Anpassung der elektrischen Potentiale unter Variation der Leitfähigkeiten. Besonderer Fokus liegt auf der Entwicklung neuer Regularisierungsalgorithmen sowie der Anwendung und Bewertung aktuell verwendeter Methoden in realistischen in silico bzw. klinischen Studien. Darüber hinaus werden Ansatzpunkte und Strategien bzgl. Weiterentwicklung und Forschung im Bereich der EKG-Bildgebung erörtert.

Contents

List of Abbreviations

AP	action potential
AT	activation times
BEM	boundary element method
BSPM	body surface potential maps
CC	correlation coefficient
CT	computed tomography
CV	conduction velocity
ECG	electrocardiogram
ECGI	electrocardiographic imaging
EDL	equivalent dipole layer
EP	epicardial potentials
FEM	finite element method
FRA	fastest route algorithm
KCL	King's College London
KMF	Kozlov-Mazya-Fomin
LAT	local activation time
LV/RV	left/right ventricle
LVOT/RVOT	left/right ventricular outflow tract
MAP	maximum-a-posteriori method
MRI	magnetic resonance imaging
NP	nondeterministic polynomial time
PVC	premature ventricular contraction
TMP	transmembrane potentials
TMV	transmembrane voltages
UMM	University Medical Center Mannheim
VT	ventricular tachycardia

CHAPTER 1

Introduction

Since the invention of an applicable ECG device by Willem Einthoven in 1903, tremendous progress has been made in comprehension of bioelectricity principles and technical development of measurement equipment. In the middle of past century, first computer models of a human body were created for numerical calculations of electromagnetic fields. This set up a milestone for ongoing evolution of computational electrocardiology, whose significance can hardly be overestimated.

After then, integration of computer-based models and computer-assisted systems into the clinical care has commenced. Nevertheless, conventional ECG remains a prevalent tool for monitoring and diagnostic of heart condition in the everyday practice. With this regard, vast opportunities for preinterventional decision making and treatment planning could be provided by noninvasive electrocardiographic imaging (ECG imaging), also called ECGI or inverse problem of ECG. Once a patient-specific torso model is obtained from magnetic resonance or computer tomography images, ECG imaging would enable real-time monitoring of beat-to-beat variations facilitated by noninvasively obtained cardiac maps with spatial resolution much higher than provided by current state-of-the-art modalities.

Despite variety of existing inverse schemes, they could be classified into two big branches: Data-driven approaches estimate cardiac sources by minimizing the misfit between measured and predicted ECG. Physiological solution properties can be introduced into the problem by means of constrained optimization. The second group consists of methods employing a realistic propagation model for calculating a reliable solution estimate.

The major goal of this thesis is to design new inverse algorithms, evaluate current state-of-the-art data-driven and model-based techniques both in realistic *in silico* scenarios and clinical context as well as outline strategies for further improvements in ECG imaging.

1.1 Structure of Thesis

Part I - Fundamentals

- **Chapter 2** provides a brief introduction into cardiac anatomy and electrophysiology and describes medical motivation of the present work.

- **Chapter 3** outlines basic ideas of biophysical heart modeling and introduces numerical methods of field calculations.
- **Chapter 4** gives an overview of current state-of-the-art approaches in ECG imaging.

Part II - Projects

- **Chapter 5** presents a simulation study case on performance of magnetocardiography for detection of an electrically silent ischemia.
- **Chapter 6** introduces a novel method for estimating ECG changes due to variations in electrical conductivity values.
- **Chapter 7** examines the performance of the model-based fastest route algorithm (FRA) in presence of modeling errors in the description of volume conductor model for localization of extrasystoles starting on the ventricular heart surface.
- **Chapter 8** outlines a simulation setup for generating realistic ectopic activation sequences.
- **Chapter 9** presents the proposed methods for solving the inverse problem of ECG and examines their performance for localization of simulated premature ventricular contractions (PVC).
- **Chapter 10** analyzes the influence of cardiac anisotropy on ECG imaging. Reconstructions are performed by FRA and a data-driven constraint optimization algorithm imposing nondecreasing temporal behavior on the transmembrane potentials (TMP).
- **Chapter 11** evaluates the performance of these two spatio-temporal approaches for localization of ventricular pacings and PVC in five patients.
- **Chapter 12** introduces an extensive scar region into the PVC simulation study leading to violation of the underlying source model assumptions. Localization results for both model-based (FRA) and data-driven (constrained optimization) approaches are analyzed in dependence on earliest excitation site relative to the scar position.
- **Chapter 13** presents the results of noninvasive imaging for a clinical case of sustained monomorphic ventricular tachycardia.

At the end, a summarizing discussion is provided and an outlook for future directions in ECG imaging is given.

PART I

FUNDAMENTALS

CHAPTER 2

Medical Fundamentals

In this chapter, cardiac anatomy as well as fundamental electrophysiological properties of the heart are recalled. Furthermore, medical motivation for noninvasive ECG imaging in general and this thesis in particular is provided.

2.1 Human Heart

2.1.1 Anatomical Overview

The heart is a hollow muscular organ controlling the blood flow in a human body. In Fig. 2.1, four heart chambers, - the left and right atrium and the left and right ventricle, - along with the blood vessels and valves enforcing unidirectional blood flow between them are visualized. Whereas the mitral valve connects the left atrium and left ventricle, the right atrium and right ventricle are separated by the tricuspid valve. The superior and inferior venae cava are connected to the top and bottom of the right atrium, respectively. The left pulmonary veins drain into the left atrium. The right ventricle is connected to the pulmonary artery via the pulmonary valve, while the aortic valve separates the left ventricle from the aorta.

The cardiac wall consists of three different layers of tissue. The endocardium is covering the inner surface of the heart. Thick myocardium is essential for the contraction function and the epicardium is lining the outer heart surface [1]. The complete heart is surrounded by a membranous sac called pericardium.

2.1.2 Circulatory System

The circulatory system including heart and blood vessels transports oxygen to the organs and transfers nutrients, hormones and other biochemical essential substances between them. Concurrently, carbon dioxide is carried back to the lungs. At the end of diastole, deoxygenated blood supplied to the right atrium through superior or inferior vena cava from peripheral circulation is pumped to the right ventricle. Simultaneously, the oxygen-rich blood that entered the left atrium through one of the four pulmonary veins pours into the left ventricle. Within the following systole, the mitral and tricuspid valves between atria and ventricles

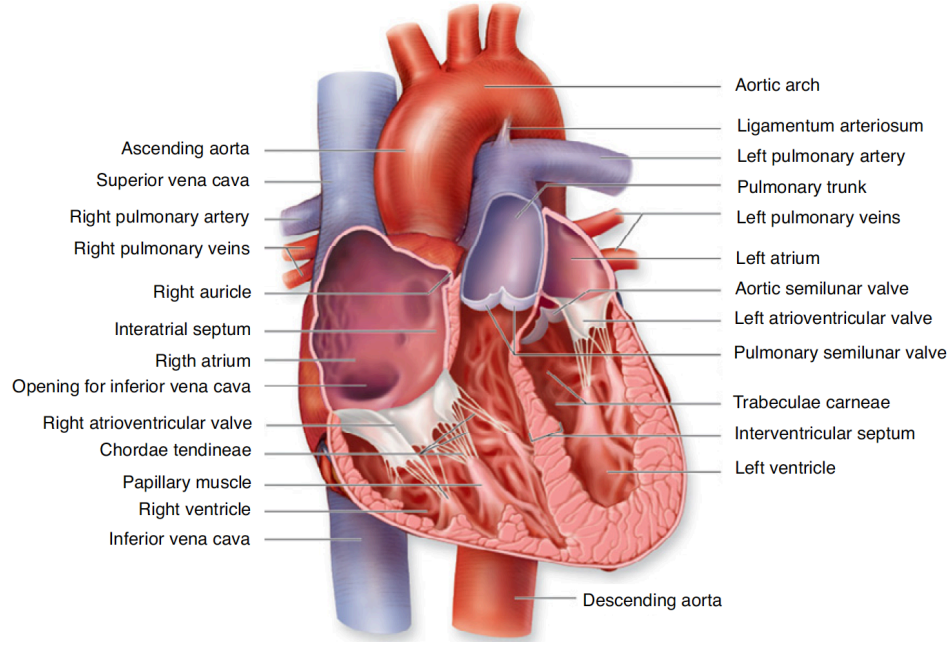

Figure 2.1: Four chamber of the human heart with blood vessels and valves. The figure is reprinted from [2] under the Creative Commons licence http://creativecommons.org/licenses/by-nc-nd/3.0/de/.

close, pressure in the ventricles increases until it succeeds the threshold for blood to be ejected into aorta and pulmonary artery from left and right heart chambers, respectively. During the subsequent diastole, the atria and ventricles are filled with blood and the described circulatory cycle is repeated [1].

2.1.3 Basics of Cardiac Cellular Electrophysiology

The cardiac myocytes are surrounded by a bilayer cell membrane that separates them from extracellular milieu and contains distinct proteins serving as permeable pathways for ionic exchange. Activity of these transport proteins results in ion concentration gradients across the membrane that lead to the difference in electric potentials called transmembrane voltage (TMV), or transmembrane potential (TMP) [3]. Furthermore, the regulation process of opening and closing the ion channels, which is called gating, is dependent on the state of TMV and adjusts the ionic conductance corresponding to its value.

In resting state, the difference between potentials in intra- and extracellular domains constitutes approximately -90 mV. However, the cardiac cells are electrically excitable and the TMV value exhibits temporal changes due to a complex intercourse between passive and active ion transport proteins, which is briefly explained in the following. A characteristic time course of TMV is shown in Fig. 2.2. First, an action potential is triggered either by an adjacent excited cell or, in case of a pacemaker cell, by a drift of the membrane voltage. At the depolarization phase, positively charged sodium ions rapidly flow into the cell leading to a positive overshoot of the transmembrane voltage. The time instance of the steepest TMV upstroke is called activation, or depolarization, time. Afterwards, the sodium channels close,

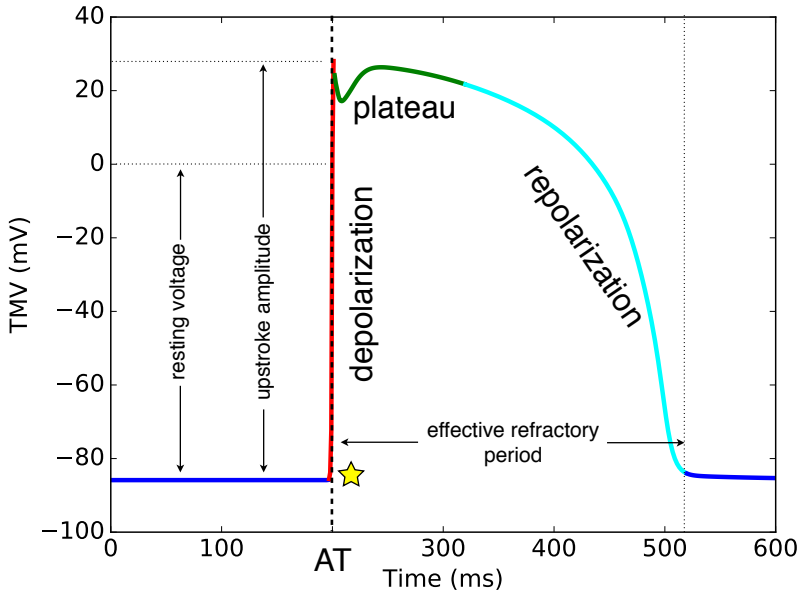

Figure 2.2: Temporal course of a transmembrane voltage (TMV). Depolarization phase is also called upstroke. The time instance corresponding to the steepest TMV increase is also known as activation time (AT).

while an increase in the calcium conductivity maintains a near constant value of TMV for the time period known as plateau phase. Repolarization phase is featured by closing of calcium and opening of potassium channels causing outflow of positively charged potassium ions. Therewith, an initial negative value of the TMV is achieved. After depolarization, the cell remains in an unexcitable state for a period called refractory time [4].

2.1.4 Excitation Conduction System

Cardiac cells are internally electrically coupled by gap junctions, which enables generation of an organized excitation wavefront. Under normal conditions, depolarization starts in the sinus node situated in the right atrium. From there, excitation spreads over the both atria initiating their contraction. After a delay necessary for completion of atria contraction [1], the depolarization wave arrives to the atrioventricular node transferring excitation through the bundle of His, left and right bundle branches and Purkinje network to the ventricular myocardial cells [2].

2.2 Medical Basics

2.2.1 Electrocardiogram

Cardiac excitation gives rise to an electric field that can be measured on the body surface as electrocardiogram (ECG). In clinical routine, mostly the 12-lead ECG system containing

bipolar (Einthoven) and unipolar (Goldberg and Wilson) leads is used for noninvasive assessment of heart function [5]. However, more comprehensive and diagnostically relevant information can be obtained with multi-channel recording systems [6, 7]. In this case, the resulting signals on the body surface are denoted as body surface potential maps (BSPM). In the context of ECG imaging, BSPM systems are usually favored over the standard 12-lead. Available commercial systems for solving the ECG inverse problem utilize electrode vests containing about 250 leads [8, 9].

2.2.2 Ventricular Arrhythmia

Ventricular arrhythmias is a major cause of sudden cardiac death worldwide. In case of premature ventricular contraction (PVC), or extrasystole, the mechanism of electrical currents depolarizing both ventricles is distorted. PVCs are irregular extra beats (contractions), interrupting the normal heart rhythm and occurring when the propagation starts from a ventricular site distinct from a normal heartbeat trigger, sinoatrial node. Patients with structural heart disease suffering from frequent extrasystoles belong to a group with increased risk of sudden cardiac death.

Ventricular tachycardia (VT), another life-threatening arrhythmia, that results in regular repetitive fast heart rhythm can trigger even more lethal ventricular fibrillation (VF). There is a broad spectrum of ventricular arrhythmias symptoms varying from chest pain, palpitations, dyspnoea, dizziness and syncope to cardiac arrest.

VTs are classified based on its cause, duration and corresponding ECG features. VT could take an idiopathic form, but in most of the cases it is associated with structural heart disease.

Based on VT duration, one distinguishes between non-sustained VT (self-terminates within 30 sec) and sustained VT that lasts more than 30 sec and could be also self-terminated.

Depending on the ECG morphology, VT can be classified as monomorphic and polymorphic. Monomorphic VT has the same ECG characteristics in all leads for consecutive beats and is mostly caused by myocardial scarring. The border zone between the scar and healthy tissue possesses abnormal electrophysiological and structural properties. It is known to contribute to scar related arrhythmias and is the target for catheter ablation. Polymorphic VT has beat-to-beat variations in ECG, its QRS complexes twist around the baseline, which is reason it is sometimes called torsades de pointes tachycardia. This type of VT is associated with a prolonged QT interval and could be both congenital or acquired.

Treatment of VT aims at both terminating an episode of the present arrhythmia and at arrhythmia suppression in the future. Clinical management strategy depends on various factors such as VT symptoms, resistivity to medicaments and comorbidities. Long-term anti-arrhythmic medication is frequently avoided due to severe side-effects. Unstable VT patients experience hemodynamic decompensation and thus require an implantable cardioverter defibrillator (ICD). Patients with previous cardiac arrest due to VT or VF and stable VT patients with a small ejection fraction are also subject to ICD. As stable scar associated

VT tends to deteriorate into unstable states, these cases are treated in clinical practice with catheter radio-frequency ablation (RFA) destroying abnormal pathways.

Success rate of such intervention procedure directly relies on the knowledge about scar position, its electrophysiological properties and excitation origin of abnormal ventricular beats. In order to obtain a 3-D view of heart anatomy and track the catheter during an ablation, electroanatomic mapping systems (EnSite NaVx (St. Jude Medical) or CARTO (Biosense Webster)) are used in the clinic.

2.2.3 Clinical Motivation

Catheter ablation is an effective treatment of ventricular arrhythmia in general, and ectopic beats in particular. In clinical environment, this procedure is performed based on qualitative analysis of the standard 12-lead ECG. First, location of a PVC is estimated according to the existing protocols without taking individual anatomical differences into account. Then, catheter pacings are performed in the target area, while being successively corrected based on the match of ECG originating from paced sequences and the sought arrhythmia.

Motivation of this work is to assess performance of noninvasive ECG imaging for guiding ablation procedures in patient-specific manner. By means of the inverse solutions, three-dimensional maps of cardiac excitation propagation could be generated for improved estimation of the ablation target. Therewith, significant reduction would be achieved for procedure time as well as involved costs and mental burden of the invasive treatment. In addition, the success rate can be increased.

CHAPTER 3

Biophysical and Mathematical Fundamentals

In this chapter, biophysical principles underlying forward ECG calculations are introduced. Monodomain and bidomain models for generating realistic cardiac activation sequences and corresponding transmembrane voltages are shortly recapitulated. Then, the problem of finding electric potentials in body volume is formulated as a set of differential equations. Finally, two numerical methods of electromagnetic field calculations, finite element and boundary element method, are described.

3.1 Monodomain and Bidomain Models

Monodomain and bidomain models are employed for simulating the cardiac excitation propagation. Originally, the bidomain model was proposed by Tung in his PhD thesis [10]. It assumes presence of two homogeneous interpenetrating macroscopic domains in the heart, the extra- and intracellular spaces. At each point, anisotropic conductivity tensors σ_e and σ_i are defined for both domains. Furthermore, a current per volume I_{im} is allowed to flow from one domain to another [4]. It is assumed that all currents leaving one domain enter the other. Thereby, the current densities $\mathbf{J_e}$ and $\mathbf{J_i}$ for extra- and intracellular spaces satisfy the following equations:

$$\nabla \cdot \mathbf{J_e} = \quad \nabla \cdot (\sigma_e \nabla \phi_e) = \quad I_{im} \tag{3.1}$$

$$\nabla \cdot \mathbf{J_i} = \quad \nabla \cdot (\sigma_i \nabla \phi_i) = \quad -I_{im} \tag{3.2}$$

which is equivalent to the conservation of charge and reads as

$$\nabla \cdot (\mathbf{J_e} + \mathbf{J_i}) = 0 \tag{3.3}$$

$$\Leftrightarrow \nabla \cdot (\sigma_e \nabla \phi_e + \sigma_i \nabla \phi_i) = 0 \tag{3.4}$$

Defining the transmembrane voltage (TMV), or transmembrane potential (TMP), as $V_m = \phi_i - \phi_e$, one can combine (3.2) and (3.4) to obtain a coupled system of equations for V_m and

ϕ_e [3]:

$$\nabla \cdot (\sigma_i \nabla V_m) + \nabla \cdot (\sigma_i \phi_e) = I_{im} \tag{3.5}$$

$$\nabla \cdot ((\sigma_i + \sigma_e) \nabla \phi_e) = -\nabla \cdot (\sigma_i \nabla V_m) \tag{3.6}$$

For determining the impressed current density I_{im}, an electrophysiological cell model should be used. In the present work, a ventricular cell model by ten Tusscher *et al.* [11] was employed. As the bidomain model considers geometrical heart space as continuous media rather than cell objects, a factor β accounting for cells volume to surface ratio and converting the cellular discrete ionic and capacitive currents into a current per volume density needs to be introduced [4, 12]:

$$I_{im} = \beta (C_m \frac{dV_m}{dt} + I_{ion}) + I_{ex} \tag{3.7}$$

where I_{ex} accounts for externally injected currents. With a simplifying assumption of intracellular conductivity being a scalar multiplicative of the extracellular one $\sigma_i = \alpha \sigma_e$, the bidomain equations (3.5), (3.6) can be merged:

$$\frac{1}{1+\alpha} (\nabla \cdot (\sigma_i \nabla V_m)) = I_{im} \tag{3.8}$$

The model described by this equation is called monodomain model. In [13], the monodomain model was shown to produce realistic activation patterns almost indistinguishable from the bidomain calculations but at lower computational costs.

Software Framework *acCELLerate* The software framework *acCELLerate* is a modular simulation environment for electrophysiological cardiac modeling in general and solving the bidomain equations (3.8) in particular. For the detailed description of the framework, reader is referred to [14]. This environment includes the considered ten Tusscher ventricular cell model as well as several other models that have been adapted to experimental data stemming from different mammals.

3.2 Finite-Element Method

Once cardiac TMV distributions V_m are calculated, one arrives at the following Poisson equation for electrical potentials ϕ within the body volume conductor:

$$\nabla \cdot ((\sigma_e + \sigma_i) \nabla \phi) = -\nabla \cdot (\sigma_i \nabla V_m) \quad \text{in the whole volume} \tag{3.9}$$

$$\sigma_t \frac{\partial \phi}{\partial n} = 0 \quad \text{on the torso surface} \tag{3.10}$$

Furthermore, when the sources are expressed in terms of V_m, a reference electrode or linear combination of electrodes potentials, e.g. Wilson central terminal, must be specified. In the static formulation, i.e. when the sources are computed beforehand, the following currents continuity on the heart surface holds

$$(\sigma_e + \sigma_i) \frac{\partial \phi}{\partial n} = \sigma_t \frac{\partial \phi}{\partial n} \tag{3.11}$$

with σ_t standing for extracellular conductivity in the torso.

In the volume conductor outside the heart, distributions of electric potentials can be described by the Laplace equation:

$$\nabla \cdot (\sigma \phi) = 0 \tag{3.12}$$

where σ is the conductivity profile of all internal tissue types.

In the following text, a solution procedure for (3.9) is recapped. First, the volume domain is discretized. Then, the solution is approximated by $\phi = \sum_{i=1}^{N} \alpha_i$, where N is the number of discretization points and α_i are the shape functions. In the present work, linear tetrahedral elements were used. Recall the weak formulation of an elliptic differential equation

$$\int_\Omega \nabla \cdot (\sigma \nabla \phi)\, \omega \, d\Omega = \int_\Omega f\, \omega \, d\Omega \tag{3.13}$$

where $\sigma = \sigma_e + \sigma_i$, $f = -\nabla \cdot (\sigma_i \nabla V_m)$ and ω is an arbitrary test function. Applying the divergence theorem to the term on the left-hand side, one gets

$$\oint_\Gamma \omega(\sigma \nabla \phi) \cdot dS - \int_\Omega (\sigma \nabla \phi) \cdot \nabla w \, d\Omega = \int_\Omega f w \, d\Omega \tag{3.14}$$

Due to the Neumann boundary condition (3.10), the first surface integral is vanishing. In solving the remaining part for ϕ, the Galerkin method can be used. According to his idea, the test functions ω are chosen from the basis function space α_i. Therewith, for $j = 1, \ldots N$

$$\int_\Omega (\sigma \nabla \sum_{i=1}^{N} \phi_i \alpha_i) \cdot \nabla \alpha_j \, d\Omega = \int_\Omega (\sigma \sum_{i=1}^{N} \phi_i \nabla \alpha_i) \cdot \nabla \alpha_j \, d\Omega$$

which results in

$$\sum_{i=1}^{N} \left(\int_\Omega \sigma (\nabla \alpha_i) \cdot \nabla \alpha_j \, d\Omega) \right) \phi_i = \int_\Omega f \alpha_j \, d\Omega \tag{3.15}$$

Assuming α_i to be linear locally defined functions, one arrives at a big sparse system of linear equations that can be efficiently solved by iterative methods [15].

3.3 Boundary Element Method

For the boundary element method, only the surfaces separating areas with different conductivity values are discretized. In a general situation of N_s nested compartments, the potential inside the respective part k is given by

$$\Phi_k(\mathbf{r}') = \frac{\sigma_s}{\sigma_k^-} \Phi_\infty(\mathbf{r}') - \frac{1}{4\pi} \sum_{l=1}^{N_s} \frac{\sigma_l^- - \sigma_l^+}{\sigma_k^-} \int_{S_l} \Phi(\mathbf{r}) d\omega \tag{3.16}$$

where σ_s is the conductivity of the source region ($\sigma_s = \sigma_k^-$), $d\omega = d\omega(\mathbf{r}', \mathbf{r})$ is the solid angle [16], which is formally defined as

$$d\omega = \nabla \frac{1}{|\mathbf{r} - \mathbf{r}'|} \cdot d\mathbf{S}_l.$$

In the discretized form, $\tilde{\omega}_{i,j}^{k,l}$ corresponds to the solid angle subtended by node i on surface S_k by the triangles on S_l that have node j as a vertex.

Although the expression (3.16) enables calculation of the potential throughout the complete volume conductor, the potentials on the surfaces need to be computed first. For this purpose, field points are moved from inside towards each of the surface interfaces and the resulting integral equations are solved numerically.

Note that after discretization of the involved integrals special care should be taken when computing the 'auto solid angles' $\tilde{\omega}_{i,i}^{l,l}$. As the total solid angle subtended by S_l at any interior point is equal to -4π, the following expression holds

$$\tilde{\omega}_{i,i}^{l,l} = -4\pi - \sum_{n\neq i=1}^{V_l} \tilde{\omega}_{i,n}^{l,l}.$$

On the other hand, for parts of S_l that are approximately planar this value is close to -2π:

$$\tilde{\omega}_{i,i}^{l,l} = -2\pi + \delta_{i,i}$$

with $|\delta_{i,i}|$ being much smaller that 2π.

Therefore, for numerical handling of (3.16) a constant $-\frac{-2\pi}{4\pi}$ scaled by $\frac{\sigma_l^- - \sigma_l^+}{\sigma_l^-}$ is moved from the respective 'auto solid angle' $\tilde{\omega}_{i,i}^{l,l}$ to the left hand side first. After rearranging the terms, one arrives at the final BEM expression for treating the situation of an inhomogeneous volume conductor [16]:

$$\phi_i^k = 2\frac{\sigma_s}{\sigma_k^- + \sigma_k^+}\phi_{i;\infty}^k - \frac{1}{2\pi(\sigma_k^- + \sigma_k^+)} \sum_{l=1}^{N_s} (\sigma_l^- - \sigma_l^+) \sum_{j=1}^{K_l} \phi_j^l \tilde{\omega}_{i,j}^{k,l} \tag{3.17}$$

where K_l is the number of vertexes on surface S_l. A general expression for the potential ϕ^∞ generated by the given sources in an infinite homogeneous medium with conductivity σ_s reads as follows:

$$\phi^\infty = \frac{1}{4\pi\sigma_s} \int_{V_h} \frac{\mathbf{J}^\mathbf{i} \cdot (\mathbf{r} - \mathbf{r}')}{|\mathbf{r} - \mathbf{r}'|^3} dV_h. \tag{3.18}$$

In the forward ECG modeling, the primary impressed sources are expressed in terms of V_m:

$$\mathbf{J}^\mathbf{i} = -\sigma_i \nabla V_m \tag{3.19}$$

Upon the assumption of equal anisotropy ratios in the intra- and extracellular spaces, the following formula for electric potentials can be obtained [17]:

$$\phi_i^k = -\frac{\sigma_i}{2\pi(\sigma_k^- + \sigma_k^+)} \sum_{j=1}^{K_h} (V_m)_j \tilde{\omega}_{i,j}^{k,h} - \frac{1}{2\pi(\sigma_k^- + \sigma_k^+)} \sum_{l=1}^{N_s} (\sigma_l^- - \sigma_l^+) \sum_{j=1}^{K_l} \phi_j^l \tilde{\omega}_{i,j}^{k,l} \tag{3.20}$$

with S_h being the heart surface and K_h the number of its vertices.

In this formulation, the electrocardiograms on the torso surface are related to the surface V_m and not to actual volumetric sources given by ∇V_m.

Assembling the terms in (3.20)

$$\begin{aligned} \phi_i &= \phi_i^k, \\ g_i &= 2\frac{\sigma_s}{\sigma_k^- + \sigma_k^+}\phi_{i;\infty}^k, \\ b_{i,j} &= -\frac{1}{2\pi}\frac{\sigma_l^- - \sigma_l^+}{\sigma_k^- + \sigma_k^+}, \end{aligned}$$

a system of linear equations can be established:

$$\phi = g + B\phi \tag{3.21}$$

where B is solely determined by the volume conductor properties and g is set up by the current source as well as by the properties of the volume conductor [18]. As the potential caused by a current source is determined up to a constant, therewith associated system (3.21) is singular, which can be handled by a technique called deflation [19].

Defining $A = I - B$, the resulting set of equations

$$A\phi = g \tag{3.22}$$

can be efficiently solved by a direct inversion of A [18, 20]. Once A^{-1} reflecting exclusively the properties of the volume conductor is found, the potential ϕ caused by any source configuration g can be easily computed as

$$\phi = A^{-1}g \tag{3.23}$$

With regard to the surface transmembrane voltages, there is a closely related source model called equivalent dipole, or double, layer (EDL) [21–23]. Within the EDL model, surface sources are represented by a dipole layer whose strength stems from the amplitude of TMP upstroke scaled by a factor of $\sigma_i/(\sigma_i + \sigma_e)$. Whereas the surface TMP experiences a jump of approximately 100 mV, the scaled EDL strength varies from 0 to 1. Otherwise, these two models are mathematically equivalent and these terms will be used interchangeably further in text, when no explicit constraints are imposed on the TMP.

CHAPTER 4

State-of-the-Art in Inverse Problem of ECG

This chapter introduces the inverse problem of ECG, regularization concept and current state-of-the-art techniques in ECG imaging.

4.1 Inverse Problem of ECG

In the previous chapter, numerical methods for solving the forward problem of ECG were examined. Due to linearity of an underlying elliptic differential equation, a linear relation between the potential-based cardiac sources and corresponding ECG can be established:

$$Ax = y \tag{4.1}$$

where A is the so-called lead-field, or transfer, matrix, x are the sources and y are the resulting body surface potential maps (BSPM). Despite deceptive simplicity of this matrix equation, attenuating effects of the human body volume conductor and high solution sensitivity with respect to modeling and measurement noise impede direct inversion of the matrix A. Due to these violations of well-posedness criteria due to Hadamard [24], noninvasive calculation of cardiac sources from BSPM falls into category of ill-posed problems and should be treated by a mathematical technique called regularization. A classical Tikhonov method for overcoming numerical instabilities due to matrix inversion consists in minimizing misfit between measured and predicted ECG while forcing desired solution properties:

$$x = \operatorname{argmin}\{\|Ax - y\|_2^2 + \lambda \|Lx\|_2^2\} \tag{4.2}$$

where L is the regularization operator, which is usually assumed to be an identity, gradient or second-order derivative matrix. With a little algebraic effort, one can show that resulting solution x belongs to kernels intersection of operators A and L and is, thereby, influenced by choice of the latter.

Several source models exist for description of cardiac electrical activity: epicardial potentials [25], epi- and endocardial potentials, surface transmembrane voltages [17], equivalent

dipole layer model [22, 23], volumetric transmembrane voltages [15, 26], current densities [27]. Activation times, though not being a physical source, represent wavefront propagation properties bearing information relevant for planning of ablation procedures. Furthermore, every source unit follows certain physiological behavior during depolarization phase that favors specific regularization approaches taking these peculiarities into account [28–36].

Apart from one method proposed in Chapter 9, within the scope of this thesis the inverse problem of ECG was solved for surface transmembrane potentials. In the following, state-of-the-art methods for ECG imaging used in the present work are outlined.

4.2 Constrained Optimization Algorithm Forcing Nondecreasing Behavior of TMV

Within this formulation, TMV is assumed to be a monotonic nondecreasing function in temporal domain [37]. Furthermore, inequality constraints on lower and upper bounds, l and u, respectively, are introduced for all cardiac nodes. Therewith, effects of the TMV slight decrease immediately after the upstroke as well as subsequent plateau phase are neglected for reconstruction of depolarization sequences. Then, the resulting optimization scheme can be written as follows:

$$
\begin{aligned}
x &= \min_{x} \; ||\,|A\mathbf{x} - y||_2 + \lambda\,||L\mathbf{x}||_2 \\
\text{subject to} \quad & \begin{bmatrix} x_1 \\ x_1 - x_2 \\ \vdots \\ x_{T-1} - x_T \\ x_T \end{bmatrix} \leq \begin{bmatrix} -lb \\ 0 \\ \vdots \\ 0 \\ ub \end{bmatrix}
\end{aligned}
\tag{4.3}
$$

where T is the number of time steps. For this work, constraints l, u were assumed to take values of -80 and 20 mV for resting and depolarized phases, respectively.

As the size of problem (4.3) grows quadratically with number of unknowns, this optimization approach rapidly becomes computationally infeasible for increasing resolution in spatial and temporal domains. Therefore, dimensionality reduction should be performed for this regularization scheme to become practical. Resulting computational complexity can be reduced in two ways: in spatial and temporal domains. With this regard, effects of temporal dimensionality reduction on the localization accuracy of PVC were investigated in [38]. Downsampling in time with rates of 1, 1/2, 1/5, 1/10 was investigated. The study revealed robustness of reconstruction results with respect to different sampling strategies, whereas computational costs could be decreased significantly. Based on these observations, each 8th time instance within a QRS complex was taken for solving the problem (4.3). The specified sampling rate was found to be a reasonable trade-off between computational burden and the spatial resolution (typically 6-10 mm) on the cardiac meshes used.

4.3 Fastest Route Algorithm and Nonlinear Problem of Activation Times Imaging

Assuming a uniform TMV waveform morphology typically modeled by a sigmoidal function exhibiting a step-like behavior [30, 39, 40], activation time is referred to as the time of upstroke occurrence. Having established a relationship between AT and a predefined TMV template, one arrives at a nonlinear problem for noninvasive estimation of AT from body surface potential maps. As shown in [40], this problem manifests in presence of multiple local minima making its final solution to be highly susceptible against the initialization. In recent studies, fastest route algorithm has been reported to provide an effective physiologically meaningful initialization for the following nonlinear optimization [30, 40–44].

Fastest route algorithm (FRA) is a rule-based approach for calculating the shortest travel time between any pair of nodes on the heart surface that can be regarded as a fully connected graph. In the presented implementation, each node could be reached along a graph edge, whereas edges were defined not only as triangle edges on the heart surface but were also referred to transmural links as long as the line connecting endocardial and epicardial nodes lied entirely within the myocardium [30].

Provided the graph connectivity matrix, travel times between nodes i and j connected by an edge are calculated as:

$$t_{i,j} = \frac{d_{i,j}}{v_{i,j}}$$

where $d_{i,j}$ is the euclidean distance between the nodes, $v_{i,j}$ is the conduction velocity along the edge. In order to account for anisotropic wave propagation, two types of conduction velocities were assumed: along the ventricular surface and in direction transmural to it, v_l and v_t, respectively, whilst the former was set to be twice higher as the latter. Based on simple geometric relations, travel times for edges not strictly orthogonal to the heart surface can be calculated as follows [30]:

$$t_{i,j} = \sqrt{\frac{d^2}{v_l^2} + \frac{h^2}{v_t^2}}$$

where d and h are the lengths of edge projections on vectors along the cardiac surface and normal to it. Subsequently, the shortest travel time between each pair of nodes can be computed with the Dijkstra's algorithm. The results constitute a square symmetric matrix T whose entries $T_{i,j}$ could be regarded as activation times of nodes j for a depolarization wave starting from node i. Based on this observation, a full-search is designed for estimation of an ectopic beat origin. Within this scheme, each activation sequence due to node i is scaled to match the measured QRS duration and, afterwards, converted to an ECG signal that is compared to the reference potentials. An initial estimate for subsequent nonlinear optimization is provided, then, by an activation sequence exhibiting the highest correlation between forward calculated and measured signals.

4.4 Estimation of Activation Times from Calculated Potentials

Having inversely calculated potential-based sources, activation patterns playing an important role in clinical electrophysiology should be estimated. For a specific application of PVC ablation, the major challenge consists in identification of earliest excitation site from smooth noninvasively imaged solutions. Although algorithms calculating AT as time points corresponding to most positive/negative temporal derivative of TMV/EP generally perform well, in some cases no clear change in the reconstructed potentials' morphology could be observed. However, depolarization is a process featuring temporal as well as spatial dependencies in activation timings. When the activation wavefront is passing a cardiac node, the potential gradient at this point reaches the maximum of its amplitude. This property has been acknowledged for in [45] by proposing the following formula for calculation of AT:

$$AT(i) = \max_t \|DV_{i,t}\| \cdot \frac{\partial V_{i,t}}{\partial t} \tag{4.4}$$

where $V_{i,t}$ is the potential at point x_i for the time sample t, $DV_{i,t}$ is an approximated spatial gradient, $\frac{\partial V_{i,t}}{\partial t}$ denotes an approximated temporal derivative. Herewith, it is assumed that the resting phase potential is more negative than its value for the depolarized state, which is true for TMV. In case the opposite holds, i.e. when activation time is associated with most negative slope of the potential curve, AT would be calculated by minimization of this function instead.

Subsequently, the dominant spatial propagation pattern is extracted from AT estimation τ_0 given by (4.4):

$$\tau = \min_\tau \{\|\tau - \tau_0\|_2^2 + \beta \|L\tau\|_2^2\} \tag{4.5}$$

Thereby, activation times τ_0 are smoothed by a Laplacian approximation L that intrinsically underlies propagation process in the heart [46]. For the present work, an optimal parameter β was determined by the L-curve criterion [47] and the node featuring minimal value of the resulting AT distribution τ was assumed to be the excitation origin.

PART II

PROJECTS

CHAPTER 5

Magnetocardiography for Electrically Silent Ischemia: an In-Silico Study Case

In this chapter, the calculation of magnetocardiograms (MCG) is considered within the bidomain theory. Furthermore, multiscale computational simulations of body surface potential maps (BSPM) and MCG are performed for a human torso model in presence of ischemia with varying transmural extent. Remarkably, one setup that resulted in zero ST segment of the ECG signal, so-called 'silent' ischemia, could also not be uncovered by magnetocardiography.

5.1 Motivation

Acute cardiac ischemia is caused by a myocardial metabolic demand that is not covered by blood supply due to coronary artery occlusion [48]. In case not early diagnosed and treated, cellular repair mechanisms can be irreversibly damaged leading to acute myocardial infarction, i.e. cell death. With this regard, two phases of temporal pathoelectrophysiological changes could be distinguished in the first 30 minutes of an acute ischemia [49]. During the first phase (Phase 1a) that peaks approximately between two and ten minutes [50], hyperkalemia, acidosis and hypoxia take place which results in time-dependent decrease of conduction velocity and action potential amplitude. Based on these temporal effects, stages S1 and S2 are discerned within Phase 1a and reached in minutes five to seven and ten to twelve, respectively [51]. Cellular uncoupling occurs in the subsequent Phase 1b that peaks between 20 to 30 minutes after coronary occlusion [50].

Besides the temporal changes, ischemia-affected tissue experiences spatial variations. Ischemia often initially appears on the subendocardium and can spread transmurally towards the epicardial wall, when no treatment is undertaken in due time.

In 12-lead ECG, diagnosis of acute ischemia is mainly based on the changes during the ST-segment: in a healthy case, fully depolarized myocardial cells do not produce any electrical signal on the body surface. In contrast, presence of ischemia gives rise to injury currents flowing from healthy to affected tissue and resulting in depression or elevation of the ST segment. Strength and direction of these pathological currents are determined by ischemia stage and extent [52].

As electric and magnetic phenomena are tightly coupled, magnetocardiography (MCG) represents another measurement tool to record the magnetic fields produced by the bioelectrical sources [53] and may deliver additional information to those obtained by ECG. E.g. in [54], MCG was shown to be more sensitive to tangential currents in the heart, while ECG was superior in characterizing normally oriented and posterior sources. Furthermore, vortex-like sources producing no electrical field can be detected by MCG [55, 56]. Based on these considerations, computational simulations of electromagnetic fields a human body evidently can substantially contribute to understanding of the underlying processes and, thereby, improved clinical diagnosis of acute ischemia.

5.2 Modeling of Acute Ischemia and BSPM Calculation

In [50], in-silico simulations of acute ischemia caused by occlusion of a coronary artery were performed. Furthermore, influence of heterogeneous ischemic regions with varying transmural extent on resulting BSPM was analyzed for three stages (S1, S2, Phase 1b) during the first 30 minutes. In stage S1, an electrically silent setup could be constructed that is also reproduced in the present work for investigations of MCG potential in uncovering the simulated ischemia.

For characterization of ion kinetics, the ten Tusscher ventricular cell model was used [11]. In order to model the modified cell properties of ischemia-affected tissue, parameters from [50] were adopted. Excitation propagation and calculation of transmembrane voltages were performed on a voxel-based heart grid with 0.4 mm resolution using the parallel monodomain solver acCELLerate [14]. For simulation of a normal ventricular activation sequence, a rule-based endocardial stimulation profile was applied [57].

An occlusion of the distal left anterior descending coronary artery was modeled similarly to [50]: regional heterogeneity of ischemia was described by the so-called zone factor (ZF). Whereas the central ischemic zone (CIZ) was set to one, the healthy tissue corresponding to normal zone (NZ) was assigned the value of zero. The transfer region was defined as border zone (BZ), where the parameters characterizing effects of hyperkalemia, acidosis and hypoxia obtained the intermediate values [50]. Ellipsoids of varying semi-principal axes were used for modeling the ischemic areas with gradually increasing extent from subendocardial in setup 1 to almost transmural in setup 5. Image sections of corresponding transmural extents for setups 1 to 5 are displayed in Fig. 5.1.

For calculation of the arising electromagnetic fields, the bidomain theory with a realistic tetrahedral volume conductor model and rule-based assigned cardiac fiber orientation was

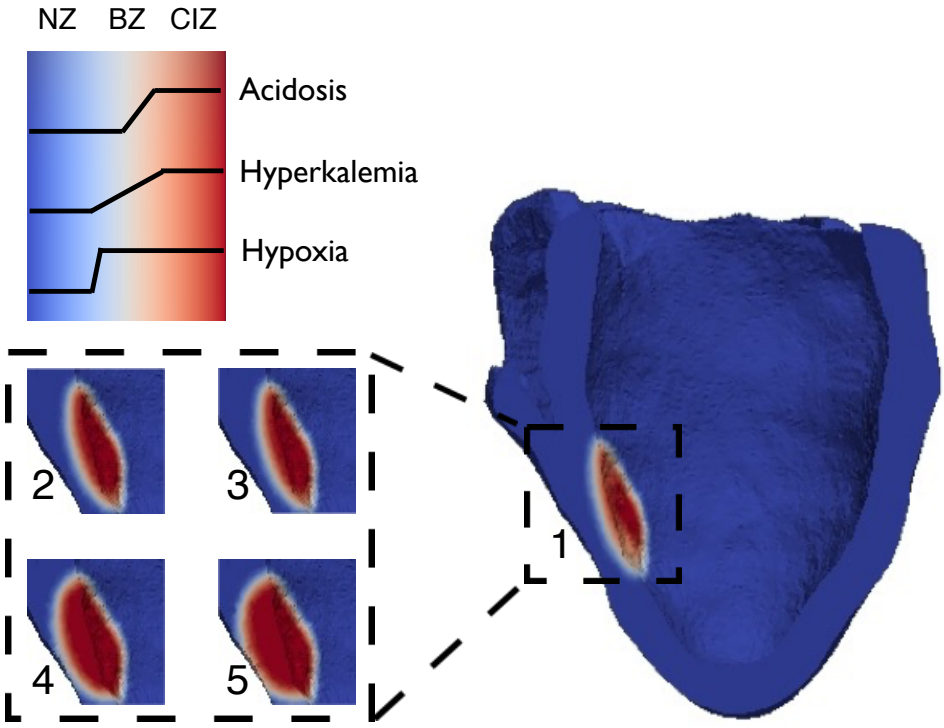

Figure 5.1: Ventricular model with spatially varying zone factors for simulation setups 1-5. For simulation of ischemia, parameters characterizing effects of hyperkalemia, acidosis and hypoxia were modified across the border zone (BZ). The figure is modified from [52].

used. Recall that its governing equation solves a Poisson problem of the following form:

$$\nabla \cdot ((\sigma_e + \sigma_i)\, \nabla \phi) = -\nabla \cdot (\sigma_i \nabla V_m) \tag{5.1}$$

where V_m are monodomain-calculated distributions of transmembrane voltages, σ_e and σ_i the extra- and intracellular conductivities, respectively and ϕ the electrical potentials in the entire torso. Calculations were performed for each millisecond during the QRST complex. The 12-lead ECG was extracted from the respective potential values on the body surface.

5.3 Calculation of Magnetic Fields

The Biot-Savart law states that the magnetic flux density $B(r)$ at a point r is

$$B(r) = \frac{\mu_0}{4\pi} \int_\Omega \frac{J(r') \times (r - r')}{|r - r'|^3} d\Omega \tag{5.2}$$

with the total current density J at each source point r', and the vacuum permeability μ_0.

In the bidomain formulation 5.1, the total current density J reads

$$J = -(\sigma_e + \sigma_i)\nabla\phi - \sigma_i \nabla V_m \tag{5.3}$$

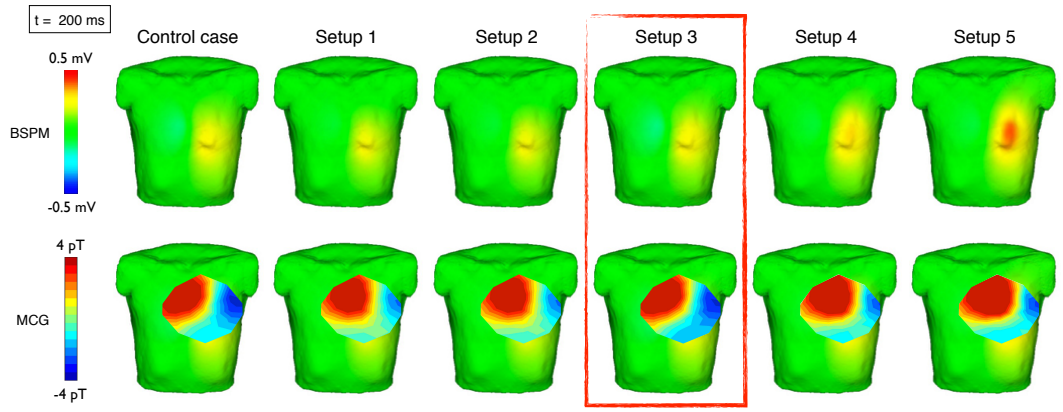

Figure 5.2: BSPM (upper row) and MCG (lower row) of the control case and ischemia simulation setups 1-5. The figure is modified from [52].

While the first term describes passive tissue properties due to Ohm's law, the second term characterizes the impressed current density in the myocardium.

The magnetic flux was computed for 33 magnetometer sensors situated ~4 cm above the anterior chest wall. For visualization, the signals were computed in the direction normal to the magnetometer plane.

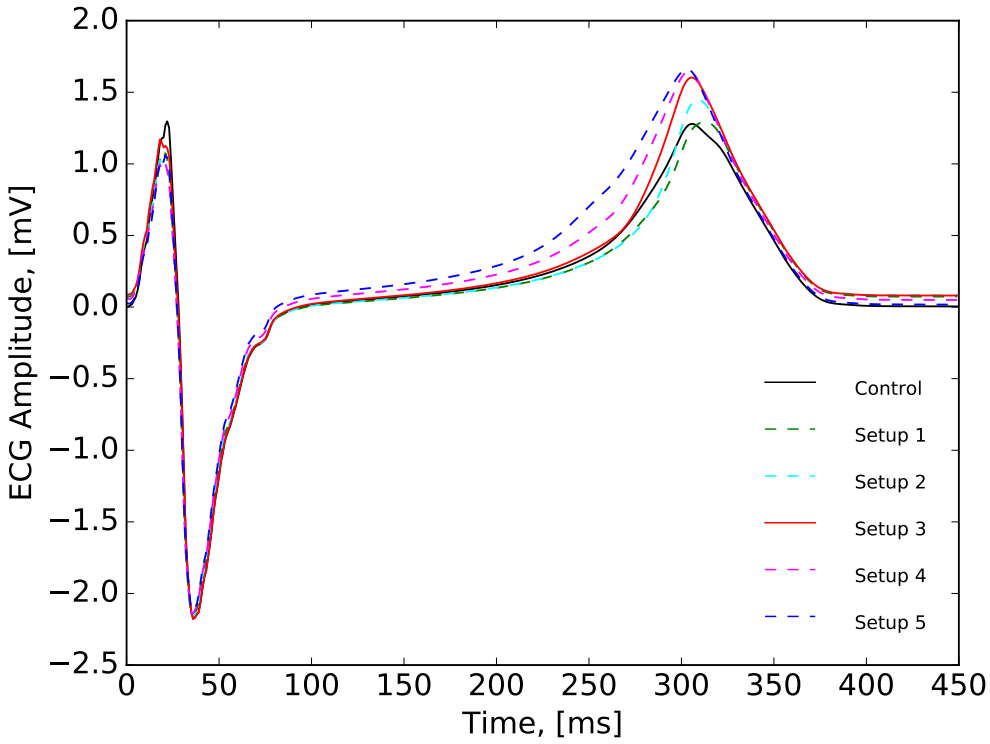

Figure 5.3: ECG at Wilson V_4 lead for the control case and simulation setups 1-5. The figure is modified from [52].

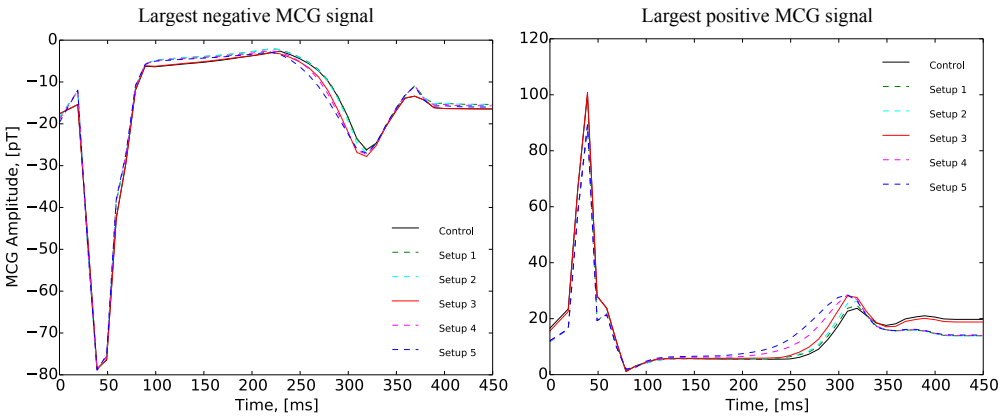

Figure 5.4: Largest negative and positive MCG signals for the control case and simulation setups 1-5. The figure is modified from [52].

5.4 Results

Calculation of electromagnetic fields was performed for a control (healthy) case and five simulation setups of ischemia with varying transmural extent (see Fig. 5.1). In agreement with [50], the precordial lead V_4 exhibited the most prominent changes in 12-lead ECG: resulting electrocardiograms are visualized in Fig. 5.3.

Major ECG changes between the control and acute ischemia cases arose in the ST segment, whereas the QRS complexes featured very similar morphology. For a small transmural extent in ischemia setups 1 and 2, a slight ST-segment depression was observed [52]. While setup 3 resulted in an ECG almost indistinguishable from the control case, setups 4 and 5 corresponding to greater transmural ischemia extents showed a clear ST elevation. For setups 4 and 5, the T wave began immediately after the QRS complex and exhibited a larger amplitude compared to the control case.

In Fig. 5.2, BSPM (upper row) and MCG (lower row) signals for the time instance $t = 200\,\text{ms}$ corresponding to the ST segment are visualized for the control and five ischemia setups. In the control case and setup 3 providing almost identical BSPM, a slight potential elevation near lead V_4 was observed. In contrast, the setups 4 and 5 resulted in more prominent elevation in this region.

With regard to the MCG signals on the sensor plane, control case and setup 3 exhibited very similar patterns, whereas other ischemia setups featured distinct shifts of positive and negative pole locations. For QRST segment, the correlation coefficient between the healthy and ischemic setup cases 1 to 5 constituted 92.79 %, 92.52 %, 99.57 %, 89.02 % and 86.9 %, respectively. In Fig. 5.4, maxima and minima of the MCG signals are plotted for the considered simulation setups. The most prominent changes between the control and ischemic cases were observed for time intervals corresponding to ST segment and T wave. Setups 4 and 5 resulted in the largest amplitude differences.

5.5 Discussion

Over the last decades, distinct information gained by the magnetic field and ECG measurements has been debated. Focusing on electrically silent ischemia, BSPM were shown to improve the detection rate and reveal some changes in the ST segment compared to the standard 12-lead ECG. However, despite this progress, some ischemia cases result in non-ST-change electrocardiograms and consequently are indistinguishable from a healthy scenario [7].

Therefore, identification of electrically silent phenomena is considered to be a potential application of MCG. In [56], Lant *et al.* demonstrated the complementary nature of MCG and ECG measurement modalities for patients suffering from ischemia. In some clinical reports, MCG was also shown to reveal morphological changes in the QRS complex, ST segment shifts and T wave alterations similar to those in ECG [58]. Furthermore, MCG was able to detect the heart pathology for non-ST-changes cases in several studies involving acute ischemia patients and patients with myocardial infarction [59, 60].

In contrast to these results, the simulated ischemia with no ST shift could also not be detected by means of MCG in the present work. Simplified elliptical form of the modeled ischemia was most probably the cause of the compensation effects leading to the zero ST segment. Therefore, further ischemia simulation studies with diverse geometrical locations, forms and sizes must be performed to evaluate the MCG performance in pathology detection [61]. In order to support assumptions about possible electrically silent ischemia configurations, clinical studies with simultaneous recordings of ECG and MCG signals have to be conducted. Furthermore, one should investigate whether combination of both modalities and application of new mixed spatio-temporal ECG-MCG markers could improve the detection rates of silent myocardial ischemia.

CHAPTER 6

Taylor Series Approximation of Potentials as a Function of Conductivities

Computer models of the heart and numerical methods for solving the forward and inverse problem of electrocardiography have been gaining attention over the past decades. Due to continuously increasing computational power, they recently have become feasible for clinical applications.

The forward electrocardiographic modeling, also known as forward problem of ECG, links the cardiac electric activity to the corresponding potentials generated within the human body. As electrical sources are exclusively situated inside the myocardium, the torso can be considered as a passive volume conductor. Internal organs with specific size, form, position and electrical conductivity strongly influence the currents passing through the body volume thus having a great impact on resultant body surface potential maps (BSPM) [62]. In addition to a great variety in anatomic structure, each human also features individual conductivities [63]. Notably, there is still no consensus in experimental values for the conductivity of major tissues varying by a maximum factor of 16 in different reports [64].

These ambiguities gave rise to the simulation studies investigating the effects of heart and skeletal muscle anisotropies and torso inhomogeneity profile on the BSPM [65], ranking organs according to their impact on ECG signals and providing tools for computation of BSPM when conductivity values are uncertain [57, 66]. Furthermore, Weber *et al.* proposed a method based on principal component analysis (PCA) to estimate ECG changes for combined conductivity variations in multiple tissues [67]. The PCA approach was also used for determining the most probable conductivity values for a given BSPM. This technique is briefly outlined in the following section. For details, the reader is referred to the original work [67].

Furthermore, an alternative approach for predicting the BSPM changes is introduced. The proposed scheme is based on a Taylor-series approximation of potentials as a function of conductivities. In comparison to the PCA method, this technique is computationally

more efficient and also capable of predicting the effects of combined conductivity variations. Its particular advantage consists in enhanced visualization of the main direction of BSPM changes with respect to varying conductivity values. The performance of both methods is evaluated and compared for a realistic forward simulation setup.

6.1 PCA-based Method for Prediction of Conductivity Influence on BSPM

PCA is a powerful statistical tool for dimensionality reduction of high-dimensional data. The basic idea is to map possibly correlated variables to linearly uncorrelated ones by means of an orthogonal transformation. In the new coordinate system, the orthogonal basis vectors, which are called principal components, are sorted according to the data variance along the basis directions. The first few principal vectors describe a major part of the high-dimensional data: Therewith, the dimensionality reduction is achieved.

In order to calculate the principal components, the following observation can be employed: Minimization of the error between original data and data projected onto the linear space spanned by the principal components is equivalent to maximization of the variance in the new affine coordinate system. As a result of this, the principal components can be found as eigenvectors of the data covariance matrix.

To reveal the BSPM patterns caused by conductivity variation in each organ k, seven forward calculations with corresponding conductivities σ_k differing by up to 75% from its default value (i.e. -75%, -50%, -25%, 25%, 50%, 75%) are performed. Subsequently, the obtained body surface potentials ϕ are combined to form the data matrix

$$X = \begin{pmatrix} \phi^1_{-75\%}(t_0) & \cdots & \phi^1_{\mathrm{GG}}(t_0) & \cdots & \phi^1_{+75\%}(t_0) \\ \vdots & \vdots & \vdots & \vdots & \vdots \\ \phi^1_{-75\%}(t_{\max}) & \cdots & \phi^1_{\mathrm{GG}}(t_{\max}) & \cdots & \phi^1_{+75\%}(t_{\max}) \\ \vdots & \vdots & \vdots & \vdots & \vdots \\ \phi^{N_{elec}}_{-75\%}(t_{\max}) & \cdots & \phi^{N_{elec}}_{\mathrm{GG}}(t_{\max}) & \cdots & \phi^{N_{elec}}_{+75\%}(t_{\max}) \end{pmatrix}. \tag{6.1}$$

While columns correspond to varying conductivity values and rows to the time steps, N_{elec} is the number of electrodes. In this formulation, the mean-free data matrix X_{mf} and its covariance matrix C are calculated first. Per definition, the principal components $p_1, \cdots, p_7$ are the orthonormal eigenvectors of C corresponding to non-zero eigenvalues $\lambda_1, \cdots, \lambda_7$. In the new coordinate system, any input signal x_i, i.e. a column of the matrix X, can consequently be expressed as a linear combination of the vectors $p_1, \cdots, p_7$ with coefficients $s_{1,i}, \cdots, s_{7,i}$. As demonstrated in [67], λ_1 is much greater than λ_2 for each internal organ k, i.e. the largest data variation is along the first principal component. This allows the following approximation:

$$x_i \approx \bar{x}_i + s_{1,i} p_1 \tag{6.2}$$

where $\bar{x_i}$ is the mean-free signal x_i. The coefficients $s_{j,i}$ ($j = 1, \dots 7$) are called scores and can easily be calculated as:

$$s_{j,i} = (x_i - \bar{x_i})p_i \tag{6.3}$$

In [67], scores obtained for each organ were shown to be monotonically increasing functions of the respective conductivity. Hence, the scores interpolation can be performed in the complete conductivity interval using a monotonic function: In this work, cubic splines were used. For each conductivity within the considered interval, the signals can be approximated as:

$$x(\sigma) = \bar{x_i} + s(\sigma)p_1 \tag{6.4}$$

with a monotonic continuous function $s(\sigma)$.

In order to extend the analysis to conductivity variations in multiple tissues, the influence of different organs on the resulting signal was assumed to be additive:

$$x(\sigma_1, \cdots, \sigma_n) = \bar{x} + \sum_{j=1}^{n} s_j(\sigma_j)p_{1,j} \tag{6.5}$$

Note that PCA performed for different organs result in different mean vectors $\bar{x_i}$. To account for this, the signal $\bar{x}$ is calculated for each default conductivity $\sigma_{1,def} \dots \sigma_{n,def}$. Subsequently, the PCA scores for each conductivity σ_k are shifted as $\hat{s}_k(\sigma) = s_k(\sigma) - s(\sigma_{def})$, respectively. Thus, the signal obtained from variation of a single conductivity k becomes:

$$x(\sigma) = x_{def} + \hat{s}_k(\sigma)p_{1,j} \tag{6.6}$$

The additive effect of conductivity modifications can be described as follows:

$$x(\sigma_1, \cdots, \sigma_n) = x_{def} + \sum_{j=1}^{k} \hat{s}_j(\sigma_j)p_{1,j} \tag{6.7}$$

Furthermore, this relationship allows estimation of optimal conductivities from a given BSPM: Due to nondecreasing behavior of the interpolation scores, the map between scores and conductivities is bijective. This fact enables reconstruction of the conductivities from an input signal by optimizing the scores $\hat{s}_j(\sigma_j)$. In the present work, the root mean squared error (RMSE) between reference and optimized BSPMs was minimized using the Nelder-Mead simplex method [68]. All calculations were done with Matlab, The MathWorks Inc., Natick, MA.

6.2 Taylor Series Approximation of Potentials as a Function of Conductivities

In this section, a new technique for estimation of electric potential changes for varying tissue conductivities is investigated. Provided a default ECG and modified conductivity values, BSPM signals are approximated by means of Taylor series expansion around the default conductivity values.

Recall the main bidomain equation:

$$\nabla \cdot (\sigma \nabla \phi) = -\nabla \cdot (\sigma_{intra} \nabla V_m) \tag{6.8}$$

where the gradient of transmembrane voltages V_m represents the source term, σ describes the tissue conductivities in the volume conductor and σ_{intra} is the intracellular conductivity defined for cardiac tissue. For the heart domain, σ_{intra} constitutes a part of the σ term on the left-hand side. Given the sources V_m, the solution ϕ of (6.8) depends only on the conductivity profile σ.

Although Chapter 3 provides a detailed description of the basis principles of the FE method, the key points for solving 6.8 are recapitulated. Having created a volumetric mesh, the solution ϕ is expressed as a linear combination of some basis functions α_i, $i = 1,\ldots,N$. Discretization of integrals yields the following system of algebraic equations:

$$K\phi = b \tag{6.9}$$

The elements of the 'stiffness' matrix $K_{i,j}(\sigma_k) = \int_\Omega \sigma(\nabla\alpha_i)\cdot\nabla\alpha_j d\Omega$ linearly depend on the conductivity values σ. Assuming the internal inhomogeneity σ to be represented by n compartments with conductivity values $\sigma = (\sigma_1,\ldots,\sigma_n)$, the following equality holds:

$$\begin{aligned} K(\sigma_1,\ldots,\sigma_i+\Delta\sigma_i,\ldots,\sigma_n) = K(\sigma_1,\ldots,\sigma_i,\ldots,\sigma_n) \\ + \Delta\sigma_i K'_{\sigma_i}(\sigma_1,\ldots,\sigma_i,\ldots,\sigma_n) \end{aligned} \tag{6.10}$$

Recollect that conductivity values σ_i are assigned element-wise in the performed FEM analysis. Then, for each tetrahedron belonging to the tissue class k, i.e. having conductivity value σ_i, the gradient of matrix K with respect to a conductivity σ_i ($i = 1,\ldots,n$) can be derived:

$$(K_{i,j})'_{\sigma_k} = \begin{cases} \int_\Omega (\nabla\alpha_i)\cdot\alpha_k d\Omega & \text{if } i = k \\ 0 & \text{if } i \neq k \end{cases} \tag{6.11}$$

Similar to the 'stiffness' matrix K, gradient matrices have to be computed only once.

Using the first-order approximation of potentials as a function of conductivities, one arrives at

$$\begin{aligned} \phi(\sigma_1,\ldots,\sigma_i+\Delta\sigma_i,\ldots,\sigma_n) \approx \phi(\sigma_1,\ldots,\sigma_i,\ldots,\sigma_n) \\ + \Delta\sigma_i \phi'_{\sigma_i}(\sigma_1,\ldots,\sigma_i,\ldots,\sigma_n) \end{aligned} \tag{6.12}$$

In order to calculate the derivative of potentials ϕ'_{σ_i}, differentiate both sides of (6.9) with respect to σ_i:

$$\begin{aligned} K(\sigma)\phi(\sigma) &= b(\sigma_{intra}) \\ K'_{\sigma_i}(\sigma)\phi(\sigma) + K(\sigma)\phi'_{\sigma_i}(\sigma) &= 0 \\ K(\sigma)\phi'_{\sigma_i}(\sigma) &= -K'_{\sigma_i}(\sigma)\phi(\sigma) \end{aligned} \tag{6.13}$$

This implies that computation of the potentials' gradient involves solution of an additional system of linear equations (6.13) of the same size as the original problem (6.8). Therefore,

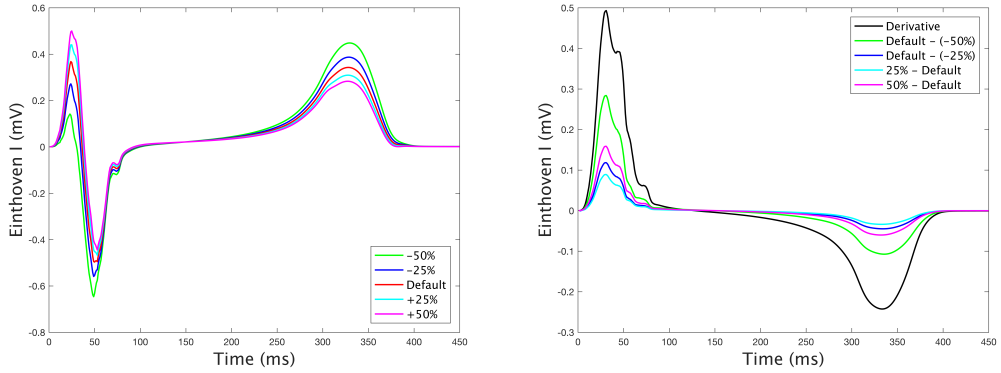

Figure 6.1: (a) ECG for varying blood conductivity; (b) Changes in the ECG caused by varying the blood conductivity: Default corresponds to the ECG for default blood conductivity σ_b; $\pm 25\%$, $\pm 50\%$ to the ECG for modified blood conductivity values of $\sigma_b \pm 0.25\sigma_b$, $\sigma_b \pm 0.5\sigma_b$. Black line represents temporal course for the gradient of lead potential with respect to blood. Its dimension [mV m/S] is adjusted to match the caption.

obtained gradients calculated for all nodes in the considered geometry could also be visualized for improved demonstration of the influence of different tissues on the BSPM for each time instance.

Assuming the influence of conductivities on the resulting BSPM to be additive, which was shown to be valid for the introduced above PCA approach [67], the following equation holds:

$$\phi(\sigma_0 + \Delta\sigma) = \phi(\sigma_0) + \sum_{i=1}^{n} \Delta\sigma_i \phi'_{\sigma_i}(\sigma) \tag{6.14}$$

6.3 Simulation Setup and Validation of First-Order Approximation

To validate the proposed approach for estimation of BSPM changes caused by modified conductivity values, a healthy sinus rhythm was considered. Distributions of TMV were simulated with a monodomain solver. Subsequently, BSPM were computed for a volume conductor model including the inhomogeneous compartments of heart, blood masses, lungs, liver, kidneys and intestine as inhomogeneous compartments (for details on the simulation setup, the reader is referred to the Part 8).

For the BSPM prediction, blood, lungs and torso were considered. First, the forward problem of ECG was solved with the default values of 0.7, 0.04 and 0.2 S/m for these tissues, respectively. Afterwards, their conductivity values were varied by $\pm 25\%$ and $\pm 50\%$ from the default, and BSPM again were computed forwardly. Exemplarily, the signal of the first Einthoven lead is shown for varying blood conductivity in Fig. 6.1a. Despite the signal amplitudes alterations, their morphology is preserved.

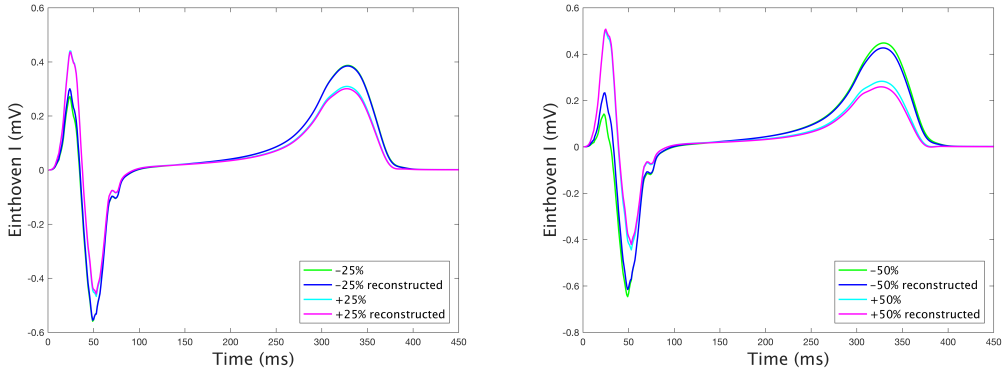

Figure 6.2: Simulated and estimated signals at the first Einthoven lead for 25% (a) and 50% (b) variation in the value of blood conductivity.

To examine the quality of the proposed first-order approximation, conductivity variations in one organ as well as simultaneous variations in all three tissue types were analyzed. The first conceptual test consisted in revealing the ability of the numerically computed first derivative to describe the direction of main changes in BSPM. For this purpose, the temporal changes in ECG as well as the gradient of potentials were computed for varying blood conductivity. In Fig. 6.1b, an exemplary behavior of the curves corresponding to the Einthoven lead I is depicted for blood. The correlation between the forwardly simulated ECG changes and the first derivative was over 99% for all conductivity variations. For lungs and torso, similar results were obtained, which indicates the capability of the first-order approximation to grasp the dependency of electric potentials on the conductivity over time.

Furthermore, performance of the proposed method for estimating the ECG amplitudes was evaluated. According to (6.12), BSPM were predicted for modified conductivities based on the default simulated potentials, the calculated gradient as well as conductivity changes $\Delta\sigma$.

6.4 Results

Estimation of the BSPM was performed for blood, lungs and torso. Whereas predicted signals were very close to the simulated curves for 25% variation from the default conductivity, 50% variation led to larger errors in prediction of the peaks during QRS complex and T wave amplitudes. As an example, Fig. 6.2 provides the simulated and estimated ECG signals in case of varying blood conductivity for the Einthoven lead I.

In order to test the assumption about additivity of changes caused by variations in single organs (6.14), conductivity values of all three tissue types were modified by the same amount of either 25 or 50%. In Fig. 6.3, the corresponding ECG estimation results are shown for the Einthoven lead I.

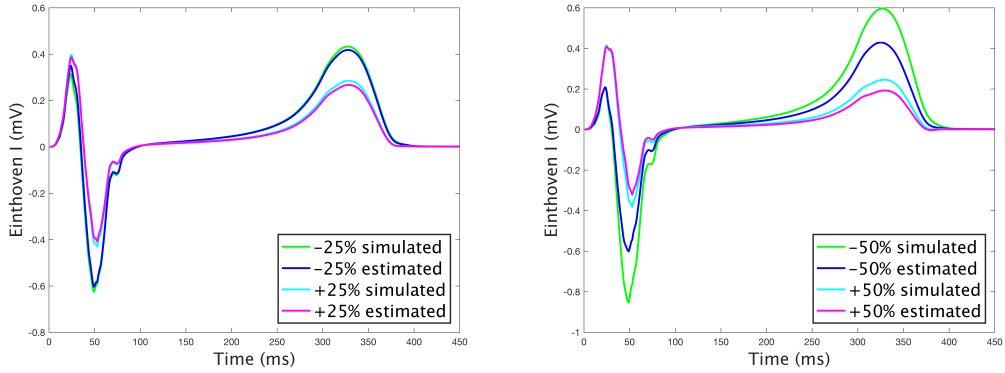

Figure 6.3: Simulated and estimated signals at the first Einthoven lead for 25% (a) and 50% (b) variation in the conductivity values of all organs (all are either -25%, $+25\%$, -50% or $+50\%$).

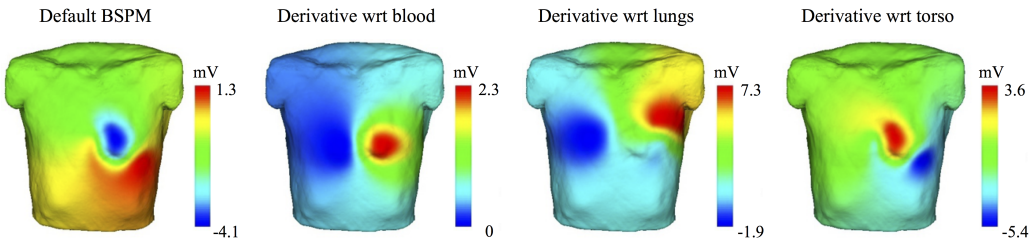

Figure 6.4: From left to right: The body surface maps for potentials and their derivatives with respect to blood, lungs and torso visualized for the time step $t = 30$ ms corresponding to the R peak.

BSPM approximation errors were calculated for both Taylor-series based and PCA approaches. For analysis, the signals at 64 electrodes distributed over the anterior and posterior chest walls for the whole QRS complex (450 ms) were used. Results are summarized in Table 6.1.

The gradients of potentials with respect to the three considered tissues are visualized in Fig. 6.4. Maxima and minima of the gradient maps are situated at different positions implying that the corresponding organs bear linearly independent information content. Their locations for the torso are proximal to those of default BSPM potentials. This relation was consistent for all time steps suggesting high impact of the volume conductor and its conductivity on the resulting ECG.

6.5 Discussion

In this chapter, a novel method for estimating the BSPM in case of modified conductivity values was presented. It is based on the first-order approximation of potentials as a function of involved conductivities and, thereby, requires only one additional solution of the governing

Table 6.1: RMSE [μV] between simulated and estimated BSPM (64 electrodes, 450 ms): first order approximation / PCA-based method.

	Blood	Lungs	Torso	Simultaneous Changes
-50%	46.4 / 35.9	14.8 / 11.1	31.4 / 27.7	97.8 / 19.2
-25%	17.2 / 35.8	6.3 / 11.0	13.7 / 26.3	32.0 / 45.9
25%	16.7 / 35.8	6.2 / 11.0	14.4 / 26.6	30.0 / 50.8
50%	36.7 / 35.9	13.2 / 11.1	30.7 / 27.7	65.8 / 46.4

Poisson equation for the complete volume conductor domain. In contrast, the current-state-of-the-art PCA-based method [67] needs 4 to 6 extra calculations.

For single conductivity variations and conductivity changes of 50%, the prediction ability of the proposed method was slightly worse compared to the PCA technique. At the same time, the resulting errors were only half of those from the PCA method for 25% changes. Considering simultaneous conductivity changes, the PCA-based prediction was significantly better for a variation of -50% but slightly worse for $\pm 25\%$ changes.

The difference in the algorithm performance might result from the considered strategies. Whilst the PCA method is data-driven and extracts the main features from signals simulated beforehand, the analytic Taylor series expansion approach makes use of the problem formulation and the structure of the gradient matrices K'_σ. Both techniques try to predict the BSPM variations as if they were unidirectional, though in a multidimensional space. The first principal component vector or the first derivative vector are considered for each conductivity. Despite this similarity, the amount of change expressed either by scores in the PCA method or by $\Delta\sigma$ in the analytic approximation are of different nature. Whereas the scores were approximated using cubic splines, $\Delta\sigma$ indicates a linear change rate with respect to conductivity values. The former is an empirical observation, while the latter stems from the Taylor series formulation.

Having in mind these similarities, one could conjecture that higher order terms correlate with the gradient and considering them in the analytic approximation would lead to an improvement in the amplitude estimation. However, this should be thoroughly investigated in further in-silico studies.

In practical applications of matching the simulated signals to measured BSPM, conductivity values could be efficiently found by a non-linear optimization procedure (e.g. Nelder-Mead simplex method) in combination with BEM. As for such an approach in practice the sources should be known beforehand, catheter stimuli at co-registered locations could be used for patient-specific conductivity parametrization.

Therefore, the main advantage and practical relevance of the proposed analytic approximation consists in the conspicuousness of its results. As shown above, the main directions of BSPM changes for each time and each tissue type could be easily visualized on the body surface, and, thereby, contribute to the qualitative uncertainty analysis of the assumptions made on conductivity values.

CHAPTER 7

Influence of Volume Conductor Modeling Errors on the Solution Estimate Calculated with Fastest Route Algorithm

As described in Chapter 4, noninvasive reconstruction of cardiac activation times (AT) poses a nonlinear optimization problem. In the reported clinical studies, this problem was initialized using either the critical point (CP) method or the fastest route algorithm (FRA), both in combination with the surface TMP source model. FRA is a rule-based approach for generating realistic activation sequences that are afterwards converted into the ECG. The best initialization is delivered by the sequence resulting in the highest correlation between measured and simulated electrocardiograms. In this section, the influence of forward modeling errors on the quality of FRA-based initialization is investigated. Three simulation setups are considered to examine the effects of volume conductor model properties, cardiac anisotropy and geometrical errors on the localization of ectopic foci on the ventricular heart surface [69]. For the performed analysis, 2 electrode configurations are utilized: a standard 12-lead ECG and a 99 electrodes BSPM system.

7.1 Motivation

Noninvasive reconstruction of electrical cardiac activity recently has begun moving towards clinical application [31, 44, 70, 71]. Characterization of cardiac arrhythmia and localization of the ablation target stay in focus of ECG imaging (ECGI). However, for efficient solution of the inverse problem, one needs an eligible forward model to mathematically describe cardiac electrical sources and their relation to the body surface potential maps (BSPM). Apart from the source model, a proper volume conductor model (VCM) is needed for realistic simulation of the ECG.

Having a VCM and measured a ECG on hand, sources and respective algorithms for their noninvasive estimation could be classified as either potential (epi- and endocardial potentials, transmembrane potentials, current density) or AT-based. In the latter, AT are first matched to a predefined spatio-temporal waveform of the transmembrane potentials (TMP), which are further used for computation of BSPM. Having established the relation between AT and ECG signals through a fixed TMP shape, noninvasive reconstruction of AT poses a nonlinear least-squares (NLLS) fitting problem [40].

This severely ill-posed problem exhibits multiple local minima making its solution highly sensitive to the initial estimate. Therefore, many efforts have been undertaken in order to find an initialization leading to a physiologically meaningful distribution of AT [30, 43, 72, 73]. With this regard, promising results have been achieved with the fastest route algorithm (FRA) [30, 44]. FRA can be used for simulation of an excitation propagation starting from one or more focal origins in the heart. For more details on FRA, the reader is referred to Chapter 4 and original publications by van Dam *et al.* [30, 43]. Each simulated activation sequence is converted into the ECG which is compared to the measured BSPM based on their similarity. The best initialization is provided by the activation sequence with the highest correlation. Yet, therewith obtained initialization depends on the assumptions about conduction velocities in the myocardium. In [40], sensitivity of the NLLS formulation with respect to propagation parameters was demonstrated. Presented results imply that in the two-chain optimization procedure consisting of initializing the NLLS problem and its following iterative solution, exclusively sensitivity of the nonlinear solver to the initial estimate has been investigated so far.

In this work, robustness of the FRA-based initialization with respect to common and partially unavoidable model uncertainties is examined. This tailored model-to-model aims at analyzing the effects of the three sources of forward modeling errors on the FRA performance [69]:

1. simplified VCM by leaving out some organs,
2. omission of cardiac anisotropy, and
3. presence of geometrical errors in a VCM.

For this purpose, consider three simulation setups with increasing extent of modeling inaccuracies. In each setup, a reference model is introduced and quality of the FRA-based initialization is analyzed for 8 test models with varying anatomical complexity and isotropic assumptions on cardiac conductivity.

Within each setup, activation sequences starting from all nodes in the triangulated ventricular mesh are converted into ECG for both reference and test models. Furthermore, error distances between true origins and the best initialization as computed by correlation-based FRA are calculated. Spatial distribution of localization errors in dependence on both considered VCM and electrode configuration is discussed. Moreover, correlation maps between reference and test BSPM are visualized for improved delineation of possible

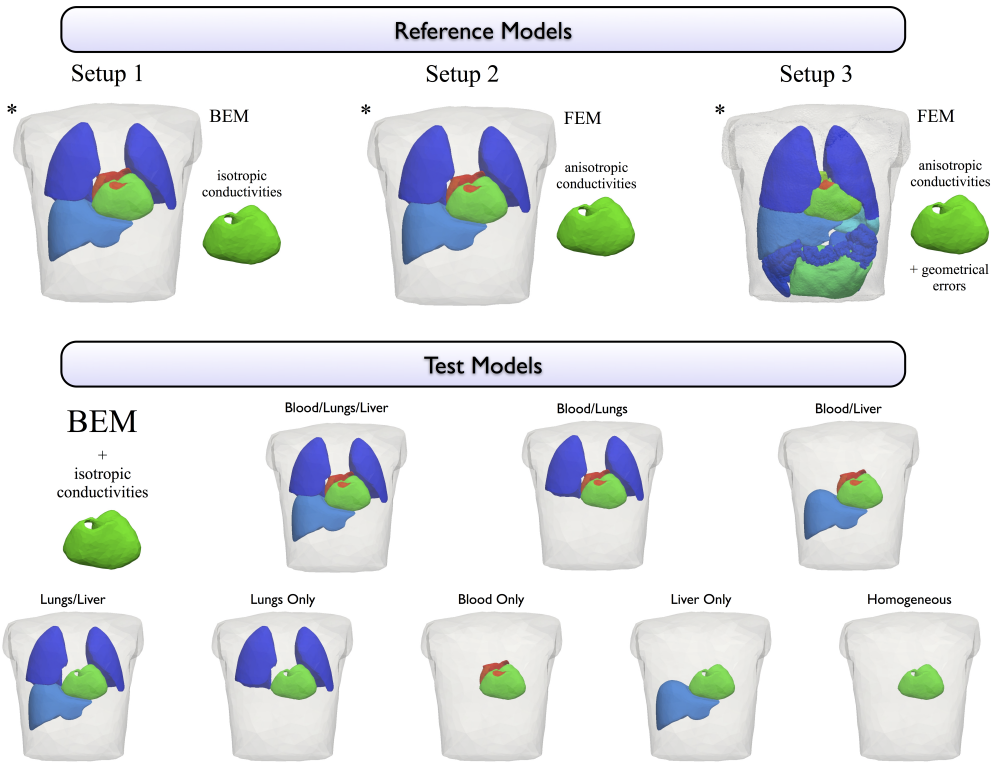

Figure 7.1: Geometrical models and numerical methods of field calculation as used in this study. An asterisk '*' marks identical volume conductor models in the performed analysis. Therewith, reference model 1 equals the corresponding test model and consists of triangulated surfaces of the considered organs. For reference model 2, the same contour lines of the organs were used, but volume discretization was done with 3-D tetrahedral elements in order to account for cardiac anisotropy. The figure is modified from [69].

ambiguities and localization uncertainties in the FRA-based noninvasive imaging of focal activities [69].

7.2 Methods

In this section, simulation setups and involved geometrical models are described. Subsequently, the work-flow for generation of activation sequences and corresponding electrocardiograms as well as the lead configuration systems are presented.

While boundary element method (BEM) was employed in calculating the ECG for setups and models assuming cardiac isotropy, anisotropic nature of myocardial tissue was modeled by means of the finite-element method (FEM). Compatibility of BEM and FEM solvers used was ensured by comparing BSPM resulting from the same source distribution for normal activation under isotropic heart assumption.

7.2.1 Simulation Setups

To systematically address the FRA sensitivity question, three simulation setups were considered. For each setup, a reference model was defined and performance of FRA was evaluated for the introduced eight test models. The test models contained varying amount of anatomical information and were based on the isotropic assumption of heart conductivities. An overview of all setups and models is provided by Fig. 7.1.

In setup 1, the influence of VCM simplifications on the FRA performance was analyzed. Reference ECG were calculated using the most detailed test model under the isotropic heart assumption. For setup 2, cardiac anisotropy was introduced into the reference model 1. Therewith, combined effects of VCM simplifications and omission of myocardial fiber anisotropy were examined. To create the reference model geometry for setup 3, slightly different contour lines from the MRI data of the same subject as used for reference model 1 and 2 were employed. The mismatch in torso and heart geometries between reference model 3 and test models is shown in Fig. 7.2. Besides, this model contained more anatomical information than reference models 1 and 2. Cardiac anisotropy was also integrated into this model resulting in a setup encompassing three sources of errors as compared to test models: inaccurate VCM, neglect of cardiac anisotropy as well as geometrical and lead localization errors.

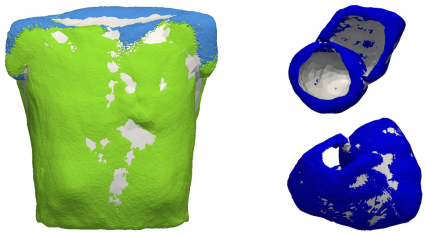

Figure 7.2: Geometrical mismatch in reference model 3 and test models. Surfaces for reference model 3 and test models are visualized in color and grey, respectively. (a) While green represents the subcutaneous fat layer not included into test models, blue depicts torso tissue. (b) The heart surface of reference model 3 is colored in blue.

7.2.2 Volume Conductor Models

For generation of geometrical models, MRI data of a single 27-year old healthy male were employed. While reference model 1 was represented by triangulated organ surfaces, reference model 2 resulted from tetrahedral tessellation of the same geometrical contours. This VCM contained the following tissue types as inhomogeneities in the electrical conductivity profile: lungs, blood masses, liver and torso. Cardiac conductivity was set to that of the torso. The most detailed test model was identical to reference model 1. Other test models were created by considering subsets of organs with their corresponding conductivity values resulting in: blood/lungs/liver, blood/lungs, blood/liver, lungs/liver, blood only, lungs only, liver only and homogeneous models (see Fig. 7.1). In these models, triangulated surface meshes for BEM consisted of 1500, 873, 1.000, 750, 752, 700, 1002, 1002 nodes for heart, left and right ventricular blood masses, left and right lungs, liver and torso surfaces, respectively. In the heart mesh, the average distance between the nodes constituted 6.7 ± 1.5 mm. For setup 2, the reference FEM tetrahedral mesh contained 431499 nodes of which 196849 nodes were in

the ventricular myocardium. Organ conductivities for the described models were assigned as follows: torso with 0.2 S/m, blood masses with 0.7 S/m and lungs as well as liver with 0.04 S/m [30, 57]. For anisotropic heart reference models in setup 2 and 3, values of 0.05 and 0.15 S/m were set for the intra- and extracellular conductivities in transversal fiber direction. Anisotropy ratios were equal to 3 and 9, respectively.

As reference for setup 3, the most complex anatomical model containing the following tissue types was considered: ventricles, atria, ventricular and atrial blood masses, lungs, liver, intestines, kidneys, spleen, subcutaneous fat and torso. Surfaces of heart, lungs, blood, liver and torso were used for creation of reference models 1 and 2 and test models. The mentioned organ contours were extracted from the original tetrahedral mesh and simplified by reducing the number of nodes using the quadric edge-collapse algorithm. In order to increase numerical stability of BEM calculations, the surfaces corresponding to lungs and liver were shifted from the heart contour to avoid any overlapping of their parts. The conductivity values for the heart, lungs, liver, blood masses and torso were set to be the same as in reference models 1 and 2. Conductivites of other internal organs listed above were assigned according to Gabriel *et al.* [74] at a frequency of 10 Hz.

7.2.3 Forward Calculation

Two numerical methods of computing electrical potentials in the human body were considered - FEM and BEM. For more details on both methods, the reader is referred to Chapter 3.

In the realized BEM model, sources were approximated by the equivalent dipole layer (EDL). For each node on the ventricular surface, the TMV is assumed to act as a source with local strength of the double layer. The EDL source model is described in detail in works of van Oosterom, Oostendorp and van Dam (see e.g. [30]).

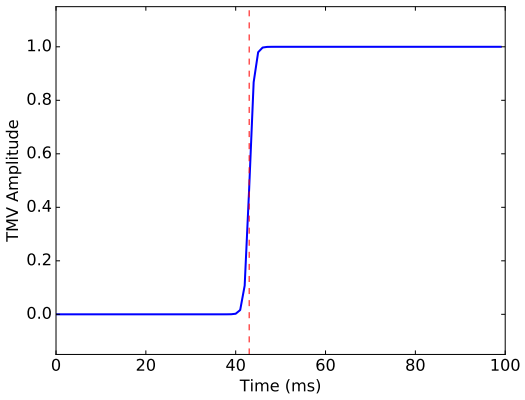

Figure 7.3: An exemplary TMV waveform used in the present work. The dashed red line marks the corresponding activation time.

The time course of local TMV was modeled by specification of AT and a sigmoid function characterizing the TMV upstroke. The TMV wave form used is illustrated in Fig. 7.3. In [30], two TMV shapes with spike and plateau and with constant plateau, respectively, were analyzed for noninvasive source imaging. It was shown that incorporation of early repolarization and plateau phases has only minor effect on reconstruction of AT and quality of the BSPM fit. Based on these considerations, the same TMV template was used for both reference and test models. Whilst the recovery phase was neglected, upstroke and resting stage were considered in the present work [39, 40, 44].

7.2.4 Simulation of Activation Sequences and FRA-Based Correlation Analysis

To analyze the sensitivity of different cardiac areas to the introduced modeling inaccuracies, an activation wavefront was initiated from every node of the geometrical test model resulting in 1500 (number of nodes in BEM heart meshes) FRA calculations. Generated activation sequences correspond to ectopic excitations starting globally around the structurally healthy ventricles. To make the activation patterns more realistic, the anisotropic nature of the myocardium was considered by setting the conduction velocity along the ventricular surface to be twice as high as in the transmural direction, 1 m/s and 0.5 m/s, respectively. With the defined activation sequence and the geometry specific transfer matrices, BSPM could be easily obtained by matrix multiplication:

$$BSPM = A * S \tag{7.1}$$

where the matrix S contains the temporal course of TMV for all cardiac nodes and A is the transfer (or lead-field) matrix between cardiac TMV and potentials at the electrodes positions.

In order to create global error distances and correlation maps reflecting the sensitivity of FRA initialization, the following steps were executed:

- Compute the activation sequence i for each heart node using FRA. Calculate the reference ECG (either 12-lead or 99 leads BSPM) with the appropriate numerical method, i.e. BEM for setup 1 and FEM for setups 2 and 3.
- Contaminate the FRA-generated activation sequences used for the reference model with white Gaussian noise of 5 ms standard deviation. Based on these noisy activation patterns, calculate ECG signals for each test model using BEM.
- Having the electrocardiograms on hand, perform a full-search procedure in order to find the node in a test model providing BSPM mostly resembling the reference signal as given by node i [30]. If the QRS complex duration from node j does not equal the reference value, scale the test activation sequence to match them. Subsequently, calculate test BSPM and the correlation coefficient (CC) between obtained and reference ECG [30, 43, 75]. Note that the scaling keeps the study more realistic as described adjustment of AT accounts for possible uncertainties in the assumed conduction velocities (CV) values, while preserving the morphology of the test signals. For this step, generate correlation maps covering the complete heart geometry to visualize these values on the heart mesh and further use for quantification of possible localization uncertainties.
- In this way, find the best node delivering the highest correlation to the reference BSPM for each test model and lead configuration. Based on these results, the maps of distances between obtained and true activation origins were calculated, which can be used for identification of heart regions most susceptible to the certain error sources under consideration.

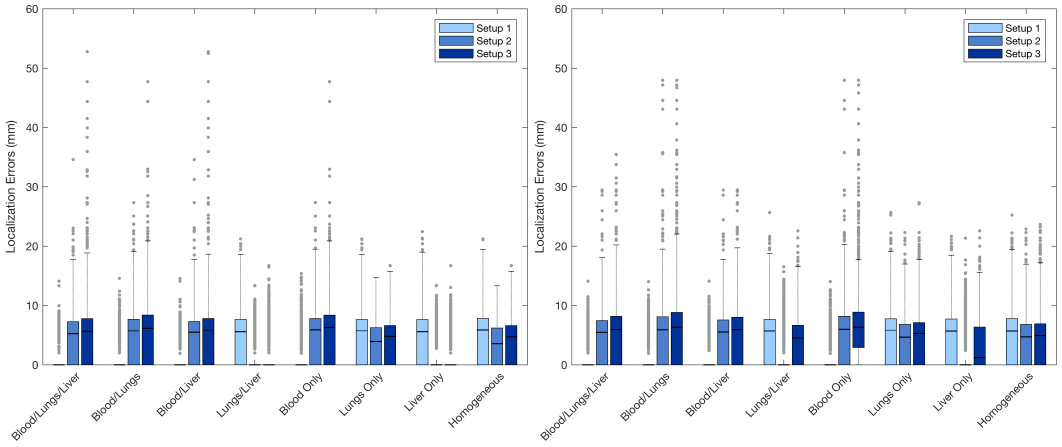

(a) BSPM **(b)** 12-lead

Figure 7.4: Distances between original and localized nodes computed from FRA activation sequences contaminated by white Gaussian noise with 5 ms standard deviation. As the considered interquartile range of 25-75% represents the variation of the middle half in the error distances data, boxes extending to the x-axis imply that the lower 25% of the error distances are zero. Then, lower whiskers also lie on the x-axis. Cases with no box depicted indicate that the localization errors in the upper 75% are equal to zero; the rest of the data is shown as outliers. This figure is reprinted from [69] with permission of the publisher (©2016 IEEE).

7.2.5 Electrodes setups

The delineated robustness analysis was performed for two electrode configurations using either a standard 12-lead ECG or a BSPM system of 99 electrodes distributed in 12 strips over both anterior and posterior parts of the body surface. As mesh nodes in the test models constituted a subset of points in reference models for setups 1 and 2, no electrode positioning errors were introduced. For reference model 3, these electrode locations were projected onto the torso surface resulting in the following electrode mismatches as compared to test models: $1.8\pm$ 0.76 mm with a maximum of 5.36 mm for the BSPM system and 2.13 ± 1.0 mm with a maximum of 4.3 mm for the 12-lead electrodes. Though these errors seem to be rather small, they exceed the reported state-of-the-art lead localization error of an average of 1 mm in clinical applications of the ECGI [76, 77].

7.3 Results

For each simulation setup and test model, error distances between true origins where the reference activation sequences were started and the nodes as found by FRA-based correlation analysis were computed. In Fig. 7.4, the distances for both 12-lead and 99-electrodes system are shown. Surprisingly, less detailed test models, e.g. liver only, lungs only, homogeneous, resulted in a smaller number of outliers. Moreover, their amplitude was smaller compared to more complex models. Table 7.1 provides an overview of the errors across all test models. According to the expectations, increasing level of committed modeling errors led to an increase in the localization errors. Only setup 1, where the influence of VCM properties

was investigated, led to slightly smaller errors for 12-lead ECG compared to those of the 99-electrodes system. For setups 2 and 3, the BSPM lead configuration showed slightly superior performance.

Table 7.1: Distance errors between original and localized nodes (mean $\pm$ standard deviation).

	BSPM, noisy case	12-lead, noisy case
S 1	3.5 ± 4.0 mm	3.6 ± 4.2 mm
S 2	3.9 ± 4.0 mm	4.5 ± 4.5 mm
S 3	4.5 ± 4.7 mm	5.1 ± 5.0 mm

For the 12-lead system, the maximal errors of 48 mm were obtained for blood/lungs and blood only models. In contrast, blood/lungs/liver and blood/liver models resulted in largest errors of approximately 35 and 30 mm, respectively. For the BSPM electrodes configuration, the largest outliers were observed in blood/lungs/liver, blood/lungs, blood/liver and blood only models. The maximal error amounted 53 mm. Other models exhibited comparable behavior resulting in moderate errors lying within 25 mm.

As provided by Fig. 7.4, setup 1 examining the influence of VCM properties on the FRA-based activation sequences resulted in the smallest errors. This simulation scenario is rather unrealistic but still of great importance in proving the robustness of a CC-based approach.

In order to give an insight into the spatial distribution of obtained errors and the differences in performance of considered lead configurations, error distances maps for setup 3 are visualized in Fig. 7.5 and Fig. 7.6. For setup 2, spatial error distributions were very similar to those of setup 3. As a result, setup 3 combining all considered error sources provides the most realistic scenario for analyzing the capability of FRA-based initialization to localize ectopic foci.

Concerning the error distributions in setup 2 and 3, the area with largest errors of over 30 mm was situated on the left ventricular summit (epicardially) region in the geometrical models blood/lungs and blood only for the 12-lead system. Errors between 20 and 30 mm were mostly observed on the right ventricular anterior endocardial wall in the models blood-/lungs/liver, blood/lungs, blood/liver and blood only. For the BSPM electrodes configuration, setups 2 and 3 resulted in the largest errors on the right ventricular endocardial inferior-posterior wall for the models blood/lungs/liver, blood/lungs, blood/liver and blood only. Smaller errors in the range between 20 and 30 mm concentrated on the endocardial anterior wall in the right ventricle, the same region as for the 12-lead case.

7.4 Discussion

Obtained results suggest overall robustness of the FRA-based correlation approach with respect to common modeling errors. Assuming knowledge of the conduction velocities, ventricular ectopic excitations could be localized with a high accuracy of an average 10 mm

for most areas in the heart. However, the left ventricular summit region and endocardial apex of the right ventricles exhibited large outliers of up to 53 mm. It was shown that exclusion of inner inhomogeneities resulted in errors comparable to the inter-nodal distance, which is in accordance with findings in [78]. The homogeneous model provided results very similar to other models thus proving itself to be suitable for the presented correlation-based analysis. Furthermore, calculated error distances revealed a rather minor impact of small geometrical errors on the reconstruction quality.

The analysis of results within setups indicated similar performance of the considered test VCM. Distance errors, however, featured maxima at different locations in the heart. Surprisingly, test models containing blood as inhomogeneity exhibited a larger number of outliers as other models. These phenomena should most probably be related to numerical subtleties of BEM when calculating the double layer integrals for proximal blood and heart surfaces. In the presented models, endocardial heart nodes also belonged to blood meshes and thereby constituted a part of the boundary to high conductive blood masses, whereas other cardiac nodes did not experience a conductivity jump. Nevertheless, it must be pointed out that in the case of the largest outliers, correlation difference as provided by a true and the found origins was smaller than 3 %. This fact emphasizes the sensitivity of this notoriously ill-posed problem on the one hand and robustness of the correlation-based approach as well as importance of CC-maps on the other hand. Fig. 7.7 gives an example for illustrating the described phenomena. For two test models within the simulation setup 3, correlation maps are visualized for the focus resulting in the highest localization error of 48 mm in the 12-lead setup for the blood/lungs model but only in a moderate error for the BSPM electrodes configuration. In contrast, the model blood/lungs/liver has proven to be robust in both electrodes settings. In this study, no noise was added to BSPM signals. Contaminating a signal with white Gaussian noise of up to 20 dB would worsen the CC by only 1 %. Therefore, it was considered to be more 'realistic' to add the noise to the reference AT instead.

Based on Fig. 7.7 demonstrating presence of regions bearing very similar high CC values, it is considered to be advisable to always analyze the complete correlation maps covering the whole heart. This approach would have an advantage over classical regularization schemes yielding only one deterministic solution. Generated CC maps could provide the most probable solution as found by FRA as well as some probability distribution of excitation site origin.

Placing the present work into context of existing studies investigating the effects of VCM properties on the forward ECG problem [57, 62, 65] and analyzing the influence of cardiac anisotropy on the forward [57, 79, 80] and inverse [81–83] modeling, CC was chosen as the similarity measure between signals, which only has been investigated in [57] so far. In order to create a sort of influence maps, the considered correlation-based analysis was applied to BSPM resulting from ectopic excitations starting all over the ventricles, which significantly complements previous studies with few activation sequences examined.

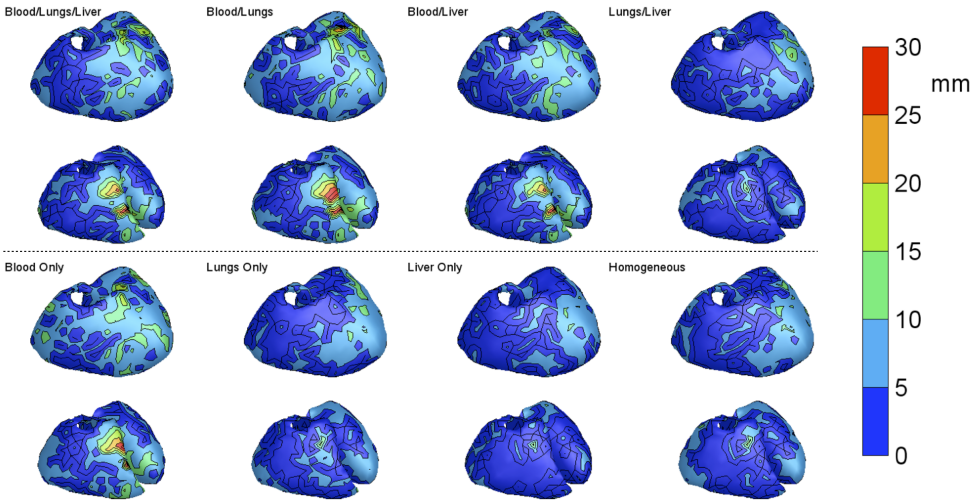

Figure 7.5: Distance maps for the BSPM electrodes configuration in setup 3 with noise contaminated reference activation sequences. For each test model, the distribution of localization errors is shown on the epicardial (upper line) and endocardial (lower line) parts of the heart surface. This figure is reprinted from [69] with permission of the publisher (©2016 IEEE).

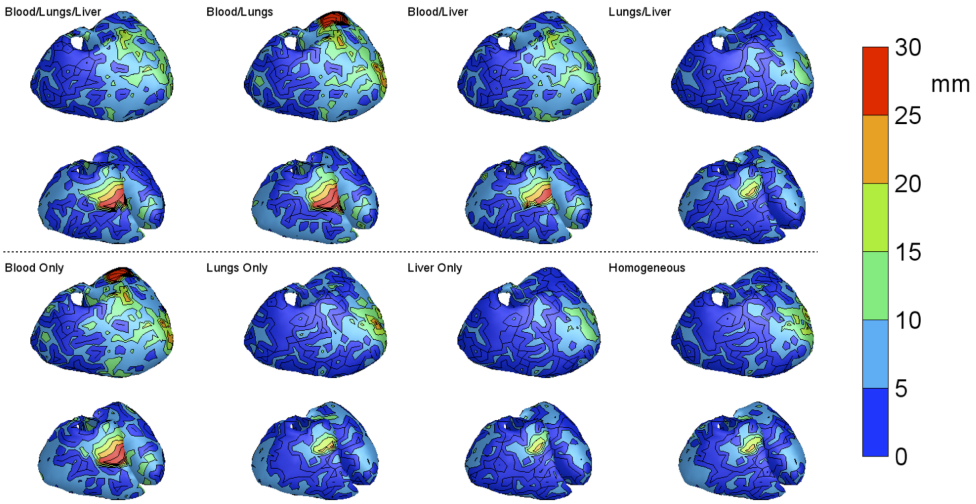

Figure 7.6: Distance maps for the 12-lead electrodes configuration in setup 3 with noise contaminated reference activation sequences. For each test model, the distribution of localization errors is shown on the epicardial (upper line) and endocardial (lower line) parts of the heart surface. This figure is reprinted from [69] with permission of the publisher (©2016 IEEE).

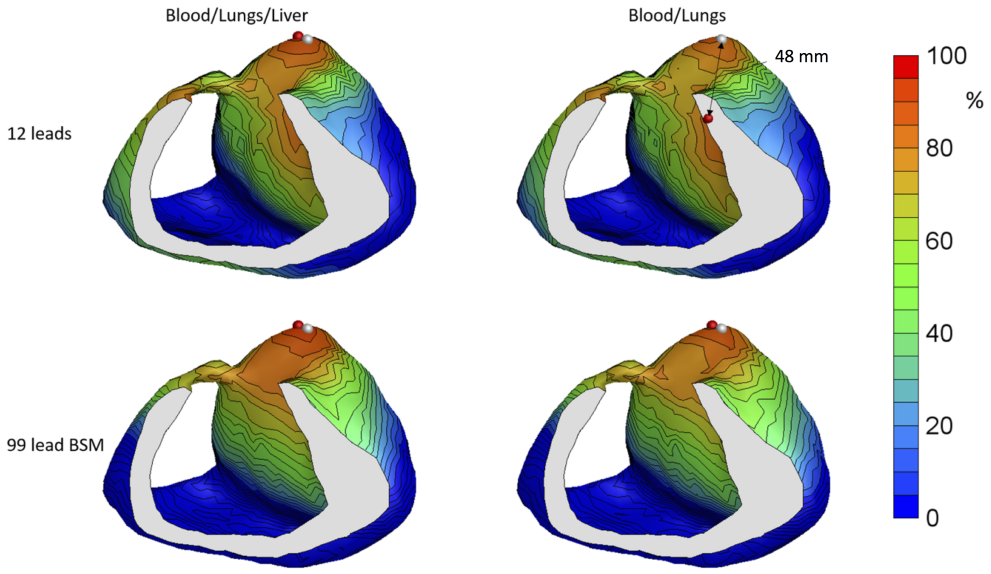

Figure 7.7: Exemplary correlation maps for models blood/lungs/liver and blood/lungs for the point with the largest distance error. Red sphere is the focus with best correlation, grey sphere is the true origin. Upper line: 12-lead electrode configuration, lower line: 99 electrodes BSPM setup. Resuts are shown for simulation setup 3. This figure is reprinted from [69] with permission of the publisher (©2016 IEEE).

Concerning the third goal of the study, the investigation of the role of geometrical errors in cardiac modeling, controlled scenarios such as shifts of the heart and other inner organs as well as random displacement of electrodes were reported [84–88]. In clinical applications of ECGI, however, high-resolution CT scans of the torso in combination with accurate electrode localization techniques are applied [76, 77]. Therefore, the present work focused on simulating state-of-the-art scenarios regarding segmentation and lead localization errors [76, 89–91]. Moreover, the global error distances were computed for all considered setups in order to identify the regions mostly susceptible to specific sources of modeling errors.

To validate the findings of the present study, clinically recorded body surface mapping of paced activation sequences is required. One similar study for patients with structurally normal hearts was performed by SippensGroenewegen *et al.* in [92]. Similarity of the measured ECG resulting from 182 distinct endocardial pacing sites in 12 patients was evaluated using total QRS integral maps. While RV basal anterior and outflow regions exhibited low electrocardiographic sensitivity, QRS configurations generated by LV midseptal sites closely resembled the RV anterior sites, which is in agreement with the present results. One can argue about the similarity criterion used for the sensitivity analysis. For reliable ambiguity detection, more than just one (CC or QRS integral) BSPM features in combination with an electrode localization system might be needed. Furthermore, the recorded BSPM should be possibly classified based on the involved patient-specific volume conductor type, e.g. children, male, female.

As revealed by this study, the localization errors depend on the lead configuration in hand. For the models containing blood, setups 2 and 3 resulted in large errors on posterior

endocardial wall in both electrodes systems. On the other hand, high errors were observed in the LV summit for 12-lead but not for the BSPM, whereas large errors in the RV septal part for the BSPM system were not present in the 12-lead. Comparing both electrode configuration, it turns to be almost evident that electrodes on the back of the torso can deliver additional information and, thereby, eliminate some possible ambiguities in the performed analysis. However, the problem of optimal electrodes setting remains open, as it is most probably dependent on the similarity criterion and furthermore could be associated with a PVC origin location in the heart.

The considered FRA implementation used in the present study [43] assumes its application in combination with the EDL source model. For forward modeling of activation sequences in three dimensional myocardial volume, analogous approaches, such as graph-based or fast marching algorithms [93], can be employed. In the context of noninvasive transmural imaging of TMV or current density sources, the corresponding techniques can be used for estimation of the location and size of an infarction in pathological hearts [34, 94, 95]. This information could be integrated into the patient-specific modeling of local CV differences in the heart.

In a case of multi-focal excitation, e.g. a QRS complex resulting from the Purkinje tree conduction system, the activation sequence can be assumed to be produced from multiple time-shifted focal activities [30]. Therefore, one could conjecture that the resulting localization errors and ambiguity analysis for each early activation site would be in agreement with the present findings for corresponding heart areas.

Finally, one remark should be made about geometrical models involved into inverse calculations. Although all considered test models delivered very similar results due to the robustness of CC as similarity measure, the anatomical model with the most detailed inhomogeneity profile could be required in the following NLLS optimization due to spatio-temporal assumptions imposed on the TMV upstroke and its amplitude.

7.5 Limitations

In [43], FRA in combination with the EDL source model were used to simulate the effects of local ischemia regions on ECG. For the points within an ischemic zone, the conduction velocity value was decreased. However, no changes in the temporal behavior of the affected TMP were explored.

The present investigations were conducted assuming healthy heart tissue. Performance of FRA and possible EDL model parameters adjustment in presence of a non-conducting scar area in the heart are considered in Chapter 12.

Furthermore, the described analysis was conducted under the assumption of known CV. In Chapter 10, the performance of the considered FRA approach is evaluated for reference activation sequences generated on the basis of the modomain theory and a realistic ventricular cell model.

CHAPTER 8

Simulation Protocol: Ventricular Ectopic Beats

This chapter gives an overview of the datasets used for validating the proposed inverse algorithms. Regarding the simulation part of the study, the forward calculations setup specifying excitation propagation computation and geometrical models is introduced.

8.1 Simulation of Ectopic Activation Sequences

8.1.1 Excitation Propagation Model

In order to evaluate the performance of different regularization approaches considered in this study, a simulation dataset consisting of 20 ventricular extrasystoles originating from different heart regions was constructed. All ectopic beats were simulated in a pairwise manner: each extrasystole with the epicardial breakthrough was accompanied by its counterpart with the earliest activation situated on the endocardial wall. Foci in septal regions were placed to different ventricular chambers.

For realistic simulation of ectopic activations, the ten Tusscher ventricular cell model [11] in combination with a 0.4 mm voxel-based heart model of a 27-year old healthy volunteer were used. Excitation propagation and therewith associated transmembrane voltages (TMV) were calculated with the parallel monodomain solver acCELLlerate [14]. Cardiac fiber orientation on the voxel grid was created with a rule-based approach [57]. The simulation setup was adapted from Wilhelms *et al.* [50] resulting in the monodomain parameters described further.

The intracellular conductivity values eventualized in a longitudinal conduction velocity of approximately 0.65 m/s. Furthermore, heterogeneity assumptions on the TMV distributions were incorporated into the model. Ventricular wall was split into three parts: 20% epicardial, 40% midmyocardial and 40% endocardial heart layers [50]. Across the introduced layers, transmurally varying parameters of the potassium channels I_{to} and I_{ks} were assigned as proposed in [11]. In addition, an apico-basal heterogeneity of the potassium conductance g_{ks}

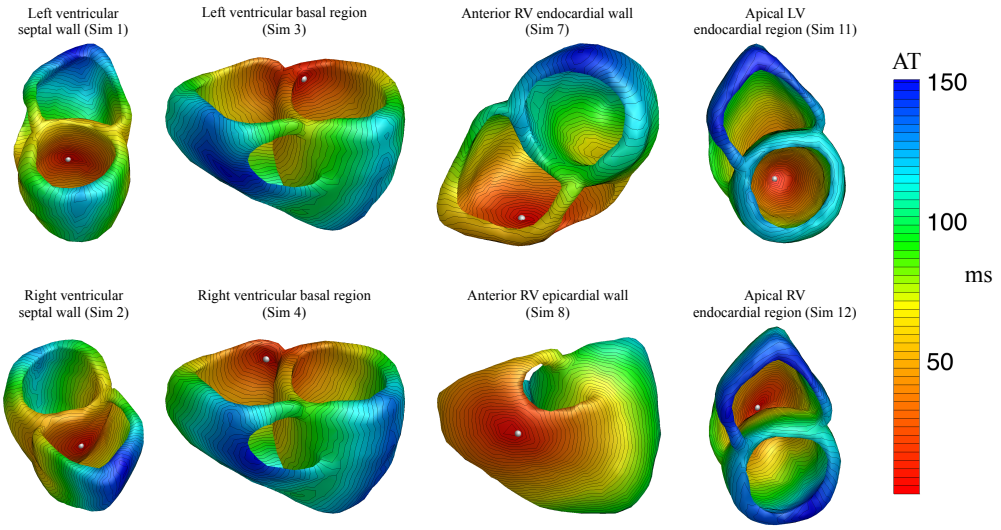

Figure 8.1: Examples of the simulated AT are shown pairwise (column-wise from left to the right) for four cases. White spheres indicate the excitation origin. Column 1: ectopic beats originating from the septal wall. Column 2: ectopic beats originating from basal part of the ventricles. Column 3: ectopic beats originating from anterior RV wall. Column 4: ectopic beats originating from apical part of the ventricles.

was accounted for [50]. For initiating excitation of an ectopic beat, a spherical area with the radius of two voxels was stimulated with an intracellulary injected current.

8.1.2 Volume Conductor Models

The voxel-based TMV computed with the described above monodomain setup were interpolated on a ventricular tetrahedral mesh and, therewith, built the source term for generating electric potentials in the body volume for each millisecond during the depolarization phase. The volume conductor model considered for the forward calculations was created based on the MRI data of the same volunteer and included lungs, heart with the intracavitary blood masses and thorax as inhomogeneous regions in the electrical conductivity profile. The created finite-element tetrahedral mesh consisted of 791983 points of which 48671 were the heart nodes.

The inverse computations were performed with the boundary element method in combination with surface TMP model. For all considered tissue types, geometrical contours were extracted from the FEM model and subsequently simplified by removing the vertices and rebuilding the surface faces. Thereby, the surviving nodes locations were preserved, and the BEM model points represented a subset of the nodes within the FEM grid. This mesh manipulations resulted in a BEM model consisting of 5877 points, including 1500 heart nodes.

The electrical conductivities were assigned to the tissue types as follows: 0.04 S/m for lungs, 0.6 S/m for the blood masses, 0.2 S/m for thorax [74]. In the anisotropic FEM heart model, extra- and intracellular conductivities in the transversal fiber direction were set to 0.15 and 0.05 S/m respectively [57, 96]. The conductivities in the longitudinal (i.e. along the heart

fiber) direction were set to be 3 and 9 times higher than the transversal values in the extra- and intracellular spaces respectively, which is in agreement with [97]. The bulk conductivity value for the myocardium in the BEM model was set up to the sum of transversal extra- and intracellular conductivities from the FEM model which resulted in 0.2 S/m.

8.1.3 Forward Calculations

BSPM calculation was accomplished based on the bidomain theory with the anisotropic heart assumptions. For each simulated ectopic activation sequence, electric potentials were extracted at 120 electrode nodes uniformly distributed over the anterior and posterior torso surfaces. As mentioned above, the electrode positions coincided for the considered FEM and BEM meshes. The BSPM used in the inverse calculations were contaminated with white Gaussian noise of 30 dB.

The activation times (AT) were calculated as the time steps with the largest positive derivative of the TMV, thus corresponding to the upstroke phase. Several examples of AT distributions are visualized for the BEM heart model in Fig. 8.1.

CHAPTER 9

Proposed Methods for Solving the Inverse Problem

Within the scope of the present work, several novel techniques for solving the inverse problem of ECG were designed, implemented and tested. They include a local regularization method for improved imaging accuracy of endocardial activities, an optimization framework combining the regularization properties of EP imaging with a-priori assumptions imposed on the TMV and a binary regularization for the TMV-based problem. An iterative Kozlov-Mazya-Fomin (KMF) method for imaging of the EP and sparse reconstruction of the TMV, although not being new regularization strategies *per se*, do not belong to established methods for ECG imaging application. Nuances in their implementation and performance is extensively evaluated within the considered testing framework.

9.1 Local Regularization

Tikhonov regularization is a standard tool for narrowing the solution space of an ill-posed problem by imposing certain constraints on a desired solution [98]. In the discretized form, the Tikhonov functional can be written as follows:

$$x = \operatorname{argmin}\{\|Ax - y\|_2^2 + \lambda \|Lx\|_2^2\} \tag{9.1}$$

where A is the transfer matrix, L a discrete approximation of the regularization operator, λ is the regularization parameter responsible for the trade-off between the data misfit and a-priori information [99]. In the present work, the Laplacian was used as regularization operator, when the opposite not stated explicitly.

The global minimum of this convex quadratic optimization problem is achieved at the point:

$$x = (A^T A + \lambda^2 L^T L)^{-1} A^T y \tag{9.2}$$

An efficient inversion of the matrix in (9.2) is dependent on dimensions and structure of the matrices A, L and could be performed in different manners. SVD (GSVD), Lanczos bidiagonalization, Arnoldi iterative algorithms were tested for the ECG imaging in [87].

All components of a solution obtained from (9.2) are smoothed by the same amount of regularization λ. However, due to complex cardiac geometry and heterogeneous excitation propagation, this might lead to over-smoothing of some areas in the heart while under-regularizing the others.

9.1.1 Generalised Approach to Local Regularization

Generally, each solution component could be regularized in a different way by introducing a vector regularization parameter $\lambda = \{\lambda_1, \lambda_2, ..., \lambda_n\}$ ($x \in \mathbb{R}^n$). Then the optimization functional (9.1) could be rewritten as:

$$F(x,\lambda) = ||Ax - y||_2^2 + \sum_{i=1}^{n} \lambda_i^2 (L_i x_i)^2 \tag{9.3}$$

with L_i standing for regularization matrix columns. In order to define constraints for the regularization vector, a second functional is introduced:

$$\Gamma(\lambda) = \gamma_1 \sum_{i=1}^{n} (\lambda_i - \lambda_0)^2 + \gamma_2 ||L\lambda||_2^2 \tag{9.4}$$

where λ_0 is an optimal scalar regularization parameter that serves as an initial estimate for all regularization vector components. This global estimate could be obtained from any standard method, e.g. L-curve, GSV, CRESO [100]. By tuning parameters γ_1, γ_2, one could force components of the vector λ either to be close to the value λ_0 or to be smoothly distributed over the heart surface. Under the assumption on λ_i being greater than 0 and smaller than λ_0, tendency of λ_i towards λ_0 would imply decrease of functional Γ and increase in the value of F. Using this observation, a new functional $F + \Gamma$ is constructed:

$$\begin{aligned} \Phi(x,\lambda) = F(x,\lambda) + \Gamma(\lambda) = ||Ax - y||_2^2 + \\ \sum_{i=1}^{n} \lambda_i^2 (L_i x)^2 + \gamma_1 \sum_{i=1}^{n} (\lambda_i - \lambda_0)^2 + \gamma_2 ||L\lambda||_2^2 \end{aligned} \tag{9.5}$$

As the functional in (9.5) is quadratic with respect to x and λ, a saddle point should satisfy the following conditions [101]:

$$\begin{aligned} \frac{\partial \Phi(x,\lambda)}{\partial x_i} = 0, \quad i = 1, ..., n \\ \frac{\partial \Phi(x,\lambda)}{\partial \lambda_i} = 0, \quad i = 1, ..., n \end{aligned} \tag{9.6}$$

These systems can be rewritten in the following way:

$$\begin{aligned} (A'A + (L * \lambda)'(L * \lambda))x = A'y \\ R(x)\lambda = \gamma \end{aligned} \tag{9.7}$$

which can be solved iteratively. The form of operator R and vector γ follow from the iterative formulae:

$$\begin{aligned} x^{k+1} = (A'A + (L * \lambda^k)'(L * \lambda^k))^{-1} A'y \\ \lambda^{k+1} = (diag(Lx^{k+1}) + \gamma_2 L'L + \gamma_1 I))^{-1} \gamma_1 \lambda_0 \end{aligned} \tag{9.8}$$

where I is an identity matrix of corresponding dimension, and $L * \lambda^k$ is understood as column-wise multiplication of matrix L with vector λ^k. In agreement with these assumptions, the update formula for λ becomes:

$$\lambda_i^{k+1} = \begin{cases} 0, & \lambda_i^{k+1} \leq 0; \\ \lambda_0, & \lambda_i^{k+1} > \lambda_0; \\ \lambda_i^{k+1}, & \text{otherwise.} \end{cases} \tag{9.9}$$

The iteration process stops when relative error between successive solutions $\{x^k, x^{k+1}\}$ and $\{\lambda^k, \lambda^{k+1}\}$ gets smaller than a small predefined tolerance ε.

Theoretically, the derived scheme allows simultaneous optimization of both solution and regularization vector. However, it involves two generally unknown parameters γ_1, γ_2 related to the characteristics of noise and depends on the initial solution estimate resulting from λ_0. Although conducted tests revealed superior performance of the presented algorithm over classical approach for some cases, automatic assignment of involved parameters γ_1, γ_2 remains an open challenge. Therefore, in order to define physiologically meaningful guidelines for choosing regularization parameter and simplify the problem at hand, local regularization is thereupon considered for endo- and epicardial parts of the heart surfaces.

9.1.2 Local Regularization of Endo- and Epicardial Surfaces of the Heart

In case the sources are known to be situated in certain part of the heart (e.g. endo- or epicardial surface), one can reduce the optimization problem (9.1) by eliminating corresponding columns from matrices A and L. However, care should be taken about possible source gradients arising on the border between eliminated and remained areas: leaving out some columns of the transfer matrix is equivalent to setting the potentials for corresponding heart nodes to zero. Inversely calculated potentials would compensate for that in order to match the resulting heart vector to the true one. However, due to anatomical structure of the heart, these effects could be negligible in some cases and overall reconstructed pattern would preserve the main solution characteristics.

An alternative method of treating distinct heart areas without need of taking care for compensating effects is to apply local regularization to the regions of interest.

As ECG imaging of activities originating on the endocardial heart surface remains a challenging task [46], in the present work only endo- and epicardial parts were considered for local regularization. For comparison, epicardial and endocardial imaging of TMV was performed first by eliminating strategy. Afterwards, a local regularization problem was solved:

$$x = \operatorname{argmin}\{\|Ax - y\|_2^2 + \|\Lambda L x\|_2^2\} \tag{9.10}$$

where Λ is a diagonal matrix with two distinct entries λ_1, λ_2 on its main diagonal corresponding to local weighting factors.

In order to estimate an optimal pair of the regularization parameters, the solution space is first estimated for all possible combinations $(\lambda_1, \lambda_2) = [\lambda_{min} \ldots \lambda_{max}] \otimes [\lambda_{min} \ldots \lambda_{max}]$. In case system noise level is known, the best combination would satisfy the discrepancy principle

[100]. In a more realistic case of noise properties being unknown, an L-surface approach as proposed in [102] could be considered. In the present work, L-curve was used to calculate a scalar parameter λ for epi- and endocardial imaging [103]. For local regularization, the best solution candidate was defined based on the reconstruction results of the three inverse approaches (epi-, endocardial and local regularization) under assumption of depolarized region to be situated either on endo- or epicardial surface. All calculations were performed for an initial time step $t = 20$ ms after QRS onset, which was supposed to satisfy the made assumption.

9.1.3 Results

In order to support the idea behind local regularization, performance of the proposed method for three characteristic examples is visualized in Fig. 9.1. Simulated and reconstructed TMV for PVCs originating from the RV septal wall, endo- and epicardial LV lateral wall are shown. For the septal case (upper row in Fig. 9.1), Tikhonov and epicardial imaging biased the solution towards the RV lateral wall, whereas endocardial and local regularization provided similar results allowing for correct detection of excitation origin. In case of an epicardial breakthrough (middle row in Fig. 9.1), Tikhonov, epicardial and local imaging could correctly identify the region of interest, whilst regularization of the endocardial surface resulted in the most negative potentials over the desired area projected from the epicardial part. For the corresponding endocardially originated PVC (lower row in Fig. 9.1), performance of endocardial and local imaging was consistent. Tikhonov regularization failed to correctly detect the region of interest. Analogous to the previous case, restricting sources to lie on the epicardial surface delivered a smooth solution with a peak around the site projected from the true origin.

To evaluate accuracy of the presented approach, points exhibiting highest reconstructed TMV value were assumed to be activation origins. Overall localization error was 20.2 ± 15 mm with maximal values of 48.3 and 57.7 mm for simulation 3 and 4, respectively. These cases correspond to the PVCs situated on the posterior basal part of the ventricles in immediate proximity to the border between endo- and epicardial heart surfaces. For other excitation sites, solutions behavior was consistent with the cases delineated by Fig. 9.1.

9.1.4 Discussion

Previously, several methods for 'local' regularization of the ECG inverse problem were introduced in [104–106]. In [104], Oster and Rudy proposed a "regional regularization" that decomposes the measured BSPM using either Legandre polynomials or singular value decomposition (SVD) and applies individual regularization to the obtained decomposition components. Thereby, the local regularization is imposed in the BSPM space and depends only on the signal content and not on the underlying solution topology, which is distinct to the concept introduced in the present work.

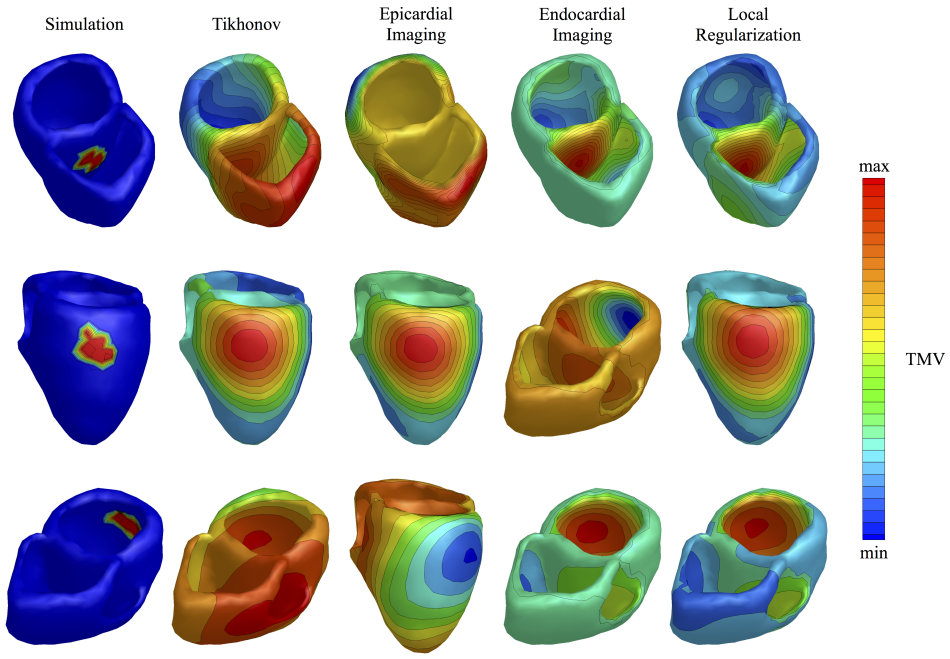

Figure 9.1: An example of simulated and reconstructed TMV. Inverse calculations were performed with (from left to right): Tikhonov, epicardial, endocardial and local imaging.

In contrast to that, a regularization technique addressing spatial local properties of the sought solution was presented by Ahmad *et al.* in [105]. The authors examined a possibility of stabilising inverse solution by introducing multiple regularization terms into the optimization scheme. It was shown that certain constraints targeting local solution properties can be integrated by proper weighting of the regularization matrix L. In one example, a weighting based on the estimate of Laplacian for (known) epicardial potentials was demonstrated to lead to improved inverse results. Although this technique is similar to the proposed methodology in the way it is related to geometry, a meaningful initial solution estimate is required for improved performance. In the present work, local regularization was considered in the specific PVC context and the heart was subdivided into two regions of interest. By costs of lacking flexibility in some cases, e.g. ectopic beats starting on the cross border between endo- and epicardium, this method was demonstrated to result in superior performance with respect to detection of septal ectopic beats.

Another local regularization technique was devised by Johnson and MacLeod in [106]. The authors regarded the inverse operator as constructed from the finite element analysis: A^{-1} was shown to involve inversion of two ill-conditioned matrices describing the "interaction" of the volume conductor with the heart and torso nodes. The regularization of these two sub-matrices in distinct manner with an optimal regularization parameter determined by the L-curve [47] resulted in performance superior over the standard Tikhonov method. Though involving the geometrical details into the solution scheme, this method does not act locally on the solution domain, which is conceptually distinct to the local regularization introduced here.

9.2 An Iterative Method for Solving the EP-Based Inverse Problem

All regularization methods for solving the classical ill-posed Cauchy problem for Laplace equation can be divided into two big groups [107]. The first group transforms the original problem into a well-posed one in Tikhonov sense by introducing a regularization functional and thus converting it to an optimization problem [98, 108]. The second group contains iterative methods that can easily account for any physical constraints [109].

In the following, an iterative method proposed by Kozlov, Mazya and Fomin (KMF) [110] for regularizing the ill-posed Cauchy problem is considered for the ECG imaging application. It has been previously employed for the Laplace and Helmholtz equations showing convergence and providing practical stopping criteria [111, 112]. Conceptually, this method is closely related to a variational Steklov-Poincaré formulation [113] that was examined in the context of ECG inverse problem for a synthetic data set with a concentric spherical geometry [114]. So far, performance of the KMF-method has been investigated for imaging of an *in silico* ventricular fibrillation case [115]. In this study, localization accuracy of the KMF-method is evaluated for ventricular ectopic sequences.

9.2.1 KMF-Method

According to electromagnetic fields theory applied to the inverse problem of ECG, a unique potential solution can be found on a closed surface containing all actual sources. A general formulation of the problem reads as:

$$\begin{aligned} \nabla \cdot (\sigma \nabla \phi) &= 0 \quad \text{in } \Omega \\ \phi &= BSPM \quad \text{on } T \\ \frac{\partial \phi}{\partial \mathbf{n}} &= 0 \quad \text{on } T \\ \phi &= ? \quad \text{on } H \end{aligned} \tag{9.11}$$

where T denotes the thorax surface, H is the heart surface, Ω is the volume conductor with the boundary $\partial\Omega = T \cup H$, σ is the electrical conductivity profile.

The problem of finding ϕ on the heart surface is a classical example of an ill-posed problem with overdetermined data on one boundary. Note that both Dirichlet (BSPM) and Neumann (zero flux) boundary conditions are provided on the thorax surface T. The KMF regularization scheme is based on alternative solution of two mixed well-posed boundary value problems with the solutions converging to the sought potentials of (9.11) [110].

Define an initial potentials estimate ϕ_0 and a sequence (ϕ_n, ψ_n) to be solutions of the following problems:

$$\begin{aligned} \nabla \cdot (\sigma \nabla \psi_n) &= 0 \quad \text{in } \Omega \\ \psi_n &= \phi_n \quad \text{on } H \\ \frac{\partial \psi_n}{\partial \mathbf{n}} &= 0 \quad \text{on } T. \end{aligned} \tag{9.12}$$

$$\begin{aligned} \nabla \cdot (\sigma \nabla \phi_{n+1}) &= 0 \quad \text{in } \Omega \\ \frac{\partial \phi_{n+1}}{\partial \mathbf{n}} &= \frac{\partial \psi_n}{\partial \mathbf{n}} \quad \text{on } H \\ \phi_{n+1} &= BSPM \quad \text{on } T. \end{aligned} \tag{9.13}$$

Subsequently, define operator $D(\phi_k) = \psi_{k+1}$ to solve problem (9.12) and note that operator in (9.13) mapping ψ_k to ϕ_{k+1} is affine and could be decomposed into two more tractable parts:

$$\begin{aligned} \nabla \cdot (\sigma \nabla \phi_{n+1}) &= 0 \quad \text{in } \Omega \\ \frac{\partial \phi_{n+1}}{\partial \mathbf{n}} &= \frac{\partial \psi_n}{\partial \mathbf{n}} \quad \text{on } H \\ \phi_{n+1} &= 0 \quad \text{on } T. \end{aligned} \tag{9.14}$$

and

$$\begin{aligned} \nabla \cdot (\sigma \nabla b) &= 0 \quad \text{in } \Omega \\ \frac{\partial b}{\partial \mathbf{n}} &= 0 \quad \text{on } H \\ b &= BSPM \quad \text{on } T. \end{aligned} \tag{9.15}$$

Observe that problem (9.15) does not involve any iteration steps and its solution b is required to be calculated only once. Furthermore, define operator $N(\psi_k) = \phi_{k+1}$ to solve the system (9.14). Then, an update formula for ϕ_{k+1} becomes:

$$\phi_{k+1} = N(D(\phi_k)) + b \tag{9.16}$$

Linear operators N and D correspond to the well-posed boundary values problems and depend only on geometry of the problem. This observation allows calculation of these operators beforehand and leads to a fixed-point iteration formulation (9.16) of the original system (9.11).

Due to limited imaging ability of EP-based problem, (9.11) was solved for pericardial potentials on a surface encompassing the complete heart. Iterations (9.16) were performed until stopping criteria on relative difference between two consecutive solutions was met, i.e. $\|\phi_{k+1} - \phi_k\| \leq \varepsilon$ with $\varepsilon = 10^{-3}$.

9.2.2 Results

In order to calculate localization errors, true excitation origins were first projected onto the pericardial surface used for inverse calculations. Activation times were computed as points showing the most negative $d\phi/dt$ value and subsequently smoothed by spatio-temporal method introduced in Chapter 3. Exemplary reconstruction results are shown in Fig. 9.2.

Mean localization error was 15.3 ± 14 mm with the largest error of 65.6 mm for the LV septal extrasystole. Whereas the true excitation wave showed up first on the posterior cardiac wall, the inversely reconstructed origin was situated on the anterior wall, i.e. on the opposite septum side. Exclusion of this case resulted in errors of only 12.6 ± 7.7 mm.

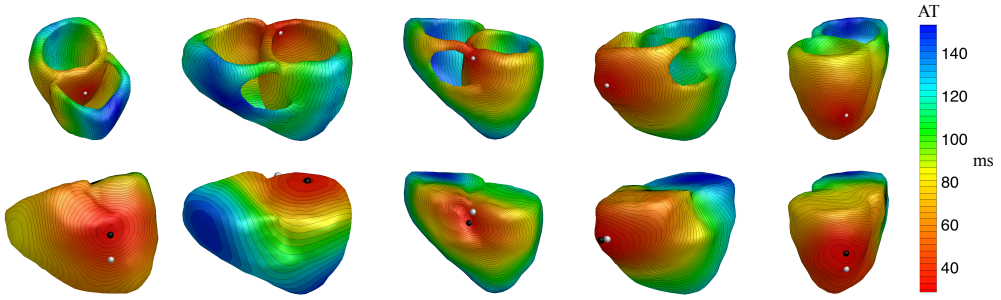

Figure 9.2: Upper row: simulated activation times, lower row: activation times resulting from the KMF reconstructions on pericardial heart surface. White spheres correspond to the simulated earliest breakthrough points. Black spheres mark reconstructed excitation sites.

For one-shot reconstructions of EP at time step $t = 30\,\text{ms}$, localization errors were $22.9 \pm 16.2\,\text{mm}$ with reconstructed origins defined as nodes with most negative EP value.

9.2.3 Discussion

In this study, the performance of the KMF-method was evaluated for imaging of pericardial potentials for PVC origin detection. Although this source model limits application of the technique for reconstruction of endocardial events, promising localization results encourage further investigations on this method for imaging of atrial activities. Nevertheless, the post-processing step for reconstructed AT was observed to be necessary for achieving improved localization accuracy. This dependency as well as more reliable methods for PVC origin detection from single reconstructions should be further explored.

9.3 Optimization Framework for Weighted Regularization of TMV: Incorporation of Different Types of A-Priori Information

Transmembrane voltages represent the cardiac electrical sources and can be reconstructed from BSPM directly using regularization. However, clinical validation of TMV-based inverse solutions would require *in vivo* optical mapping that hinders verification of this source model with current-state-of-the-art technology. Nevertheless, the problem of reconstructing TMV can be split into two parts: a classical Cauchy problem for EP and imaging of TMV from the EP found at the first step [116]. The first sub-problem has been extensively studied and direct computation of the cardiac sources from BSPM constitutes the major part of the present work. Though, the second sub-task was demonstrated to have a well-behaved stable solution under available a-priori assumptions on the targeted TMV [116]. Burger *et al.* analysed the problem of reconstructing ischemia regions during resting phase by minimizing the norm $||x - x_0||$ under linear relationship linking the sought TMV to the heart potentials [116]. For the resting phase of action potential, x_0 was assumed to have a constant value.

Recalling the FEM-based bidomain formulation of forward ECG problem, one can rewrite the governing Poisson equation in the discretized form as follows:

$$Ku = Sx \tag{9.17}$$

where K and S are the stiffness matrices for the involved elliptical operators, u are potentials in the complete FEM-volume, x are the TMV. In [117], Dafang *et al.* proposed an optimization framework that minimizes the term $L(x-x_0)$ under conditions consisting of equality constraints (9.17), convex inequality constraints controlling the misfit between predicted and reconstructed BSPM to lie within the noise level ε and inequality constraints assuming negative values for the TMV.

Note that in [117] two-dimensional problems of reconstructing ischemic areas were considered. Discretization of the Poisson equation for a three-dimensional realistic torso model would result in prohibitive computational costs. Another observation reveals ineffectiveness of applying a discrete Laplace operator to a constant x_0 in the minimization functional, as this cancels the term and plays no further role in the optimization procedure.

In line with these considerations, a new optimization framework bearing advantages of previous investigations and imposing physiological constraints on the sought solution was designed:

$$\{x,\phi\} = \min_{x,\phi} \rho||Lx|| + (1-\rho)||x-x_0|| \tag{9.18}$$

$$\text{subject to} \quad Ax = \phi \tag{9.19}$$

$$||B\phi - y|| \leq \varepsilon||y|| \tag{9.20}$$

$$l \leq x \leq u \tag{9.21}$$

x, ϕ are the TMV and EP respectively, x_0 is the a-priori value for TMV value for all heart nodes, A, B are the transfer matrices mapping TMV to EP and EP to BSPM respectively, L is a discretized version of Laplace operator, y is the BSPM, ε is estimated (or known) noise level, ρ is a constant varying from 0 to 1 and playing a role of trade-off between the desired solution properties: smoothness and proximity to the a-priori defined value. l, u are the vectors specifying lower and upper bounds on the TMV values [118]. As the main topic of the present work is PVC localization, x_0 was chosen to be the resting transmembrane potential with value of -80 mV. l, u were set to -80 and +20 mV, respectively. Note that these values could be easily adjusted to match other pathology, e.g TMV values of ischemia during the ST segment.

In contrast to previous works, minimization functional (9.18) is split into two terms that control the weights of smoothness and a-priori constraints. Furthermore, lead-field matrices A, B could be calculated beforehand and link only the values of interest. In this formulation, the admissible solution space is constrained by (9.18), (9.21). Possible measurement and modeling errors are taken into account by (9.20) with ε playing a role of regularization parameter. Condition (9.19) might be used for coupling of EP and TMV. Otherwise, B in (9.20) could be replaced by a transfer matrix connecting TMV to BSPM.

9.3.1 Simplified Framework for TMV Reconstruction

The designed framework (9.18)-(9.21) might be a comprehensive tool for simultaneous noninvasive estimation of TMV and EP that imposes available physiological constraints on the solution and allows for possible validation of EP. However, during optimization each inequality constraint is first translated into equality problem by introducing additional slack variables that significantly increases computational burden. In order to bypass this problem still keeping the key-advantages of the considered methodology, a modified optimization scheme is proposed:

$$\begin{aligned} x = \min_x \ & \rho||Lx|| + (1-\rho)||x - x_0|| \\ \text{subject to} \quad & ||Ax - y|| \leq \varepsilon||y|| \\ & l \leq x \leq u \end{aligned} \tag{9.22}$$

The reconstruction is performed only for TMV that enable imposition of physiologically meaningful constraints. Conducted numerical experiments confirmed ability of this algorithm to preserve the regularizing properties of its more complex counterpart, while setting reconstruction of EP aside and, thereby, significantly reducing computational time. However, this optimization problem involves quadratic inequality constraints that could be replaced by more efficient linear ones:

$$\begin{aligned} x = \min_x \ & ||Ax - y|| + \lambda * (\rho||Lx|| + (1-\rho)||x - x_0||) \\ & l \leq x \leq u \end{aligned} \tag{9.23}$$

This last optimization problem resembles more a classical Tikhonov approach, though taking advantage of available a-priori information. Numerical experiments proved similar behaviour of formulations (9.22) and (9.23) with slightly superior performance of the latter formulation. In the following, results are referred to this scheme.

9.3.2 Optimal Choice of ρ

To investigate results dependency of (9.23) on parameter ρ, its value was varied from 0 to 1 with a step 0.1 [118]. In Fig. 9.3, exemplary reconstruction for three ρ parameter values are presented. Limit cases $\rho = 0$ and $\rho = 1$ confirmed the necessity of splitting the minimization functional into two terms for better reconstruction quality. Furthermore, results suggested that ρ values between 0.6 and 0.8 provided the best trade-off between solution smoothness and a-priori constraint to adhere to x_0 value. Presented reconstructions were performed for $t = 30$ ms. Advancing in time towards the middle of QRS-complex, an optimal ρ parameter might continuously increase. After reaching the R peak, x_0 should be changed to the value of u.

9.3.3 Results

For the inverse calculations, ρ was set to 0.8 and λ determined based on the L-curve criterion. In order to evaluate performance of the proposed formulation, reconstructed PVC origins

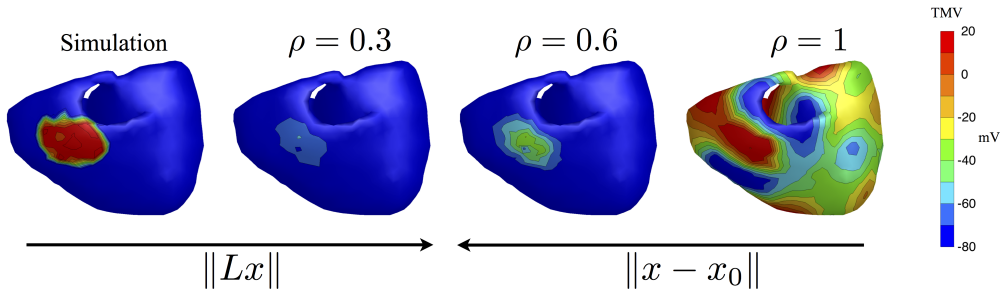

Figure 9.3: Simulated and reconstructed TMV for fixed near-optimal λ and increasing ρ parameters.

were detected as heart nodes with the largest TMV value, which resulted in localization errors of 16.0 ± 10.9 mm with maximal error of 39.1 mm for a posterior RV epicardial ectopic beat. Septal extrasystoles could not be correctly localized. Besides, no distinction between endocardial and epicardial origin was possible, as solutions were biased towards epicardium.

9.3.4 Discussion

With regard to the developed methodology, the complex optimization framework introduced in [118] delivered 'one-shot' reconstructions very similar to those obtained with its simplified version (9.23). However, an advantage of the complex approach consists in the possibility of coupling TMV with EP. Furthermore, an optimization formulation of the ECG inverse problem provides an opportunity of incorporating any kind of available data, e.g. pacing position, intracardiac electrograms, into the solution scheme in a flexible way. This algorithm could be extended to other pathologies by adapting the initial estimate x_0. In addition, spatio-temporal solution behavior could be regularized by modifying ρ parameter.

Although satisfactory localization accuracy was achieved, further investigations on optimal regularization operator and possible coupling of the proposed scheme with local imaging introduced previously should be undertaken.

9.4 Sparse Reconstructions: L_1 and L_0-Norm Regularization

In case regularization matrix is built by a discrete derivative operator, its pseudo-inverse approximates an integral operator and acts as a low-pass filter [119]. This property together with penalty-term minimization in L_2 sense inherently leads to a smooth solution.

However, depolarization front in a human heart exhibits a thickness of approximately 0.4 mm. Projecting arising potentials onto a heart model employed for the inverse calculations (average node distance $\sim$ 6-10 mm) would result in step-like source distributions. In order to achieve this effect and emphasize solution features lost due to over-smoothing, total variation or L_1-norm of the penalty term should be minimize [120–122].

In the inverse problem of ECG, L_1-norm regularization based on total variation minimization and gradient projection was demonstrated to have superior performance over standard Tikhonov reconstructions of EP [123, 124]. Furthermore, novel sparse reconstruction al-

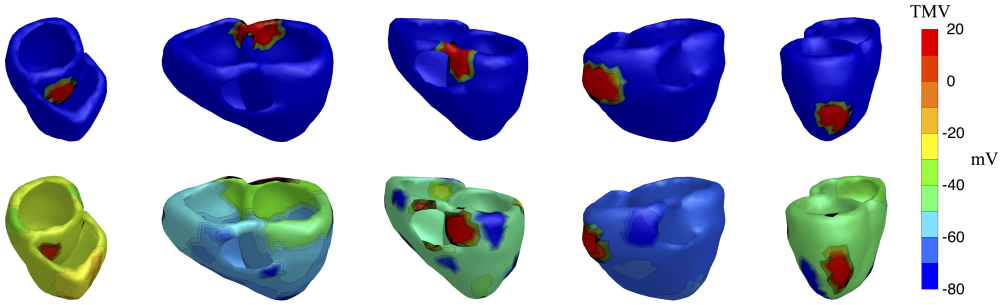

Figure 9.4: Reconstruction examples for L_1-norm minimization.

gorithms for localizing infarction and ischemia regions in terms of volumetric TMV were introduced in [125–127].

In the present work, performance of L_1-norm regularization with a gradient operator as penalty matrix is evaluated.

9.4.1 L_1-norm regularization

In order to assess the performance of L_1-norm based regularization for PVC localization, reconstructions were conducted for time step ($t = 30$ ms) corresponding to QRS onset. The gradient operator G was constructed in the following way: number of rows in G was equal to the number of edges in the discretized geometry. Two non-zero entries per row $G(i, j_1) = 1$ $G(i, j_2) = -1$ corresponded to the nodes j_1 and j_2 connected by an edge i.

9.4.2 L_0-norm regularization

L_0-norm of a vector is equal to the number of its non-zero components. Therefore, applied to the TMV-based inverse problem of ECG, regularization in L_0 sense implies sparse reconstruction of sources in some basis. In the present work, the basis, or dictionary, was created in the following way: first, the heart was subdivided into $d = 100$ parts. Subsequently, TMV for nodes from each part were assigned to the value of a depolarized cell ($+20$ mV) that was intended to resemble a PVC at an initial time instance. Then, an L_0-norm regularized solution $\alpha \in \mathbf{R}^{100\times 1}$ would ideally have almost all but a few non-zero components in the dictionary D. Examples of dictionary basis vectors are provided by Fig. 9.5.

As L_0-norm optimization is non-convex NP problem, usually L_1 relaxations are considered instead. For this work, greedy analysis pursuit algorithm was employed [128]. Within this approach, the problem is formulated as follows:

$$\begin{aligned} \alpha &= \min_{\alpha} ||\Omega\alpha|| \\ \text{subject to} \quad & AD\,\alpha = y \end{aligned} \tag{9.24}$$

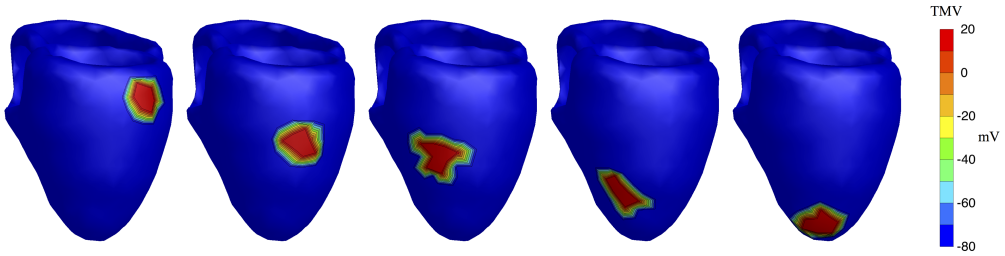

Figure 9.5: Dictionary basis vectors used for sparse reconstructions. Each PVC at an initial time step was approximated as a linear combination of the columns from dictionary matrix.

Cosparsity of the signal α is defined as $l = d - \|\Omega\alpha\|_0$, which corresponds to the number of zero elements in α. From the cosparsity concept, a vector called cosupport Λ is defined to contain indexes of the zero elements in $\Omega\alpha$.

The greedy analysis pursuit algorithm consists in finding of the cosupport for a cosparse signal α [129]. According to the adopted dictionary, Ω was set to identity matrix, vector α was initialized as zero vector. Therewith, all indexes were included into initial estimation of the cosupport vector Λ.

The problem (9.24) can be, then, solved by the following procedure:

Algorithm 9.1 GAP algorithm

$t > 0$ (input parameter)
$\eta > 0$ (input parameter)
$\varepsilon > 0$ (input parameter)
$k = 0$
$\alpha_0 = \{0, 0, ..., 0\}$ initial estimation
$\Lambda_0 = \hat{\Lambda}^0 = \{1, 2, 3, \cdots, d\}$
$\hat{\alpha}_0 = \begin{bmatrix} AD \\ I_{\hat{\Lambda}_0} \end{bmatrix}^{\dagger} \begin{bmatrix} y \\ 0 \end{bmatrix}$
repeat
    $k = k + 1$
    $\beta = I\hat{\alpha}_{k-1}$
    find the largest entries in β: $\Gamma_k = \{i : |\beta_i| \geq t \max_j |\beta_j|$
    $\hat{\Lambda}_k = \hat{\Lambda}_{k-1}/\Gamma_k$
    $\alpha_k = \begin{bmatrix} AD \\ I_{\hat{\Lambda}_k} \end{bmatrix}^{\dagger} \begin{bmatrix} y \\ 0 \end{bmatrix}$
until $||I_{\hat{\Lambda}_k}\hat{\alpha}_k||_\infty < \varepsilon$

The parameter t determining the number of rows removed in each iteration was set to 2. Performance of the algorithm was, however, robust with respect to variations in t.

9.4.3 Results

Determination of an optimal regularization parameter in L_1-norm regularization is a challenging problem. As no automatic method with satisfactory performance was found, the

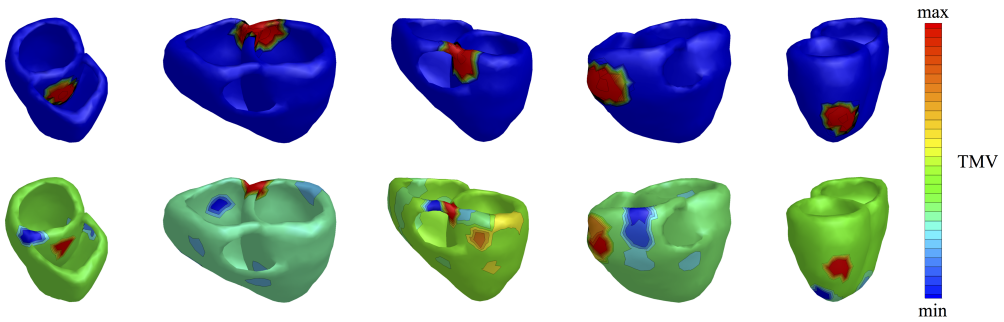

Figure 9.6: Reconstruction examples for L_0-norm minimization.

optimal parameter was chosen a-posteriori to deliver the best solution in the considered metric. A range of λ parameters was tested for solving the inverse problem. For each solution, distance from the true origin to the node with highest TMV value was computed. For L_0 regularization, the center of mass of a found cardiac part was assumed to be the reconstructed origin.

For L_1-norm minimization, localization errors were 14.3 ± 15 mm with one outlier of over 50 mm for a septal PVC. Septal extrasystoles could not be correctly detected. Furthermore, solutions were biased towards the epicardial surface. Exemplary reconstruction results for $\|L_1\|$ regularizaiton are illustrated in Fig. 9.4.

L_0-norm regularization resulted in errors of 16.4 ± 12.1 mm. Two out of 5 septal extrasystoles were localized correctly. Exemplary reconstruction results for $\|L_0\|$ regularizaiton are illustrated in Fig. 9.6.

9.4.4 Discussion

The present study assessed performance of sparse reconstructions for PVC localization. Endocardial and septal events could not be correctly identified and might be improved by proper weighting of regularization and transfer matrices. Errors for L_0-norm regularization were slightly higher than for L_1-norm, which could be partially explained by the nature of the considered dictionary.

Furthermore, several different approximations of the gradient operator were tested and the obtained results were found to strongly dependent on the regularization matrix used.

9.5 Binary Optimization

Nonsmooth regularization approaches to the ECG inverse problem were demonstrated to result in more realistic solutions compared to a classical Tikhonov method (e.g. [130–132]). Starting from a standard (smooth) regularization scheme, several steps in the development of algorithm can be accentuated. First, improvement of the reconstruction quality for Tikhonov solution can be achieved by adding constraints on the solution range. In Fig. 9.7, a standard

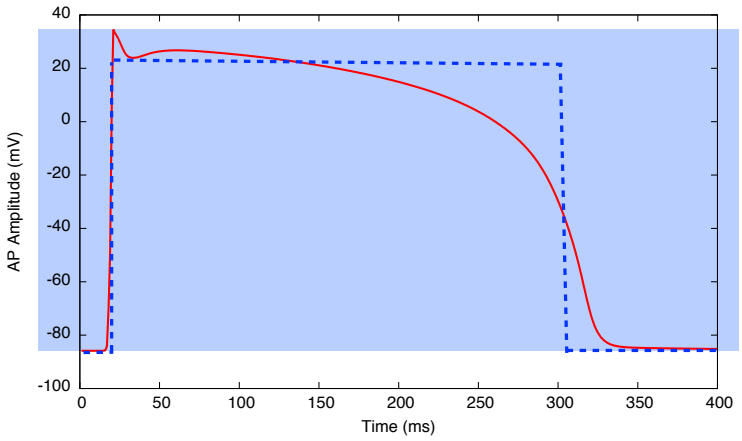

Figure 9.7: An exemplary action potential (AP) of a heart cell is drawn in red.The admissible solution space is highlighted; the blue dashed line shows a possible binary solution behaviour of the TMV.

action potential curve is plotted. TMV values lie in a certain interval that is highlighted with blue, which is characteristic for all cardiac cells independent on possible pathologies.

In case of including corresponding non-equality constraints into the formulation, one arrives at an optimization problem that could be treated with appropriate convex optimization methodologies, e.g. conic optimization, semi-definite programming etc. [133]. On one hand, the inverse problem can be solved sequentially in time with the introduced spatial constraints. An alternative method described in Chapter 4 consists in adding spatio-temporal dependency by imposing nondecreasing behaviour in the time domain [134].

These approaches penalize the regularization term in L_2-norm that could sometimes lead to over-smoothed solutions. Depolarization process in a cell is, however, a fast process which is reflected in the upstroke of TMV (see Fig. 9.7). This stage is followed by a plateau phase during which the TMV could be assumed to have a constant value. This property justifies the application of a step-like function for nonlinear activation times imaging [30, 135].

Applying similar logic to the potential-based inverse problem, a classical Tikhonov regularization functional can be reformulated as an unconstrained binary quadratic optimization problem (UBQP):

$$\begin{aligned} x = \arg\min_x F(x) = \arg\min_{x\in[l,u]^n} \|Ax-y\|_2^2 + \lambda\|Lx\|_2^2 = \\ = x^T(A^TA + \lambda L^TL)x - 2A^Tyx = x^TQx + qx \end{aligned} \tag{9.25}$$

where l and u define the binary values every heart node potential can take, n is the problem dimension.

Although the number of possible solutions (2^n) is finite, application of exact algorithms [136, 137] becomes computationally infeasible for increasing n. Due to high practical importance of the UBQP, a variety of heuristic techniques (e.g. tabu search [138, 139], simulated annealing [140, 141], population-based approaches [142–144]) has been proposed for its solving.

For the ECG imaging of PVC localization, the difference of convex functions (DC) method [145, 146] was shown to deliver the best results [147].

9.5.1 Difference of convex functions (DC) algorithm

Optimization of a quadratic functional $F(x)$ in (9.25) generally leads to a smooth sources distribution. In order to force the optimization output to be binary, an additional multiplier constraint should be added:

$$F(x) = x^T Qx + qx + \mu \langle u - x, x - l \rangle \tag{9.26}$$

The introduced penalty term represents the scalar product between sought solution and the allowed binary values l and u. For a sequence of positive increasing relaxation parameters μ, the functional value is decreasing for all solution components move towards one of the favoured boundaries thus forcing the binary behaviour. In order to solve the arising optimization problem, the difference of convex (DC) functions algorithm was used [147].

9.5.1.1 DC programming

The functional (F) in 9.26 is not convex any more, which poses certain restrictions on the solution scheme [141]. Writing it as a difference of two convex functions results in what is known to be convex-concave regularization:

$$F(x) = g(x) - h(x), \tag{9.27}$$

with two convex functions defined as

$$g(x) = x^T Qx + qx + \chi_C(x) \tag{9.28}$$

$$h(x) = -\mu \langle u - x, x - l \rangle. \tag{9.29}$$

Whereby $\chi_C(x)$ is the characteristic (or indicator) function of the convex set $C = [l, b]^n$, i.e. it takes value 0 if point x is inside C and $+\infty$ otherwise.

Reformulated in this way, the original optimization problem reads as finding the infimum of convex functions difference [145]:

$$x = \inf_x \{g(x) - h(x)\}. \tag{9.30}$$

For elements x in vector space X, define the dual space Y to be the space of all linear functionals operating on $\mathbb{R}^n$. The conjugate of a convex function $h(x)$ is defined as:

$$h^*(x) = \sup_y (\langle x, y \rangle - h(y))$$

Therefore, problem (9.30) can be rewritten in terms of conjugate functions:

$$\begin{aligned} &\inf_x \{g(x) - h(x)\} = \inf_x \{g(x) - \sup_y \{\langle x, y \rangle - h^*(y)\}\} = \\ &= \inf_x \inf_y \{g(x) - [\langle x, y \rangle - h^*(y)]\} = \inf_y \{h^*(y) - g^*(y)\} \end{aligned} \tag{9.31}$$

which poses the problem dual to (9.27). The primal-dual subgradient algorithm was used for solving this set of equations [148]. Algorithm 9.2 represents the solution scheme constituting the core of the DC approach (the algorithm scheme is adapted from [147]). According

Algorithm 9.2 Primal-dual subgradient algorithm

1: initialize x_0
2: **for** $k = 0, 1, \ldots$ **do**
3: $\quad y^k \in \partial h(x^k)$
4: $\quad x^{k+1} \in \partial g^*(y^k)$
5: **end for**

to [148], the sequences $\{x^k\}, \{y^k\}$ are well-defined and $\{g(x^k) - h(x^k)\}$ is decreasing with every limit point of $\{x^k\}$ being also a critical point of the optimization functional $g - h$. Generally, the subgradient ∂h of a convex function h is defined as follows [149]:

$$\begin{aligned} \partial h(\bar{x}) &= \{y \mid h(x) \geq h(\bar{x}) + \langle y, x - \bar{x} \rangle, \forall x\} = \\ &= \arg\max_y \{\langle y, \bar{x} \rangle - h^*(y)\}. \end{aligned} \tag{9.32}$$

Directly from the definition, it follows that

$$\inf_x \{h(x)\} \geq \inf_x \{h(x^k) + \langle y^k, x - x^k \rangle\}$$

which leads to the following infimum estimate of the optimization functional

$$\inf_x \{g(x) - h(x)\} \leq \inf_x \{g(x) - [h(x^k) + \langle y^k, x - x^k \rangle]\} \tag{9.33}$$

Using (9.32), one can show that every subsequent iteration point x^{k+1} minimizes the expression on the right-hand side of this inequality [146]:

$$\begin{aligned} x^{k+1} \in &\arg\inf_x \{g(x) - [h(x^k) + \langle y^k, x - x^k \rangle]\} = \\ &= \operatorname*{argmax}_x \{\langle y^k, x - x^k \rangle - g(x) + h(x^k)\} := \partial g^*(y^k) \end{aligned}$$

Similar, an expression for the y^k update can be obtained:

$$\partial y^k = h(x^k) = \arg\min_y \{h^*(y) - [g^*(y^{k-1}) + \langle x^k, y - y^{k-1} \rangle]\} \tag{9.34}$$

As function h is convex and smooth, $\partial h(x) = \nabla h(x)$. Therefore,

$$y^k = \nabla h(x^k) = 2\mu x^k - \mu(u + l) \tag{9.35}$$

Function g is convex but non-smooth due to the convex set constraints $x \in C$. Hence, the update x^{k+1} is calculated as follows:

$$x^{k+1} = \arg\min_x \{g(x) - \langle y^k, x \rangle\} \tag{9.36}$$

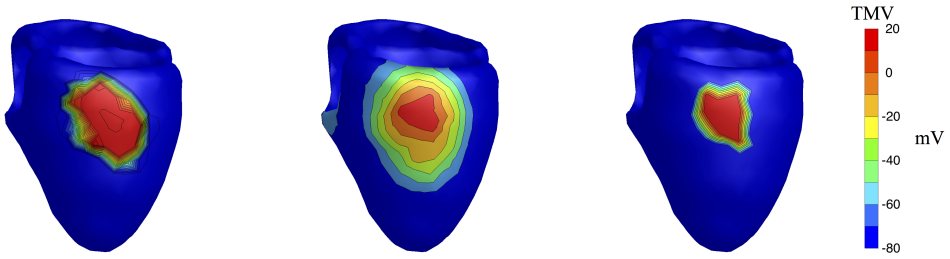

Figure 9.8: Behavior of the DC algorithm. From left to right: simulated TMV; the first (smooth) Tikhonov reconstruction corresponding to $\mu = 0$; the first DC iteration corresponding to $\mu = 0.05$ - the solution converged to a binary one.

Recalling definition of g and C, the task of finding x^{k+1} becomes to be a familiar inequality constrained optimization problem:

$$x^{k+1} = \arg\min_x x^T Qx + (q - y^k)x \qquad (9.37)$$
$$l \leq x^{k+1} \leq u$$

The resulting structure of the DC method is provided by Algorithm 9.3 [146].

Algorithm 9.3 DC binary algorithm

$\mu = 0$ - no binary constraints
input parameters $\Delta\mu, \varepsilon_{in}, \varepsilon_{out}$
initialize x^0
repeat
  repeat
    $y^k = \nabla h(x^k, \mu)$
    $x^{k+1} = \arg\min_x \{g(x) - \langle y^k, x\rangle\}$
  until $|x_{k+1} - x^k| \leq \varepsilon_{in}$ (inner loop)
  $\mu = \mu + \Delta\mu$
until $sup\{min(u - x^{k+1}, x^{k+1} - l)\} \leq \varepsilon_{out}$ (outer loop)

The initial parameter $\mu = 0$ implies that the first estimate x^1 coincides with the constrained Tikhonov solution and the quality of the final reconstruction is dependent on this smooth approximation. In Fig. 9.8, an exemplary behavior of the DC method is demonstrated: simulation, the first (smooth) and second (binary) iterations are shown for a right ventricular PVC for time step $t = 30$ ms after the excitation onset. Speed of convergence is regulated by parameter $\Delta\mu$, which was set to 0.05 in the present work [147]. The outer loop is exited when the differences between iterative solution and binary values l, u become smaller than a predefined threshold ε_{out}. The stopping criteria $\varepsilon_{out}, \varepsilon_{in}$ were set to 10^{-3}.

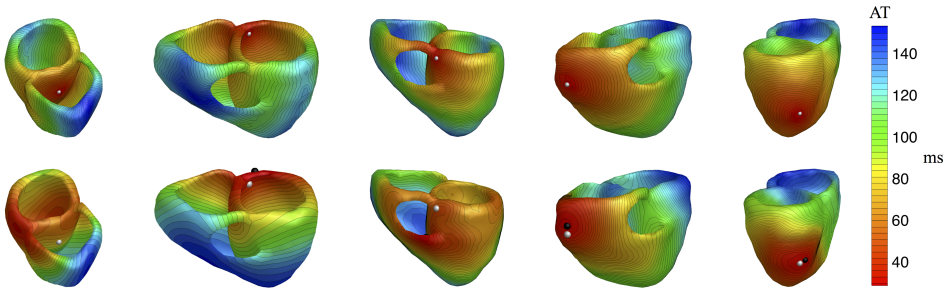

Figure 9.9: Exemplary reconstructions with the DC algorithms.

9.5.2 Results

The inverse problem was sequentially solved for all time steps within the QRS complex. From the computed TMV, AT were as previously derived with a spatio-temporal algorithm [45].

Mean localization errors were 21.9 ± 15.1 mm error. As mentioned before, final reconstruction quality depended on the initial estimate provided by Tikhonov regularization. For each consecutive iteration step, solution from previous iteration was used as initial estimate, which significantly speeded up the convergence and revealed robustness of the binary approach with respect to regularization parameter λ.

9.5.3 Discussion

In this study, the performance of a DC method for binary regularization was evaluated. Although being dependent on a smooth solution provided by Tikhonov method, binary optimization resulted in efficient 'filtering' of low-frequency components and led to physiologically more meaningful reconstructions. Consecutive solution for all time steps was observed to exhibit more robust performance against uncertainty in regularization parameter λ compared to Tikhonov regularization. The proposed scheme could be easily extended to a binary analogue of spatio-temporal algorithm imposing nondecreasing constraints on TMV as described in Chapter 4.

CHAPTER 10

ECG Imaging for PVC Localization: *in silico* Study

The assumption of equal anisotropy ratios in the intra- and extracellular heart domains underlying the equivalent dipole layer (EDL) model does not reflect the reality. In the present study, localization errors for noninvasive surface TMP-based imaging of ventricular extrasystoles are quantified. 20 ectopic beats starting from endo-, epicardial and septal regions of the heart were simulated with the monodomain. In the forward calculations, ECG were computed for a realistic volume conductor with an anisotropic bidomain model of the heart for three setups of cardiac conductivity tensors: isotropic, equal anisotropy ratios and unequal anisotropy ratios in the intra- and extracellular spaces. For the inverse reconstructions, the fastest route algorithm (FRA) and the spatio-temporal method imposing nondecreasing temporal behavior on TMV were used.

10.1 Introduction

Though a unique linear relation between volumetric TMV and BSPM exists, basic physics suggests that there is an infinite number of source configurations producing identical electrocardiograms. To some extent, this problem can be overcome by applying proper regularization strategies [33, 36, 150–152]. Another way to moderate the problem is to restrict the solution to the heart surface.

In this case, the noninvasive cardiac imaging is not underdetermined but still remains a severely ill-posed problem. For source modeling, two popular approaches are the epicardial potential model (e.g. [25, 153, 154]) and the equivalent dipole layer model [155, 156]. In the former, the volumetric current sources are usually replaced by electric potentials on a surface encompassing the complete heart (the pericardium). This is done rather from practical considerations than due to theoretical limitations of the model. With suitable spatio-temporal regularization, one can also image the endocardial part of the heart surface [46]. The surface TMP model represent the sources by a current dipole layer situated on the myocardial surface, including endo- and epicardial parts.

According to the EDL theory, an electric potential generated by a three-dimensional source distribution is equal to the potential produced by a dipole layer on the heart surface. The dipole strength is proportional to the local TMP. However, this equivalence holds true only under certain assumptions on the cardiac electrical conductivities. In his first work, Geselowitz showed equivalence of the EDL model and three-dimensional current sources for the isotropic intra- and extracellular conductivities [157]. Thereafter, the validity domain of the EDL was extended to the case of equal anisotropy ratio, i.e. when the ratio between conductivities along and orthogonal to the fiber direction is equal for the intra- and extracellular domains [17]. But even this assumption does not fully reflect the reality. In [158, 159], it was shown that the excitation front as well as therewith associated electric potentials in the body volume conductor are strongly affected by the myocardial fiber structure. On the other hand, practical challenges in generation of the patient-specific fiber orientation models and desired real-time clinical applicability of the ECG imaging require investigations on validity of the EDL model approximation.

The purpose of the present study is to quantify localization errors resulting from the surface source model for noninvasive imaging of realistic BSPM produced for a range of anisotropy ratios in the bidomain formulation [160].

10.2 Methods

10.2.1 Simulation Setup

The volume conductor model and the simulation setup used for this study are described in detail in Chapter 8. Note that for analysis of the proposed methods in Chapter 9, BSPM resulting from the assumption of unequal anisotropy ratios in the heart were considered.

For the present study, electrocardiograms were simulated for three bidomain conductivity scenarios corresponding to:

- isotropic case
- equal anisotropy ratios
- unequal anisotropy ratios

in the intra- and extracellular domains. All BSPM were contaminated with white Gaussian noise of 30 dB.

The intra- and extracellular conductivity values for FEM as well as heart conductivity for BEM are provided in Table 10.1. For all cases, the bulk conductivity in the BEM model was equal to the sum of extra- and intracellular conductivities (σ_e and σ_i) for the isotropic FEM. The anisotropic FEM bidomain conductivity values with unequal ratios are in agreement with the literature [97, 161]. The values for the isotropic and equal anisotropy cases are based on the extra- and intracellular conductivity values in the transversal direction for the unequal anisotropy ratio case. For the equal anisotropy ratio, longitudinal conductivities in both extra- and intracellular spaces ($\sigma_{e,l}$ and $\sigma_{i,l}$) were set to be 3 times higher than those

Table 10.1: The bulk conductivity values (S m^{-1}) for the heart used in the performed calculations.

Tissue type	Conductivity [S m^{-1}]
Heart BEM	0.2
Heart FEM isotropic	$\sigma_{e,t} = \sigma_{e,l} = 0.15$ $\sigma_{i,t} = \sigma_{i,l} = 0.05$
Heart FEM equal anisotropy ratio	$\sigma_{e,t} = 0.15$ $\sigma_{i,t} = 0.05$ $\sigma_{e,l}/\sigma_{e,t} = \sigma_{i,l}/\sigma_{i,t} = 3$
Heart FEM unequal anisotropy ratio	$\sigma_{e,t} = 0.15$ $\sigma_{i,t} = 0.05$ $\sigma_{e,l}/\sigma_{e,t} = 3$ $\sigma_{i,l}/\sigma_{i,t} = 9$

in the transversal direction ($\sigma_{e,t}$ and $\sigma_{i,t}$). For the unequal anisotropy case, this ratio was assigned to 3 and 9 in extra- and intracellular domains, respectively.

10.2.2 Inverse Calculations

For the inverse reconstructions, two spatio-temporal state-of-the-art methods were used. The fastest route algorithm (FRA) and the approach imposing nondecreasing constraints on the temporal behavior of the TMP. FRA, which is usually utilized together with the following nonlinear optimization, was considered on its own without further fine-tuning of the test activation sequences. FRA-simulated activation excitation starting from each node of cardiac geometry was converted to the ECG that was afterwards compared to the reference electrocardiogram. The test sequence delivering the highest correlation between the simulated and 'measured' BSPM was assumed to be the best solution candidate. For the considered FRA-based method, the conduction velocities were set to 1 and 0.32 mm/ms in the tangential and normal directions with respect to the heart surface. Recall that the monodomain simulations resulted in a longitudinal conduction velocity of approximately 0.65 m/s.

For the optimization algorithm employing the property of TMP being a nondescreasing function in the time domain during the depolarization phase, reference BSPM were first down-sampled with rate of 8 ms, i.e. each 8th time step was used to construct the BSPM matrix for the due optimization. To calculate AT from the reconstructed TMV, a spatio-temporal algorithm proposed by Erem *et al.* [45] was used.

For better comprehension of the results and interpretation of algorithms performance in dependence on focal origin, a short overview of considered PVC locations is provided: 1) left side of septum; 2) right side of septum; 3) posterior base LV near septum; 4) posterior base RV near septum; 5) epicardial free wall LV; 6) endocardial free wall LV; 7) endocardial anterior free wall RV; 8) epicardial anterior free wall RV; 9) anterior endocardial base LV

near septum; 10) anterior epicardial base LV near septum; 11) endocardial apex LV; 12) endocardial apex RV; 13) epicardial posterior free wall RV; 14) endocardial posterior free wall RV; 15) epicardial free wall RV; 16) endocardial free wall RV; 17) lower septum LV; 18) lower septum RV; 19) posterior endocardial apex LV; 20) posterior epicardial apex LV.

The inverse reconstructions were performed for all setups of myocardial conductivities. For the ECG generated for the cases of isotropic conductivities, equal and unequal anisotropy ratios, the BEM transfer matrix with isotropic conductivities assumption was used. For the case of unequal anisotropy ratio, performance of the 'anisotropic' FEM transfer matrix calculated was also tested. Therewith, the BEM transfer matrix corresponds to a realistic scenario of neglecting the myocardial fiber structure, whereas the results obtained with the FEM matrix represent the best-case scenario.

10.3 Results

10.3.1 FRA-based Reconstructions

For the BSPM simulated with isotropic conductivities, the mean localization error was 13.2 ± 8.5 mm with the maximal error of 28.7 mm for the ectopic beat originating from endocardial free wall in the RV (pattern 16). In 15 cases, ectopic beats were localized within 20 mm from the true origin. In two cases, perfect focus location was found. For patterns 11, 13 and 16, 17, the beats were incorrectly localized when the question of their endo- or epicardial origin was concerned.

For the anisotropic cases with equal anisotropy ratios, the mean reconstruction error was 12.6 ± 8.4 mm with the maximal error of 28.7 mm for the same excitation pattern 16. In 16 cases, ectopic beats were localized within 20 mm from the true origin. In three cases, perfect reconstruction was achieved. The results were very similar to those from the isotropic setup. It was the pattern 3 that contributed to a slightly better statistic compared to the isotropic setup (14.8 vs. 21.0 mm localization errors). For patterns 11, 13, 16, 17 and 19, the foci were localized on the wrong part of the heart surface with respect to their endo-/epicardium.

The reconstruction errors for the unequal anisotropy ratios case constituted 13.1 ± 6.8 mm with the maximal error of 24.3 mm. No foci were localized precisely. In 16 cases, ectopic beats were located within 20 mm from the true earliest activation site. Patterns 9 and 10 resulted in errors of over 20 mm for all considered conductivity setups. Patterns 1, 11, 12, 13, 16 and 17 resulted in incorrect localization when the question of their endo-/epicarial origin was considered.

As expected, inverse reconstructions performed with the FEM-generated transfer matrix resulted in the smallest localization errors of 10.8 ± 7.2 mm. The maximal error of 21.5 mm was observed for pattern 12. In 18 cases, the localization accuracy was better than 20 mm. Four ectopic origins could be found precisely. For patterns 11, 12, 14, 15, 17 and 19, however, the ectopic foci were incorrectly localized with respect to their endo-/epicardial origin.

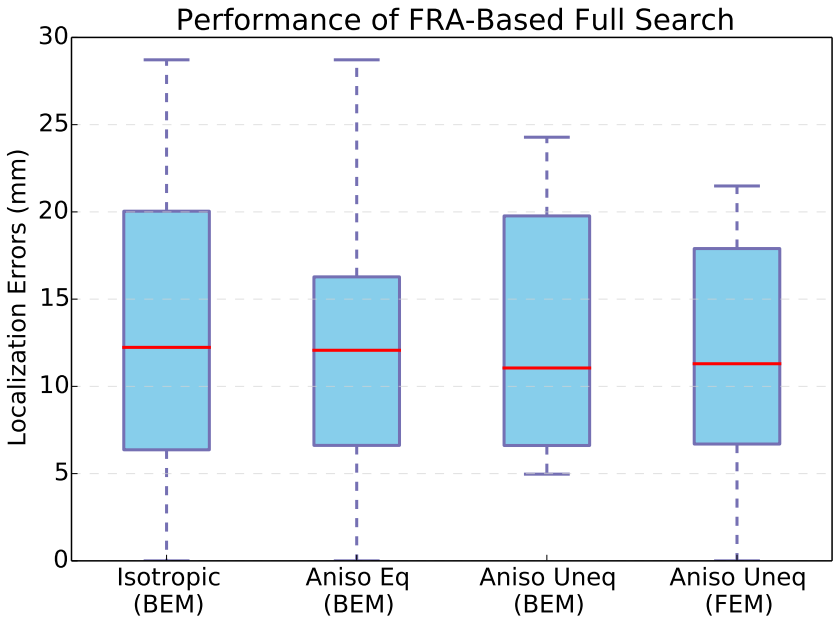

Figure 10.1: Localization errors of the FRA-based inverse reconstructions. The results are shown for all types of myocardial conductivity tensors used in the forward calculations: isotropic, anisotropic with equal anisotropy ratio (aniso equal), anisotropic with unequal anisotropy ratio (aniso unequal). In parenthesis, the type of transfer matrix used for the inverse calculations (BEM or FEM) is indicated.

The summary on the localization errors obtained with FRA-based full-search for all considered excitation patterns and myocardial conductivties setups is given by Fig. 10.1. Exemplary correlation coefficients maps delivering information on the achieved solution uncertainty are shown in Fig. 10.2.

10.3.2 Performance of Constrained Optimization Algorithm

For the BSPM resulting from isotropic conductivities assumption, localization accuracy was 7.7 ± 4.7 mm with the maximal error of 14.2 mm for pattern 6. Four excitation sites could be localized precisely. Patterns 6, 7, 11, 12, 13, 16 and 19 resulted in incorrect reconstruction of activation origin to be either on epi- or endocardium.

In case of anisotropic forward calculations with equal anisotropy ratios, the localization error constituted 5.6 ± 4.2 mm with maximal error of 11.6 m for pattern 6. Six foci were perfectly reconstructed. For patterns 1, 3, 4, 6, 9, 11, 12, 14, 16 and 17, the earliest excitation sites were localized on the wrong part of the heart surface. In these cases, endocardial foci were reconstructed to lie on the epicardium.

For the BSPM computed under unequal anisotropy ratios assumption, the average localization error was 9.3 ± 4.7 mm. The maximum of 23.7 mm was observed for pattern 14 corresponding to the focus originating on the RV endocardial posterior free wall. One earliest excitation site could be precisely located. Similar to the equal anisotropy ratio case,

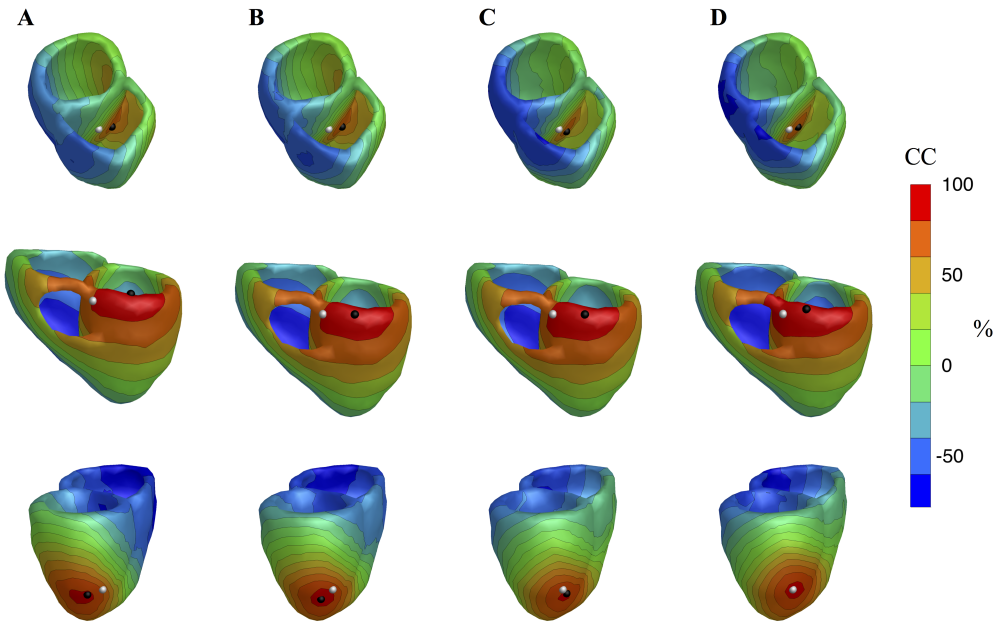

Figure 10.2: FRA-computed correlation values for each node in the ventricular mesh. Upper row: pattern 2, middle row: pattern 10, lower row: pattern 20. Column A: CC values for BSPM calculated with isotropic conductivities, inverse full-search performed with BEM transfer matrix; Column B: CC values for BSPM calculated for equal anisotropy ratios in intra- and extracellular conductivities, inverse full-search performed with BEM transfer matrix; Column C: CC values for BSPM calculated for unequal anisotropy ratios in intra- and extracellular conductivities, inverse full-search performed with BEM transfer matrix; Column D: CC values for BSPM calculated for unequal anisotropy ratios in intra- and extracellular conductivities, inverse full-search performed with FEM anisotropic transfer matrix.

patterns 1, 3, 4, 6, 9, 11, 12, 14, 16, 17 were falsely identified to have the epicardial origin. In addition, pattens 7 and 19 were incorrectly localized to have epicardial breakthrough.

In the best-case scenario of the FEM transfer matrix computed with anisotropic conductivities, the localization error was comparable to other setups resulting in 5.8 ± 4.0 mm with maximum of 14.3 mm for pattern 18. Five foci locations were reconstructed precisely. Patterns 3, 4, 6, 7, 12, 14, 16, 17 and 18 failed to identify the endocardially originated foci and resulted in the epicardial earliest activation sites.

The overview of all obtained results is provided by Fig. 10.3. In Fig. 10.4, exemplary reconstructions for activation patterns 2, 10, 20 are visualized.

10.4 Discussion

In the present model-to-model study, performance of two state-of-the-art spatio-temporal regularization approaches was evaluated. For the analysis, three setups of bidomain myocardial conductivities (isotropic, equal and unequal anisotropy ratios) for the forward calculations and two transfer matrices (isotropic BEM and anisotropic FEM) for the inverse computations were considered. This study showed that the EDL-based inverse procedures allow reconstruc-

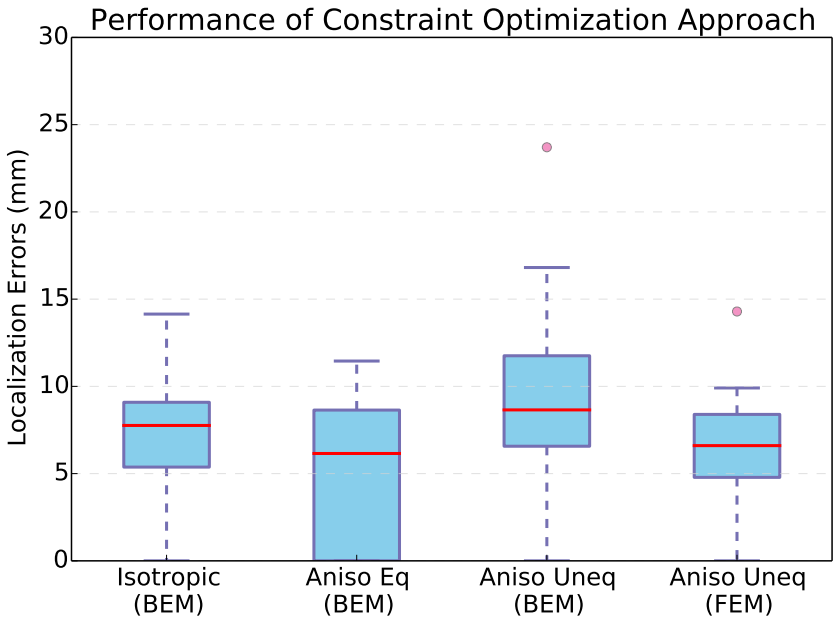

Figure 10.3: Localization errors (in mm) of the inverse reconstructions for the spatio-temporal algorithm with nondescreasing constraints on TMP. The results are shown for all types of myocardial conductivity tensors used in the forward calculations: isotropic, anisotropic with equal anisotropy ratio (aniso equal), anisotropic with unequal anisotropy ratio (aniso unequal). In parenthesis, the type of transfer matrix used for the inverse calculations (BEM or FEM) is indicated.

tion of activation times without taking the cardiac anisotropy into account. Computationally fast rule-based FRA method resulted in 80% of localization errors being <20 mm.

As expected from work of Geselowitz [17], localization errors obtained for the equal anisotropy ratios case were very similar to those resulting from BSPM computed with isotropic conductivities assumption. In the FRA-based reconstructions, patterns 11, 13, 16 and 17 were localized on the wrong part of the heart surface for both conductivity setups. These activation sequences corresponded to ectopic beats originating from LV endocardial apex, RV epicardial posterior free wall, RV endocardial free wall and LV lower septum respectively. For the unequal anisotropy ratios case in combination with BEM-based inverse reconstructions, pattern 1 was added to the list of missclassified foci (LV septum localized as RV septum). Although, localization accuracy of imaging with the FEM-generated transfer matrix was slightly superior compared to the isotropic BEM calculations, the wrong endo-/epicarial origins were identified for six patterns. In addition to the mentioned patterns 11 and 17, sequences 12, 14, 15, 19 were missclassified. The corresponding focal sites were situated on RV endocardial apex, RV endocardial posterior free wall, RV epicardial free wall and LV posterior apical endocardium. This analysis confirmed challenges arising from reconstruction of septal activities as reported in [46, 162]. Difficulties due to the beats starting from RV free wall can be partially explained by a much thinner RV wall in the used heart model. Furthermore, the endocardial apical parts with adjacency of septum and other ventricle seem to represent a challenge for the rule-based FRA as well.

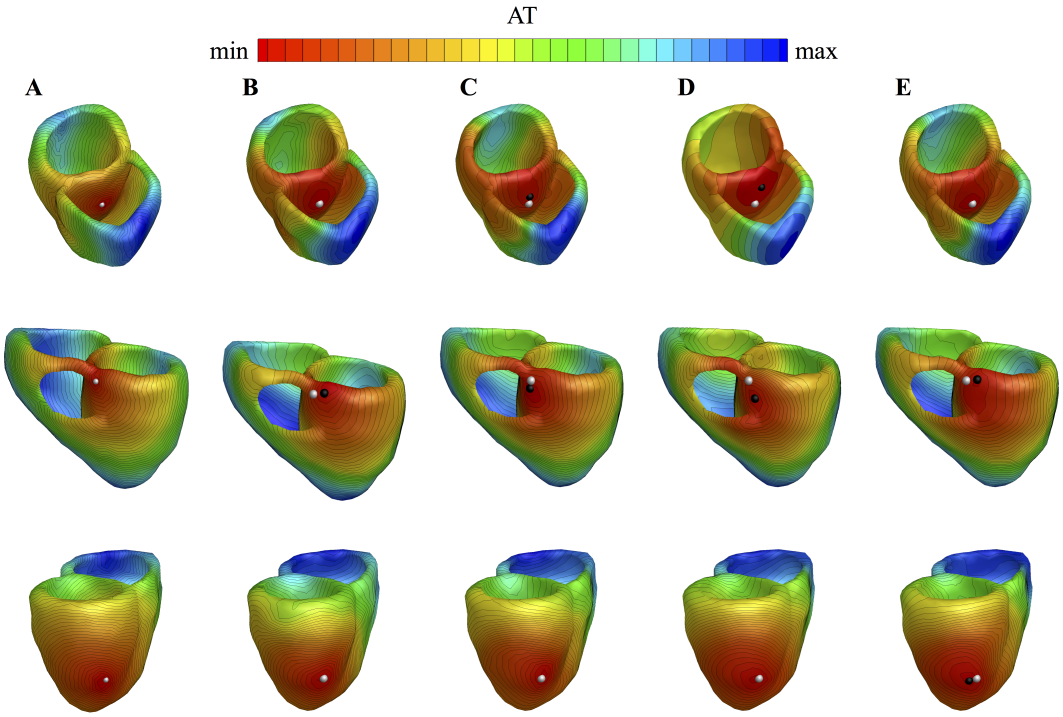

Figure 10.4: Simulated and reconstructed activation times. Upper row: pattern 2, middle row: pattern 10, lower row: pattern 20. Column A: simulated activation times (AT); Column B: BEM-reconstructed AT for BSPM calculated with isotropic conductivities, origins for patterns 2 and 20 localized precisely; Column C: BEM-reconstructed AT for BSPM calculated for equal anisotropy ratios in intra- and extracellular conductivities, origin for pattern 20 localized precisely; Column D: BEM-reconstructed AT for BSPM calculated for unequal anisotropy ratios in intra- and extracellular conductivities, origin for pattern 20 localized precisely; Column E: BEM-reconstructed AT for BSPM calculated for unequal anisotropy ratios in intra- and extracellular conductivities, origin for pattern 2 localized precisely.

For the reconstructions obtained with the spatio-temporal optimization algorithm and nondecreasing constraints on the TMP, the average errors for all conductivity cases were smaller than those resulting from the FRA-based solutions. Errors across the conductivity setups were very similar and performance of the FEM-based transfer matrix was only slightly superior for unequal anisotropy ratios compared to the isotropic BEM lead-field matrix. However, despite the overall better localization accuracy, the number of missclassified origins with respect to their endo-/epicardium location increased compared to the FRA approach. Patterns 3, 4, 6, 7, 12, 14, 16, 17 and 18, all corresponding to endocardial earliest excitation sites, were falsely identified to have epicardial origin according to the best-case anisotropic FEM scenario.

In [38], the effects of temporal dimensionality reduction on the performance of the considered spatio-temporal approach were evaluated. The study revealed that simple down-sampling of the problem does not influence the localization quality but can significantly reduce the computational time. However, another down-sampling approach with the hope for better classification of epi/endocardial events was tested. BSPM for the inverse optimization were constructed to contain each second time step from the first 30 ms of the QRS complex

and each 30th instance from the remaining depolarization interval. Obtained results were very similar to those presented in Subsection 10.3.2 without any improvement in the classification performance. On one hand, it implies that the Tikhonov method smooths the region of interest. Small ECG differences resulting from endo-/epicardial excitation origin are lost by the L_2-norm minimization and the epicardial sources are favoured due to bigger amplitude of the corresponding lead-fields. On the other hand, it suggests necessity of new reliable methods for AT estimation from the reconstructed potentials.

Concerning inverse methods, the ECG signal morphology at early time steps should be taken into account and integrated into the regularization scheme. With this regard, each of the two considered approaches revealed specific advantages and drawbacks. Overall localization accuracy was better for the constrained optimization approach. However, computational time of the full-search FRA-based procedure is in orders of magnitudes faster and does not require additional regularization parameters apart from the assumed CV. In contrast, an average computational time for the down-sampled optimization approach was in order of 1 h for each regularization parameter λ. A thorough analysis of computational time dependency on the sampling rate can be found in [38]. With continuous increase of available computational resources, this approach could become clinically feasible, but for the current stage, it is the FRA-based method that represents a tool for possible real-time applications of ECG imaging. Moreover, it can deliver certain information on uncertainties of the best solution candidate, which is impossible with deterministic Tikhonov-based optimization approaches.

10.4.1 Relation to Previous Works

In general, the presented results are in agreement with previously reported investigations on the AT imaging [83, 160] and reconstruction of the TMP [37]. Modre *et al.* examined the influence of cardiac anisotropy on the reconstruction quality for four different activation sequences: sinus rhythm, RV and septal pacings, sinus rhythm with pre-excitation. With this regard, there are several differences concerning the design of the study and methods used.

First, the AT distributions in the study reported by Modre *et al.* were simulated with a three-state cellular automaton [163]. Although serving a realistic model of the electrical excitation in the heart, this approach does not account for ion kinetic, whereas the monodomain simulations used in the present work are considered to be the current state-of-the-art [13]. Second, the previous work evaluated localization of a septal focus (basal part of the septal wall separating two ventricles) and an endocardial focus on the RV free wall. Here, the analysis was extended to 20 simulated beats originating from different parts of the heart and having endo- and epicardial origins. The present study demonstrated the ability of FRA to distinguish between the endo-/ epicardial sources in 15 out of 20 cases, whereby no subsequent ECG fine-tuning was performed. Third, critical point theorem was used in [83] for initializing the nonlinear AT imaging problem. Herewith, only FRA-generated sequences were employed. Overall, the FRA has been shown to produce superior results compared to the critical point initialization [41]. Finally, the forward and inverse computations presented in [83] were performed on meshes with a spatial resolution lower than those for this study,

which could have an immediate impact on the ill-posedness of the resulting problem. In [164], it was shown that increasing resolution on the heart can worsen numerical properties of the associated transfer matrix. Some direct suggestions on the spatial resolution to be used for ECG imaging are given in [165].

The simulation setup used here and the main goal of the work to investigate the influence of cardiac anisotropy on the AT reconstructions coincide with the motivation behind the study presented in [160]. However, there are certain differences to be mentioned. In [160], a normal sinus rhythm with four distinct points of early excitation was also considered. Furthermore, the initial FRA-based initialization was followed by the nonlinear optimization of AT. All inverse computations were performed by the researchers from Nijmegen, the Netherlands. Furthermore, localization errors as well as absolute differences in the first activation times, relative differences between the simulated and reconstructed values for AT and BSPM were analyzed. In the present work, localization accuracy was estimated only in terms of earliest activation point detection.

10.4.2 FRA-Based Initial Estimation

As discussed in [40], the result of nonlinear AT imaging problem is sensitive to the initial settings of CV values for tangential and transmural directions. These parameters affect only the activation order of transmural neighbours and in the case of isotropic propagation, all timings would be just scaled appropriately leading to results independent of the initial velocity value. With this respect, a more extensive full-search based on the rule generated FRA sequences could help to somewhat improve reconstruction results. In order to investigate variability of localization errors in dependence of initial CV values, the following test was performed: the tangential velocity values were chosen from the interval [0.8, 1.2] mm/ms with step 0.1 mm/ms. The transmural velocity ratios were set from the interval [1.6, 2.4] with step 0.2. Therewith, 25 CV setups were analyzed. The correlation-based reconstruction results showed only slightly better localization accuracy for several patterns. The misclassified cases were, however, not improved. Importantly, multiple setups of CV values resulted in the best possible reconstruction, which suggests robustness of the considered rule-based activation sequences produced with FRA.

Classically, the FRA initialized AT are subject to nonlinear optimization (e.g. [30]). Although it often does not significantly improve the AT and rather fine-tunes the relative differences between the measured and predicted BSPM, the improvement can be sometimes vital. Endo-epi change was observed for pattern 1 as evaluated for the study presented in [160]. Therefore, the final optimization remains an essential step in the whole noninvasive imaging pipeline. In contrast to the simple FRA full-search, it requires a more detailed anatomical model [166]. In future work, influence of the optimization step on the final localization accuracy for the considered simulation data should be investigated.

10.4.3 Inclusion of Cardiac Anisotropy

The presented results suggest that inclusion of anisotropy into the inverse calculations could improve the overall localization errors. At the same time, the success rate of beat classification with respect to their endo-/epicardial origin was very similar to the performance of isotropic BEM-based reconstructions.

Therefore, possible improvements in the noninvasive estimation of AT could be achieved by considering a more realistic conduction velocities profile. In the clinic, this information could only be obtained indirectly. Nevertheless, multiple pacings combined with simultaneously recorded BSPM could be used for adjustment of propagation parameters. Furthermore, in order to keep the inverse procedure as fast as possible, one can employ a cellular automaton (e.g. [163, 167]) model of an anisotropic heart and couple it with the BEM method for performing the forward calculations of electrical potentials in the body volume conductor [168].

Although the information on fiber structure can be obtained from cardiac diffusion MRI, this procedure is not integrated into the clinical routine. Despite recent progress [169], *in vivo* imaging of 3-D fiber architecture remains a challenging practical task. Besides, it remains unclear whether a rule-based cardiac fiber orientation would perform better than the isotropic assumption. Therefore, isotropic BEM for computing of BSPMs was considered to be the state-of-the-art method in clinical applications of ECG imaging.

CHAPTER 11

Clinical Application of ECG Imaging for PVC Localization

In this chapter, performance of the ECG imaging for PVC localization is evaluated in clinical context. The data acquisition and preprocessing were accomplished by Walther Schulze [35]. In his PhD thesis, W. Schulze also considered several ECG imaging techniques for reconstructing transmembrane voltages: Tikhonov-based methods reconstructing potentials for all time instances sequentially and two approaches involving temporal solution dynamics: maximum-a-posteriori method (MAP) and a simplified version of the fastest route algorithm (FRA). In the present work, performance of the 'classical' FRA approach and a constrained optimization algorithm is assessed for localization of PVC and ventricular pacing sites.

11.1 Introduction

Among the conventional noninvasive methods of arrhythmia detection, ECG is believed to provide the best initial estimation of the target for catheter ablation procedure [5]. With this regard, the goal of noninvasive ECG imaging is to bring the diagnostic and preinterventional treatment planning on a new level in terms of involved logistical efforts and financial costs.

Recently, ECG imaging begun moving towards its clinical applications. Tremendous progress of the technology has been facilitated by numerous validation studies conducted over the last years [8, 31, 154, 170, 171]. Results on noninvasive imaging of ventricular ectopic beats and pacing locations, which stays in focus of the present work, were reported for different source models: epicardial potentials (e.g. [172, 173]), epi- and endocardial potentials [46], TMV-based activation times [28, 44], current density [152, 174], transmembrane voltages (TMV) [35].

The goal of the present work is to extend the validation study performed by Walther Schulze in cooperation with the University Medical Centre Mannheim [35]. For this purpose, new, more complex, BEM geometries were created for solving the inverse problem of ECG. Furthermore, two additional spatio-temporal regularization approaches were considered for noninvasive localization of ventricular focal activities.

11.2 Methods

11.2.1 Patient Data

The clinical data used for validation of the inverse methods have been recorded in the scope of a joint project with the University Medical Centre Mannheim aiming at noninvasive imaging of ventricular ectopic activities. Within this study, data essential for ECG imaging were recorded for 10 patients undergoing catheter ablation procedure. For more details on data and its acquisition, reader is referred to the PhD thesis of Walther Schulze [35].

In his work, W. Schulze has created a processing pipeline that included BSPM and MRI acquisition, electrodes localization, meshes generation, rigid co-registration of the validation and anatomical data, BSPM and CARTO data post-processing [35]. For each patient, resulting quality of the complete dataset was evaluated based on the quality of single processing steps in the described work flow.

In the present work, only patients with good (according to [35]) data quality were considered for reconstructions. Based on this criterion, Patients 13, 14, 17, 19, 20 were the test subjects for the present study.

11.2.2 Volume Conductor Models

In contrast to [35] that used homogeneous BEM model for calculations, following inhomogeneous regions were added to the patients' volume conductor models: ventricular blood masses, lungs and liver. These surface contours consisted in average (among patients) of 1.600, 2.000, 450, 500 and 350 nodes, respectively. Blood meshes comprised only ventricular blood masses and did not include the atrial part (similar to [35]). Furthermore, the torso surfaces were adjusted for better match to the localized electrode positions [175]. Electrical conductivity values for the included inhomogeneity regions were assigned as follows: heart and torso with 0.2 S/m, lungs with 0.04 S/m, blood with 0.6 S/m [74].

11.2.3 Inverse Calculations

For the inverse reconstructions, two spatio-temporal methods were considered: the fastest route algorithm (FRA) for calculating the correlation maps and the Tikhonov-like approach imposing nondecreasing constraints on the TMP time course. In the used FRA implementation, conduction velocities in tangential and transmural directions relative to the heart surface were set to 1 and 0.4 mm/ms, respectively. For effective pacings, the QRS complex onset was assigned to the time instance featuring the smallest BSPM signal energy among those occurring after the pacing artefact. For the constrained optimization algorithm, the problem was solved for each 8th time instance of the QRS complex. The time sampling was set in the same way as for the simulation study described in Chapter 10. Optimal regularization parameter was chosen according to the L-curve criterion [103]. Subsequently, activation times were derived from the calculated TMV based on the spatio-temporal method proposed by Erem *et al.* [45].

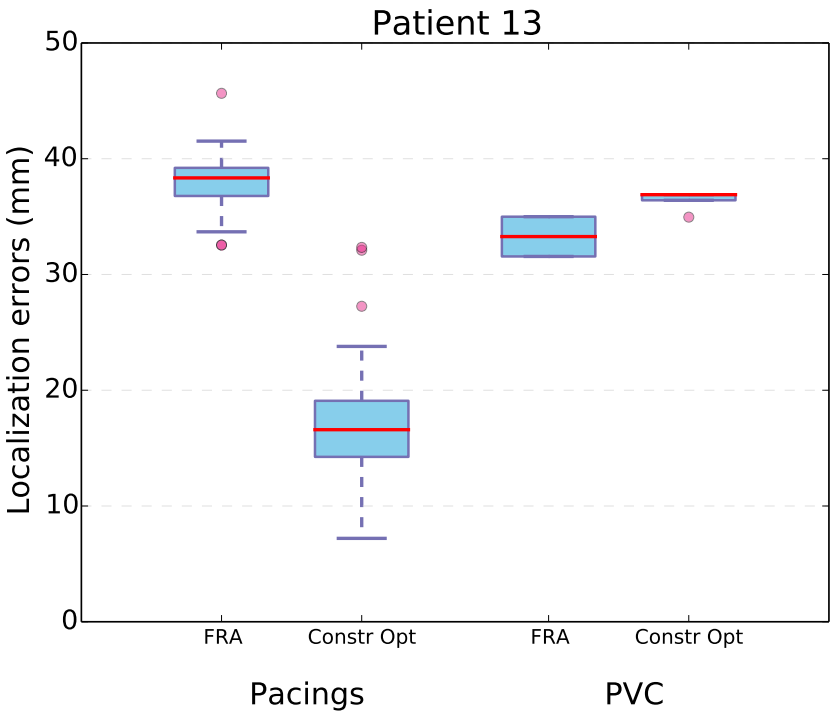

Figure 11.1: *Patient 13:* Localization errors for the considered regularization methods.

11.2.4 Evaluation of Results

As demonstrated in [35], the pacing sites and points of the latest ablation localized by the CARTO system often did not conform with the heart surface. This could be due to several reasons. First, because of unavoidable co-registration errors between multiple imaging modalities. As a consequence, this uncertainty also contributed to the estimation of ECG imaging errors. Second, catheter could have possibly been placed on the papillar muscles that were not included into the geometrical model. Based on these considerations, the validation points provided by the CARTO system were first projected onto the heart surface. Subsequently, localization errors were computed as distances between the projected points and the noninvasively found origins.

11.3 Results

11.3.1 Patient 13

An overview of the noninvasively obtained results is provided by Fig. 11.1. The inverse problem was solved for 24 paced activation sequences originating from five different sites and four PVC beats. The PVC could be successfully terminated and the point of latest ablation was taken as validation reference. Pacing sites as well as the PVC origin were situated on the right ventricular septal wall.

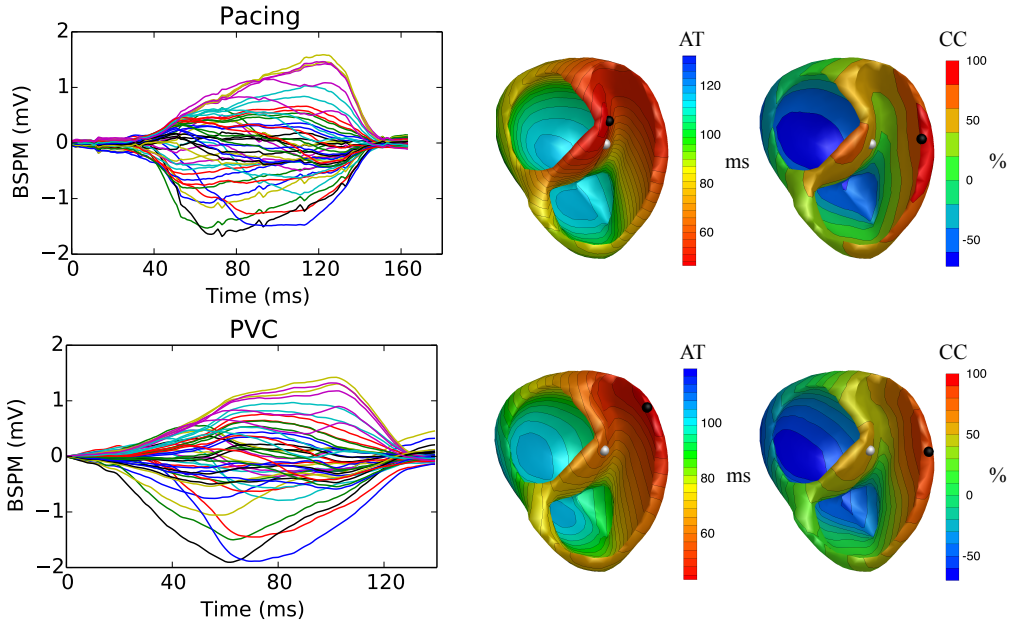

Figure 11.2: *Patient 13:* Exemplary performance of considered regularization methods. Left: BSPM signals resulting from a pacing activation sequence and PVC beat; middle: corresponded activation times reconstructed with the constrained optimization algorithm; right: FRA-based correlation coefficients maps. White spheres correspond to reference CARTO points projected onto the cardiac mesh, black spheres indicate excitation origins localized by the noninvasive imaging.

Although constrained optimization method resulted in significantly higher localization accuracy of pacing sites compared to the FRA-based approach, the difference in PVC beats imaging was marginal with slightly superior performance of the full-search. Exemplary reconstruction results for a pacing sequence and PVC beat along with the corresponding BSPM are visualized in Fig. 11.2. Performance of the FRA-based approach was consistent for all ectopic activations. Points providing the highest correlation with the measured BSPM were localized on the endocardial part of anterior basal RV wall. Regions covering the true excitation origin also exhibited an island of high similarity, though with smaller correlation.

In contrast, the optimization routine resulted in higher reconstruction quality for paced activation sites. Origins were correctly identified to lie on the septal wall (see Fig. 11.2) and imaging errors were 18.6 mm in average. For PVC cases however, the reconstruction quality was poorer and imaged sites were localized either on the RV wall or in septal region adjacent to the RV.

11.3.2 Patient 14

Within this dataset, the noninvasive imaging was applied to 15 paced and 16 PVC beats. The ablation procedure was the follow-up of a previous successful therapy with PVC situated in the LV under aortic valve. Due to proximity of the ablation target to the atrioventricular node, the procedure was cancelled and the reference origin was defined as the point of earliest activation recorded by the CARTO system. Ectopic origin as well as pacing sites were

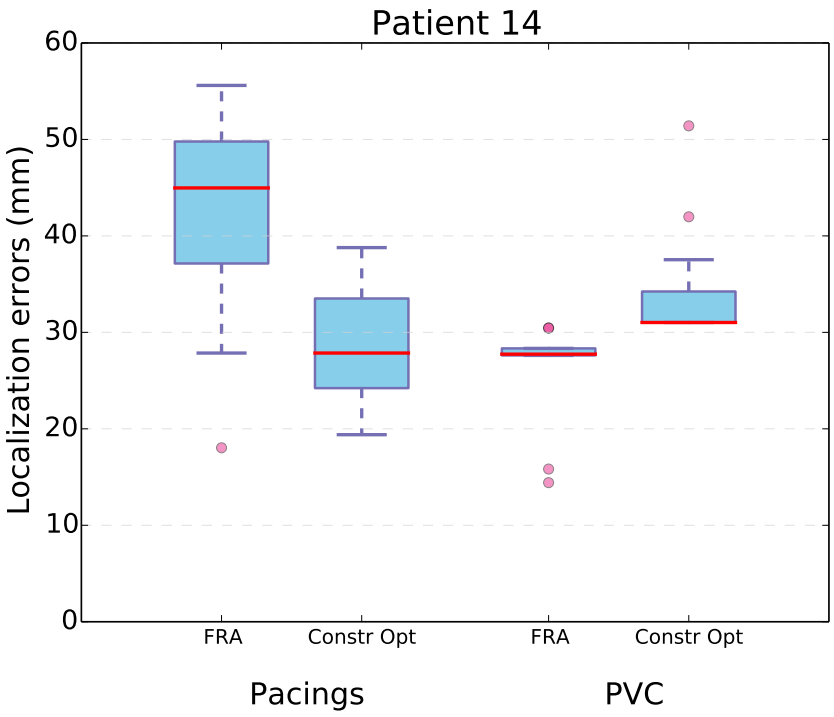

Figure 11.3: *Patient 14:* Localization errors for the considered regularization methods.

situated on the RV septal wall. Localization errors calculated from the inverse solutions are shown in Fig. 11.3.

Compared to the FRA-based approach, Tikhonov-like minimization resulted in superior performance for imaging of pacing sequences and slightly higher localization errors for PVC detection. Exemplary reconstruction results are shown in Fig. 11.4. In pacing reconstructions, the full-search localized early excitation sites to lie on the RV anterior wall in all but two cases. The correctly identified beats resulted in errors of 18 and 27.8 mm. All PVC beats were, however, correctly localized to originate from the RV septal wall, which is also reflected in reduced error distances (see Fig. 11.3). The best PVC imaging results were obtained with FRA and corresponded to 14.2 and 15.8 mm errors.

Constrained optimization scheme succeeded to detect an excitation origin in the septum in 27 out of 31 ectopic beats, when both pacings and PVC sequences are taken into account. In contrast to Patient 13, localization accuracy of extrasystoles was consistent with imaging results for pacing sites.

11.3.3 Patient 17

For Patient 17, 12 paced activation sequences and six ventricular extrasystoles were non-invasively imaged. Overall performance of the applied inverse strategies is represented by

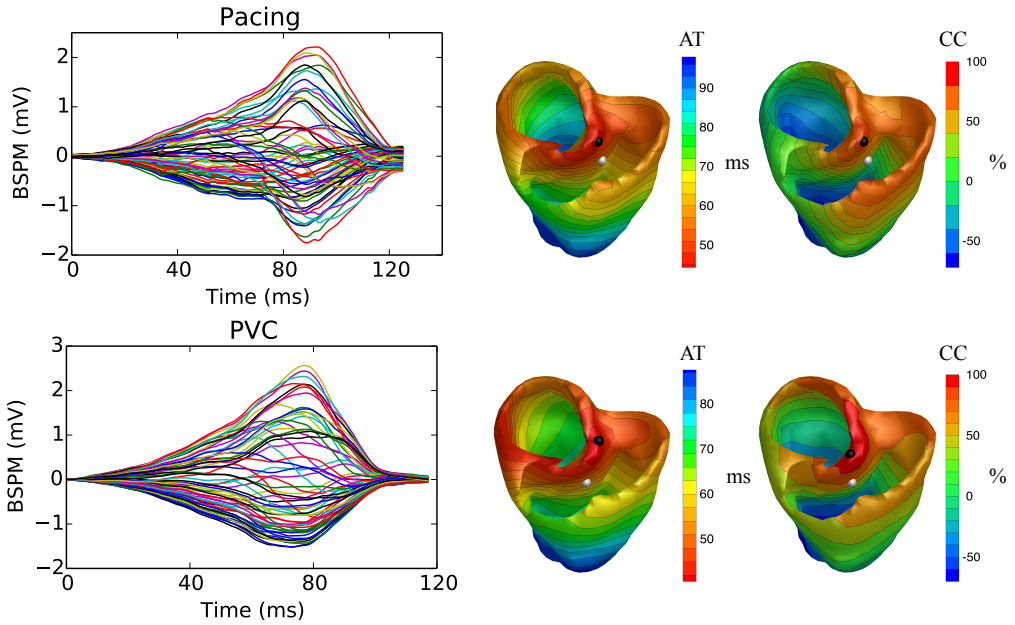

Figure 11.4: *Patient 14:* Exemplary performance of considered regularization methods. Left: BSPM signals resulting from a pacing activation sequence and PVC beat; middle: corresponded activation times reconstructed with the constrained optimization algorithm; right: FRA-based correlation coefficients maps. White spheres correspond to reference CARTO points projected onto the cardiac mesh, black spheres indicate excitation origins localized by the noninvasive imaging.

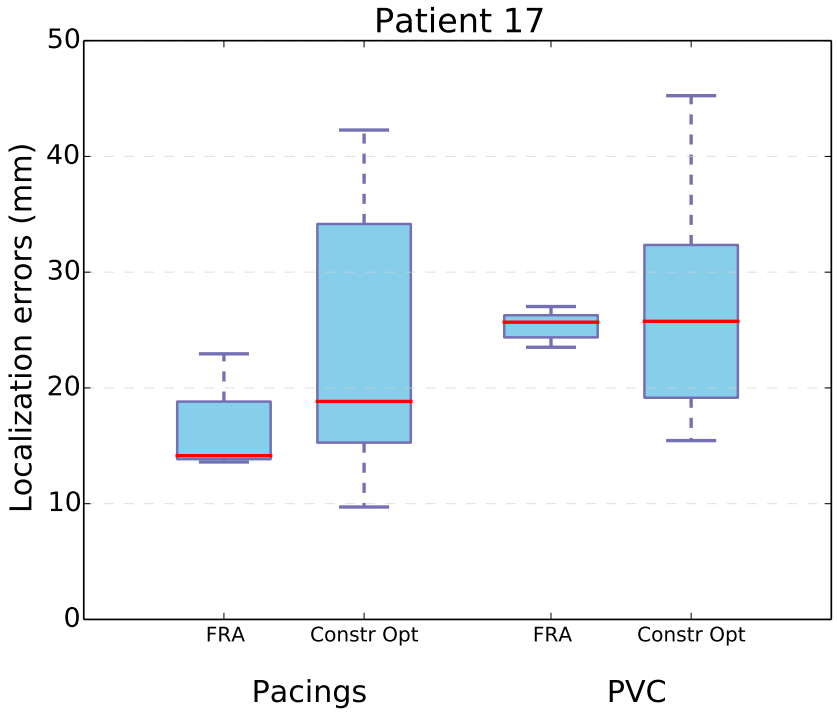

Figure 11.5: *Patient 17:* Localization errors for the considered regularization methods.

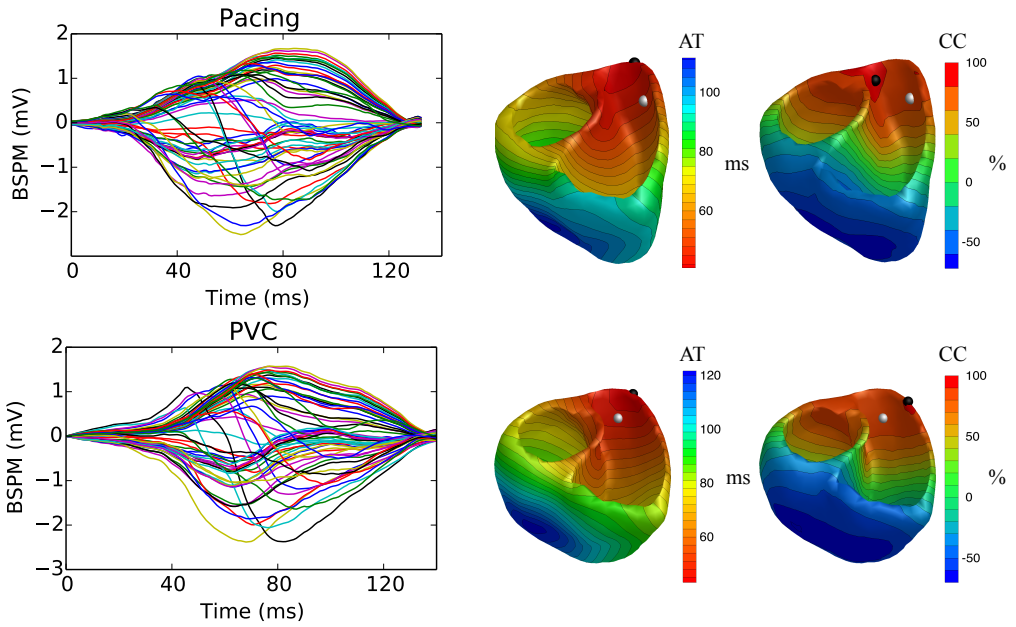

Figure 11.6: *Patient 17:* Exemplary performance of considered regularization methods. Left: BSPM signals resulting from a pacing activation sequence and PVC beat; middle: corresponded activation times reconstructed with the constrained optimization algorithm; right: FRA-based correlation coefficients maps. White spheres correspond to reference CARTO points projected onto the cardiac mesh, black spheres indicate excitation origins localized by the noninvasive imaging.

Fig. 11.5. PVC were situated in the RV outflow tract (RVOT) and could be successfully terminated by a catheter ablation.

For this patient, FRA-based method exhibited superior performance in imaging of ventricular ectopic activities. Box plots of localization errors for pacings as well as for PVC showed considerably smaller variation compared to the optimization approach. Some reconstruction results are visualized in Fig. 11.6. In all experiments, validation reference points were found within the areas of highest correlations in the FRA-calculated CC-maps. With regard to activation times computed from the outcome of constrained optimization algorithm, several beats resulted in an early activation originating from the septal wall, which is reflected in broader spread of localization errors in Fig. 11.5.

11.3.4 Patient 19

For Patient 19, BSPM recordings for 27 activation sequences including four PVC beats were available for inverse reconstructions. The ablation performed in basal posterior septal part of the LV terminated the arrhythmia and was assigned as the validation reference. Pacings stimuli were applied to the septal and posterior parts of the LV. Localization errors of the noninvasive electrocardiographic imaging for all considered activation sequences are provided by Fig. 11.7.

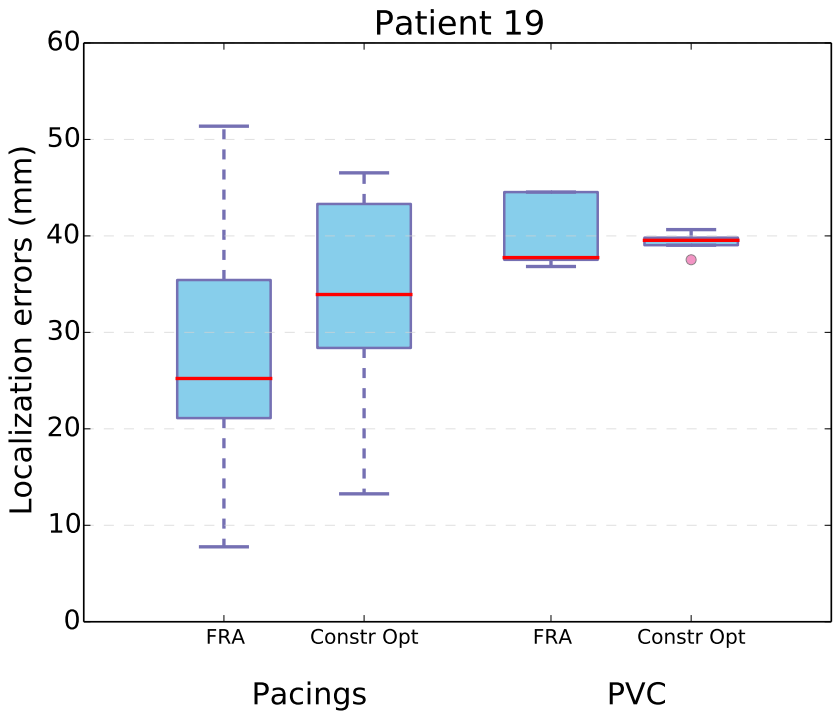

Figure 11.7: *Patient 19:* Localization errors for the considered regularization methods.

Some reconstruction examples are visualized in Fig. 11.8. For pacing sites on the septal wall and PVC beats, the majority of the FRA-found origins were situated on the LV posterior wall. In some cases, points delivering the closest BSPM similarity were wrongly misclassified to originate from the RV. It was observed that BSPM from different pacings led to very similar CC-maps (see Fig. 11.8) and that the areas with high CC values often spread over the whole posterior part of both ventricular chambers. Performance of the constrained optimization algorithm was consistent for both pacings and PVC cases, which is expressed by narrow errors spread in the corresponding box plots in Fig. 11.7. Noninvasively imaged excitation origins were found predominantly epicardially on the posterolateral LV wall.

11.3.5 Patient 20

Patient 20 featured the largest number of available experiments: 29 BSPM recordings resulting from pacing stimuli together with nine PVC beats were noninvasively imaged. PVC could be terminated by an ablation in LVOT close to the mitral valve. For this patient, best reconstruction quality among the reported subjects was achieved. Localization errors computed from the inverse solutions are provided by Fig. 11.9.

Exemplary reconstructions from both regularization methods are shown in Fig. 11.10. FRA-based technique exhibited superior localization accuracy for pacing sites as well as for PVC sequences. Although the corresponding box plots reveal some variation in the distance errors, almost for all cases ectopic origins were successfully characterized by maxima regions

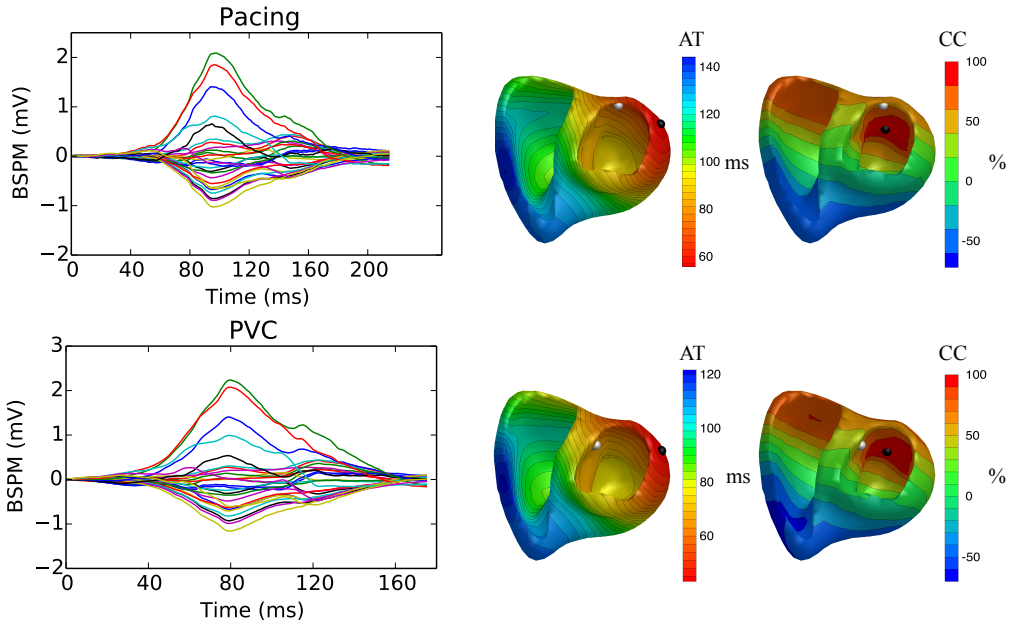

Figure 11.8: *Patient 19:* Exemplary performance of considered regularization methods. Left: BSPM signals resulting from a pacing activation sequence and PVC beat; middle: corresponded activation times reconstructed with the constrained optimization algorithm; right: FRA-based correlation coefficients maps. White spheres correspond to reference CARTO points projected onto the cardiac mesh, black spheres indicate excitation origins localized by the noninvasive imaging.

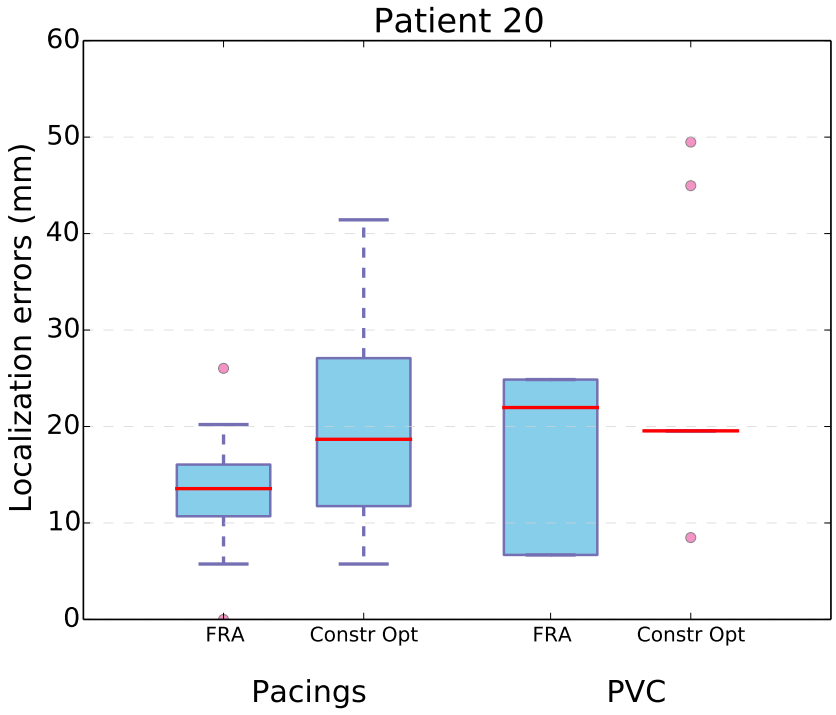

Figure 11.9: *Patient 20:* Localization errors for the considered regularization methods.

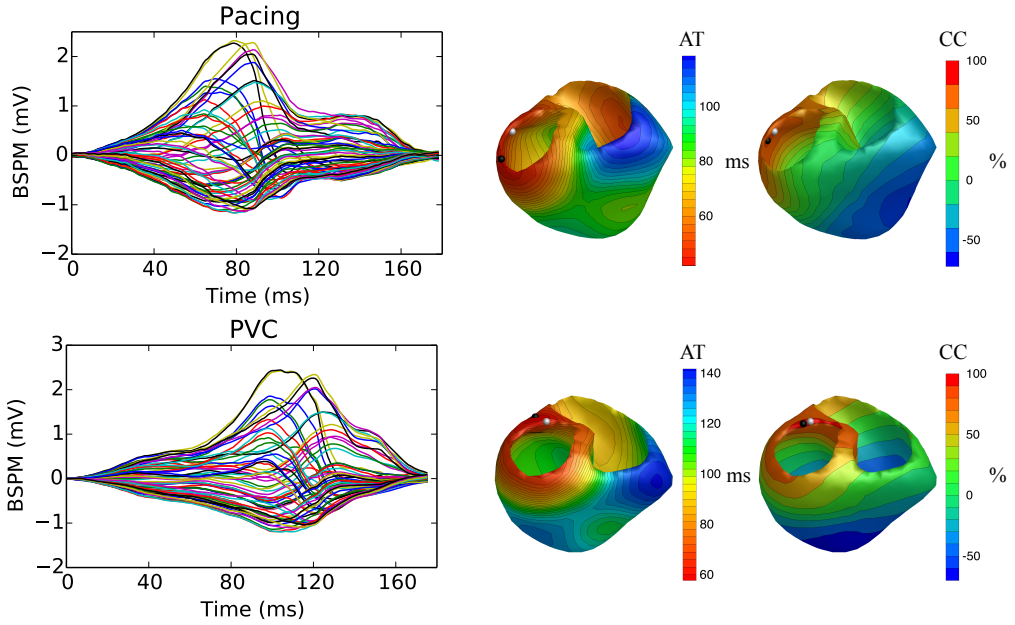

Figure 11.10: *Patient 20:* Exemplary performance of considered regularization methods. Left: BSPM signals resulting from a pacing activation sequence and PVC beat; middle: corresponded activation times reconstructed with the constrained optimization algorithm; right: FRA-based correlation coefficients maps. White spheres correspond to reference CARTO points projected onto the cardiac mesh, black spheres indicate excitation origins localized by the noninvasive imaging.

in the CC-maps. The optimization approach, though catching well the region of interest, often resulted in somewhat over-smoothed areas of early activation. This observation is rendered by larger spread of localization errors compared to FRA performance.

11.4 Discussion

In the present work, performance of two spatio-temporal regularization techniques was evaluated in clinical context. The inverse problem of ECG was solved for ventricular pacings and ectopic beats. To create validation reference for PVC locations in case of successful therapy, the point of latest ablation was adopted. For Patient 14, the procedure was canceled due to a risk of damaging AV node and the point with earliest activation from the CARTO local AT (LAT) map was used as gold standard.

The data pre-processing and co-registration of imaging modalities as well as the first noninvasive imaging results for these datasets were performed by W. Schulze within the scope of his PhD [35]. In contrast to this work, the inverse problem had been solved with several established spatio-temporal methods including Tikhonov-Greensite [176], critical point theorem [177], time integral method [151, 156], maximum-a-posteriori (MAP) [87, 178] and an isotropic variant of the FRA-based correlation method. The conduction velocities (CV) in myocardium had been assumed to be isotropic and equal in all directions, which does not reflect the reality. Furthermore, instead of normalizing the QRS complexes duration between

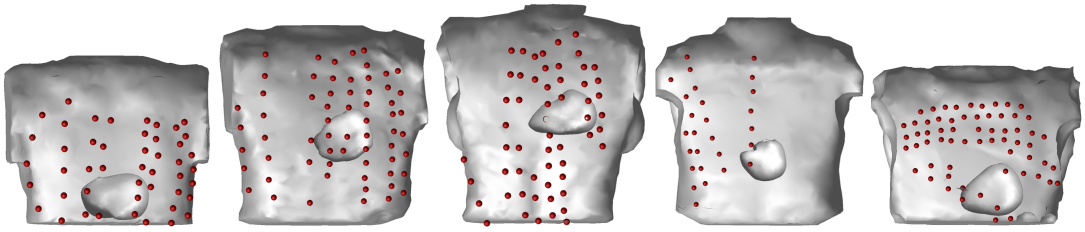

(a) Patient 13 **(b)** Patient 14 **(c)** Patient 17 **(d)** Patient 19 **(e)** Patient 20

Figure 11.11: Patients torso models with electrodes used for ECG imaging. Lungs, intracavitary blood and liver are not displayed in order to better represent spatial relation between heart and lead locations.

simulated and measured signals, the R-peaks had been aligned first. Then, the similarity between signals restricted by two time points exhibiting 15% of the R peak magnitude and corresponding to onset and end of the QRS complexes had been calculated. In the present study, anisotropic cardiac nature was somewhat taken into account by setting propagation velocity in the direction tangential to the heart surface to be two times higher than through the myocardial wall. Moreover, it might happen that the signal morphology within the first 15% can be crucial for detecting the correct side of a ventricle (endo-/epicardial wall) or septum (left/right septal wall). Based on these considerations, a 'classic' FRA implementation that involves scaling of CV was employed. The reconstructions were performed with BEM for inhomogeneous volume conductor models, whereas isotropic BEM and inhomogeneous FEM models had been used in [35]. Note that for the FEM models, the 'simplified' FRA-based full-search had resulted in the best localization accuracy [35]. In combination with BEM, the MAP method had been reported to deliver the best results.

For this study, no averaging of multiple beats corresponding to the same event was performed. In [35], beats averaging for noninvasive imaging with MAP was reported to partially worsen the results. Within the present work, BSPM corresponding to the error outliers were visually inspected. Often, these signals featured morphology and QRS duration quite distinct from the cases that provided reasonable localization accuracy. This might be due to baseline wander effects or catheter tip movements. In [179], the question of better leveraging available repeated recordings was addressed by comparing several approaches. The authors applied a 'standard' averaging, a nonlinear spline based averaging method [46, 180, 181] and a statistical approach for incorporating a data-driven noise model into the inverse procedure [179]. No definite conclusions could be made about overall performance of the considered methods, which suggests necessity of further investigations on an optimized use of multiple recordings.

Furthermore, sensitivity of the inverse results, especially for the correlation-based approach, might heavily depend on the number and position of ECG leads. Due to clinical restrictions in the present study, electrodes could be placed only on the anterior torso part. An overview of the electrodes configurations for the considered patients is provided by Fig. 11.11. Although an 80-channel BSPM system from BioSemi was employed [182], some channels must have been dismissed due to bad contact and, consequently, low signal quality.

For Patient 19, the remained 27 electrodes are situated on the right side of anterior chest wall, which might explain poor performance of the model-based FRA approach. On the other hand, it points out that Tikhonov regularization is more robust with respect to limited number of leads. Although there is no gold standard on an optimal electrodes setting required to cover all possible ambiguities in the source imaging, commercial systems utilize chests with over 250 channels placed on both posterior and anterior surfaces of the torso [8, 171].

For this work, two algorithms representing data-driven (Tikhonov) and model-based (FRA) approaches were tested. Achieved localization errors were rather dependent on the patient data quality and not on underlying regularization scheme. Both considered methods were revealed to have some limitations. With this regard, further attempts to improve localization accuracy of the existing approaches should be undertaken. When the constrained optimization algorithm is concerned, activation times are derived from the inversely calculated TMV. It was often observed that resulting AT maps featured over-smoothed areas of early activation with very similar values. These regions could be considered analogous to the FRA-based CC-maps that provide the best guess as well as some uncertainty area. Therefore, a more robust method incorporating some propagation dynamics for reliable estimation of earliest excitation site from imaged potentials is needed. A simple alternative can be to take the whole early activation regions and assume its center of mass to be sought solution.

The FRA-calculated correlation coefficients were visualized for better representation of possible solution uncertainties. In a classical implementation, the best FRA-estimated activation sequence is used as initialization for nonlinear optimization of AT [30, 39]. Although subsequent optimization would probably not solve the outliers problem, one should investigate on the spread of final localization errors for cases of multiple pacing stimuli being FRA-estimated to come from the same heart area. In order to correctly localize septal events wrongly classified to have RV or LV origin (see Patients 13, 19), one might need to perform nonlinear optimization for the first as well as for the second and third best estimates obtained by FRA.

Finally, both methods should be combined while retaining the best regularization features of each part. One could think of a MAP-similar approach with the basis generated by realistic FRA activation sequences and subsequent spatio-temporal constrained optimization. Another alternative could be to combine the outputs of two methods. The activation times estimated from constrained optimization could be fed into the nonlinear optimization for an improved localization of early excitation site. On the other hand, the best FRA-calculated activation sequences can be converted into TMV distributions and serve as an initial guess for a spatio-temporal Twomey regularization [183, 184] of the TMV-based problem.

CHAPTER 12

ECG Imaging for Localization of Scar-Related PVC: *in silico* Study

In Chapter 10, performance of two state-of-the-art spatio-temporal ECGI techniques was investigated for the case of a structurally normal heart. Results demonstrated ability of the considered methods to accurately localize PVC origins and classify foci with respect to their origin endo- or epicardial nature. Herewith, the study is extended to the case of a scar affected heart. Ten ectopic activation sequences originating from varying distances relative the introduced scar were simulated with monodomain model. Inverse solutions were computed, as previously, with FRA-based correlation search and an algorithm imposing nondecreasing temporal constrains on the sought TMP.

12.1 Introduction

One of possible clinical applications for the noninvasive EGG imaging is PVC localization. Ectopic beats represent an organized excitation spread starting from one focus, which allows imposition of strong spatio-temporal constraints biasing the solution toward desired behavior. The previously described FRA-based search simulates realistic activation sequences and compares the resulting BSPM to measured signals based on the correlation criterion. Another spatio-temporal algorithm considered in this work minimizes the misfit between recorded and predicted signals while forcing the TMV to be increasing functions in the temporal domain.

In a structurally healthy heart, these methods are probably the best representatives of model-based and data-driven inverse approaches, respectively. However, their underlying assumption are violated in presence of scar tissue (necrotic, or old infarct). Border zones surrounding the scar and possessing ischemic properties have been shown to correlate with inducibility of ventricular tachycardia (VT) [185]. In these cases, scar-related reentrant VT is conjectured to be triggered by an ectopic excitation originating from the border zone close to the infarct region.

Concerning the forward modeling of VT, the first reports on the role of fibrosis and gray zone in its inducibility and maintenance have appeared recently [186–189]. With regard to the noninvasive imaging of reentrant VT, the first studies were performed by Burnes *et al.* in animal open chest procedures [89, 190]; these investigations were followed by further animal and human studies (see e.g. [152, 154, 173, 174, 191–193]). In [173], ECG imaging of epicardial potentials was performed for 79 catheter pacings and induced VT. Interestingly, for considered epicardial pacings, the localization accuracy of 13 ± 9 mm over normal myocardium was significantly worsened to 28 ± 27 mm when pacings were performed close to scar.

Furthermore, the basis assumptions behind the surface TMP model are violated in presence of scar. Equivalence of volumetric sources and surface TMP was shown for the case of continuous resting potentials in [157]. In a case of injury, the boundaries of scar or ischemia, must be, however, also explicitly considered. Note that only few simulation studies of necrotic and scar tissue effects on the performance of TMP-based ECG imaging was reported [194, 195]. In [195], necrotic tissue was characterized by reduced action potential amplitude without adaptation of any propagation parameters [195]. For initializing the nonlinear activation times solver, the critical point method [177] and linear time-integral methods [156] were used. The latter resulted in carving out the affected tissue, which could serve as an indicator for ischemia affected area.

In [194] it was shown that presence of an old, extensive myocardial infarction can considerably bias results of the uniform double layer source model and that proper inclusion of a scar into the geometrical model could improve the imaging results.

The goal of the present work is to simulate scar in a realistic manner and evaluate performance of the two state-of-the-art spatio-temporal approaches in PVC localization using the surface TMP source model, when no additional assumptions on the scar affected tissue are made.

12.2 Methods

12.2.1 Simulation Setup

For the present study, an extensive scar region caused by left anterior descending coronary artery stenosis was introduced into the geometrical heart model that is described in detail in Chapter 8. The scar was modeled as a passive tissue with decrease of the electrical conductivity by a factor of 10 compared to the value of healthy heart [93].

For the excitation propagation simulation on the scar affected ('reduced') geometry, the setup from Chapter 8 was adopted. In total, 10 ectopic beats originating from endo- and epicardial sites close and far from the scar were simulated. In Fig. 12.1, the resulting activation patterns are shown on the considered ventricular mesh. The scar area is depicted in dark blue.

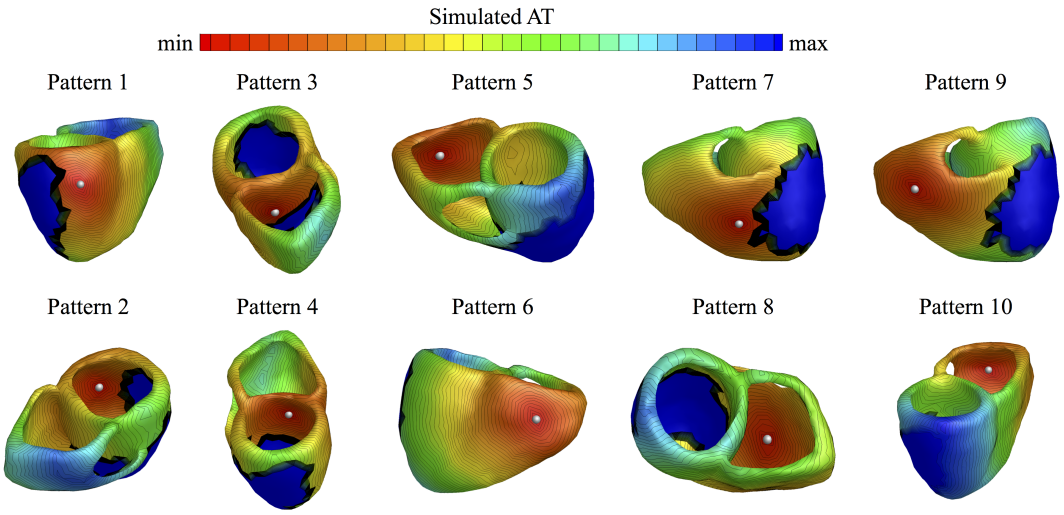

Figure 12.1: Simulated activation sequences: The excitation origin is marked by a white sphere; the scar region is visualized in dark blue. Ectopic beats are simulated pair-wise with respect to their endo-epicardial origin; furthermore, the dependence of localization results on the distance from PVC origins to the scar was investigated.

The BSPM were calculated for the realistic case of unequal anisotropy ratios between the conductivities in longitudinal and transmural directions in the intra- and extracellular spaces. These ratios were assigned to three and nine, respectively. For the inverse computations, the BSPM signals were contaminated with white Gaussian noise of 30 dB.

12.2.2 Inverse Calculations

The surface transmembrane potentials source model was used for the inverse calculations. The scar was not accounted for and all computations were made for the complete heart geometry under the assumptions of healthy myocardium. The inverse problem was solved with the FRA-based full-search and with the spatio-temporal constrained optimization algorithm.

12.3 Results

The accuracy of the considered scar-related PVC localization for both inverse algorithms is represented by Fig. 12.2. Table 12.1 provides an overview of the localization errors in dependence on the PVC location with respect to the scar.

12.3.1 FRA-based Reconstructions

FRA-based correlation maps reflecting possible solution uncertainties are depicted in Fig. 12.3. White spheres represent the true excitation origin, black spheres mark the point delivering

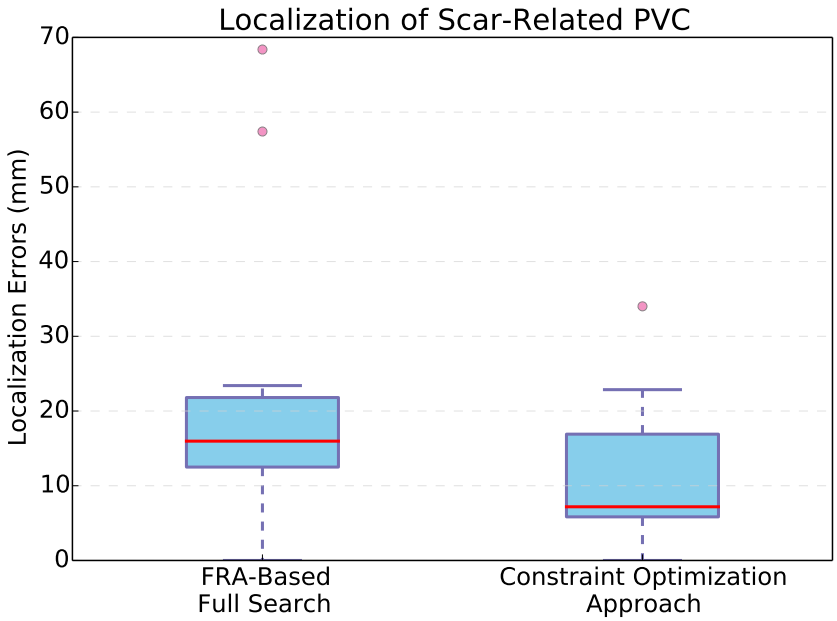

Figure 12.2: Localization errors for the considered FRA-based full search and the optimization approach imposing nondecreasing temporal constraints on the sought TMV.

Table 12.1: Localization errors for the simulated ectopic foci. Geodesic curves along the edges of triangulated heart surface were used for calculation of distances from PVC locations to the scar.

Pattern #	Anatomical Location	Distance to scar	Localization error, mm	
			FRA	Constrained Optimization
1	LV lateral, epi	19.3	17.0	0
2	LV lateral, endo	21.0	11.6	10.3
3	RV septal	15.1	68.4	34.0
4	LV septal	26.4	57.4	19.1
5	RV posterior, endo	60.3	15.3	7.4
6	RV posterior, epi	59.0	15.0	22.9
7	RV anterior, epi	15.0	16.6	5.6
8	RV anterior, endo	25.1	23.4	5.2
9	RV lateral, epi	54.9	0	6.6
10	RV lateral, endo	57.0	7.0	7.0

highest CC between the reference and FRA-simulated ECG. For each simulation, the correlation provided by the best solution estimate is indicated. The mean localization error was 23.2 ± 22 mm. For the patterns 3 and 4 corresponding to the septal ectopic beat (second column in Fig. 12.3), the errors were 68.4 and 57.4 mm, respectively. For these PVC, the origins were incorrectly localized to be situated on the LV epicardial lateral wall. For the rest eight patterns, the average error was 13.2 ± 7.1 mm which is in accordance with the results

from Chapter 10. Excitation origin 9 (upper row, most right plot in Fig. 12.3) was localized exactly. Patterns 6, 8 and 10 (lower row, figure from the middle to the right) endocardial sites of the earliest activation were wrongly classified to lie on the epicardial part of the heart surface; for the patterns 6 and 10, the simulated origin was within the region of the highest correlation.

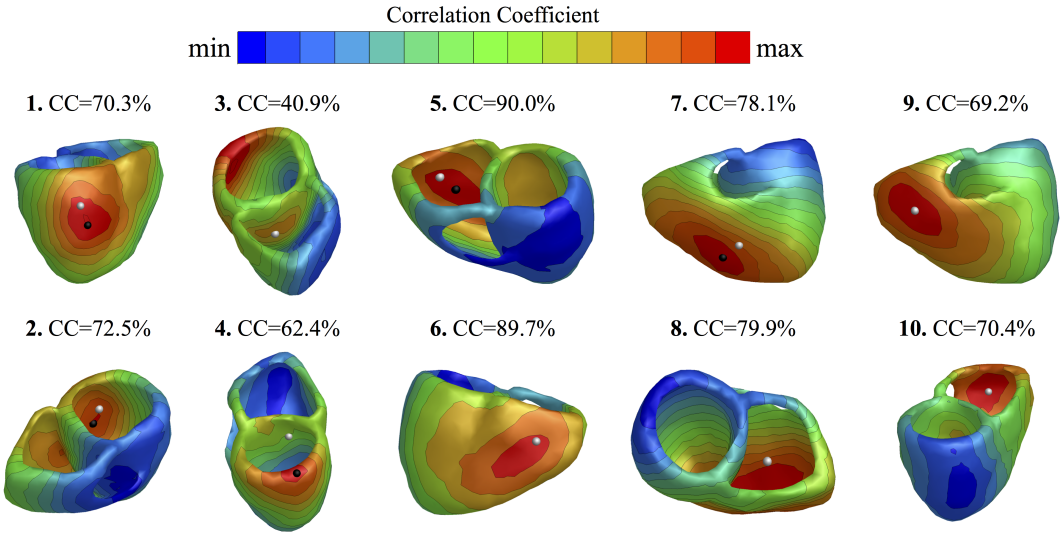

Figure 12.3: Correlation maps obtained with the FRA-based full search: white spheres mark the true excitation origin; black spheres indicate the found origin. For each simulated pattern, the correlation coefficient between the best test activation sequence generated by FRA (starting from the black point) and the simulated ECG is shown. For pattern 2, the localized origin is situated on the LV epicardial lateral wall. For patters 6, 8 and 10, the localized origin is situated on the epicardial wall and is, therefore, not visible on the figure. For pattern 9, perfect localization was achieved.

12.3.2 Performance of constrained optimization Algorithm

The activation times maps derived from the calculated TMV are visualized in Fig. 12.4. The average localization error was 11.8 ± 10.3 mm. For patterns 3 and 4 corresponding to the PVC starting from RV and LV septal sides respectively, a septal origin was identified: however, the LV focus was localized on the septal wall and the RV point of earliest activation was detected on the LV septal side. Pattern 1 resulted in perfect reconstruction. For patterns 5, 8 and 10, the true endocardial origin was found misclassified to be situated on the epicardium. The early activation regions corresponded well to the true excitation origin. In the area affected by scar, no corresponding noticeable indicators in the activation times maps were observed.

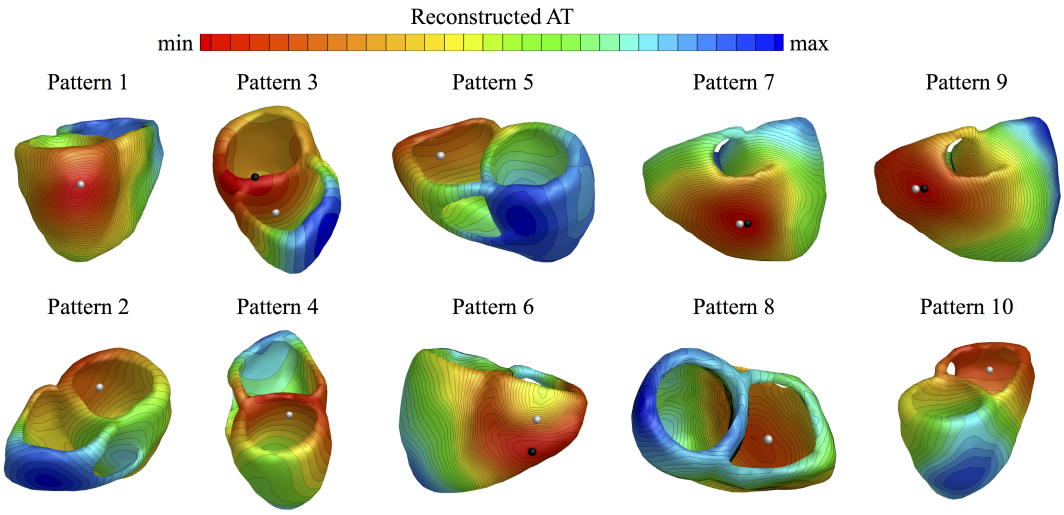

Figure 12.4: Activation times reconstructed with the constrained optimization approach: white spheres mark the true excitation origin; black spheres indicate the found origin. For pattern 1, perfect localization was achieved. For patters 4 and 6, 8, 10, the localized origins are situated on the other septal side and epicardial wall respectively and are, therefore, not visible on the figure.

12.4 Discussion

In the present study, performance of two spatio-temporal techniques was evaluated for localization of scar-related PVCs. The scar was simulated as passive tissue and, therefore, not involved in the excitation propagation. Ectopic beats were simulated to originate from varying distances relative to the scar. In the inverse calculations, the transfer matrix was, however, calculated based on the surface TMP source model without taking this information into account: the heart was assumed to be structurally normal without discontinuities in the resting potentials profile. The obtained inverse reconstructions were consistent for both inverse methods: the areas of early activation were identified with both methods; excitation patterns starting from septum close to the scar resulted in the lowest correlation for the FRA approach and highest localization errors for the constrained optimization algorithm.

With regard to the simulation setup used in the present work, excluding scar area from the forward calculations geometry and assuming healthy heart tissue in the inverse procedure gives rise to an additional model error, when the inversely estimated wavefront passes the necrotic region. Obviously, the effect of this error on the inverse reconstructions depends on the size of infarct zone and its position relative to the PVC origin. Intuitively, when an ectopic beat starts remotely from the scar, discontinuous propagation affects only the end of the depolarization phase. In the present work, corresponding patterns 5 and 6 resulted in the highest correlation between reference and FRA-estimated BSPM (90 and 89% respectively). For the considered Tikhonov-like optimization method, imposed temporal constraints in combination with Laplacian regularization operator guarded the solution smoothness by assigning late activation times to the scar-related points. In a case of PVC starting close to the scar, the biggest modeling errors are present in the time span when the simulated wavefront is passing the scar region. Surprisingly, the correlation criterion turned out to

be a robust feature for identifying such excitation origins. The exceptions were the septal extrasystoles starting from immediate vicinity of the scar; these patterns resulted in largest localization errors for the norm-based optimization approach as well.

It can be assumed that ECG imaging for a cardiac geometry that explicitly takes into account scar information would result in accuracy comparable to those reported in Chapter 10 [194]. In this study, both inverse algorithms were not able to provide any information on the scar location. However, a low correlation coefficient, as for pattern 3, could indicate presence of model errors and elaborate on results reliability. In such cases, tailored inverse routines for scar localization might be applied first in order to estimate infarction size and position [34, 95]. Thereafter, PVC localization could be performed with the proposed methods for an adjusted cardiac geometry.

12.5 Limitations

Despite promising results, no strong claims can be made about the localization accuracy of scar-related PVC in general: in further simulation scenarios, different scar configurations (size, transmural, endo-/epicardial extent, shape) in combination with varying ectopic origin locations should be considered.

Moreover, the employed scar model represents rather a limit test case, when the scar region consists exclusively of non-excitable tissue; in reality, ventricular scars consist not only of dense fibrosis with collagen and fibrocytes, but also contain areas with survived myocyte bundles [196, 197]. The fibrosis contributes to the slow conduction in scar regions and could create conduction blocks thus forcing the excitation to take a circuitous path through the critical isthmus. In many cases, treatment of the patients suffering from VT is further complicated by the fact that scars can contain multiple circuit paths contributing to a reentry.

Therefore, in future work a more realistic VT-facilitating scar model with slow conducting fibrosis in presence of reentry triggering isthmi should be included into the excitation propagation model [187, 189].

CHAPTER 13

Clinical Study on ECG Imaging of VT

In the present study, ECG imaging is applied to a case of monomorphic ventricular tachycardia (VT). For reconstruction, a constrained optimization algorithm was tested. The reconstructed activation times (AT) are qualitatively compared against endocardially recorded signals.

13.1 Introduction

ECG imaging is an evolving technology for noninvasive assessment of cardiac electrophysiological conditions. In the present study, imaging of transmembrane potentials (TMP) and associated activation times is performed for a case of monomorphic ventricular tachycardia (VT).

Although several validation studies of VT imaging were performed in animal experiments [89, 152, 174, 190], validation in human is challenging and limited by certain clinical restrictions, e.g. radiation dose of the CT imaging modality, applicability of an electrodes vest during the EP procedure, acquisition and processing of the validation data. In [89, 190], validation of epicardial potentials was realized with a 490 electrode sock during an open chest-procedure. Noninvasive reconstruction of electrograms and isochrones was able to reveal the location of abnormal heart substrate, epicardial activation sequences and epicardial breakthroughs. In [152, 174], three-dimensional cardiac electrical imaging was assessed for intramural pacing rhythms and norepinephrine induced VT of focal origin in rabbit and canine hearts, respectively. BSPM and intracardial electrograms were simultaneously measured in closed-chest conditions. For paced and focal activities, points of earliest excitation were localized with accuracy of 5 and 7 mm respectively.

The first clinical human case of noninvasive imaging for VT was reported in [191]. A young athlete suffering from asymptomatic PVCs developed a sustained left ventricular tachycardia during physical exercise. For this patient, epicardial activation map for a single PVC was noninvasively computed. CARTO maps obtained during RFA endocardially overlapped with the area indicated by ECG imaging as epicardial excitation point.

A more comprehensive study of ECGI performance for endocardial electroanatomical mapping of ventricular arrhythmia is described in [192]. Noninvasive reconstruction of epicardial potentials was accomplished for 25 patients undergoing catheter ablation procedure for various types of symptomatic VT or PVC. For 18 patients demonstrating spontaneous abnormal ventricular rhythms, ECG imaging was performed before the invasive catheter-based electrophysiology studies. Nine patients were imaged during sustained VT, five patients had a reentrant mechanism characterized by rotational wave and successful entrainment of the tachycardia with stable return cycle after termination of pacing. In all reentrant patients, VT activation patterns reconstructed on the epicardium showed a good correspondence with the endocardial electroanatomical maps. Furthermore, the imaged activation times matched well to the ventricular scar areas. Despite the good qualitative correspondence, no quantitative analysis on the localization accuracy of the VT exit points was performed. Besides, the earliest epicardial breakthrough may not necessarily identify the endocardial circuit, which remains a limitation of the study.

In [173], ECG imaging was applied to two patients during implantable defibrillator pacing, catheter pacing and induced VT. Ventricular activation sequences determined by inverse solutions and epicardial three-dimensional contact mapping qualitatively yielded similar patterns, including areas of slow conduction or functional block which resulted in inversely computed crowded isochronal lines. For induced VT cases, noninvasive imaging successfully co-localized epicardial breakthroughs with the site of successful ablation in two out of six VTs. The exact activation sequence during VT was not mapped due to hemodynamic instability or clinical expediency. Therefore, the location of VT exit points were rather inferred and not precisely located [173].

In this work, qualitative analysis for noninvasive localization of imaged and recorded activation patterns is performed. For the considered case, the first noninvasive imaging results with Tikhonov-Greensite method [198] are described by W. Schulze in his PhD thesis [35]. Compared to the previously performed analysis, the present work assumes another numerical method of field calculations (BEM instead of FEM) and is extended by considering another spatio-temporal regularization algorithm.

13.2 Methods

The clinical data was collected at King's College London (KCL) and Guy's Hospital, London. Sustained monomorphic VT was induced in agreement with the VT stimulation protocol by Wellens *et al.* [199] with the goal of deciding on whether to implant a cardioverter defibrillator. The generation of a realistic patient volume conductor model and BSPM signal processing was performed by W. Schulze. Details on data acquisition and first results of noninvasive imaging can be found in his PhD thesis [35].

In the present work, BEM meshes were generated for representing the patient's geometry. Transmembrane potentials were reconstructed with a spatio-temporal approach imposing nondecreasing behavior on TMP.

13.2.1 Geometrical Model

For the inverse calculations, BEM in combination with the surface TMP model was used. The volume conductor model was represented by four inhomogeneity compartments: torso and heart, blood masses, lungs and liver tissue types were considered. The electrical conductivities were assigned as follows: 0.2 S/m for for torso and heart, 0.6 S/m for ventricular blood, 0.04 S/m for lungs and liver [74].

13.2.2 ECG Imaging

The inverse problem of ECG was solved for the time-span indicated by Fig. 13.1. In the case of a monomorphic VT, the regular macroreentrant wave follows a circuit caused by an excitation block with slowed conduction. Repetitive nature of a monomorphic VT explains periodicity in the resulting ECG signal.

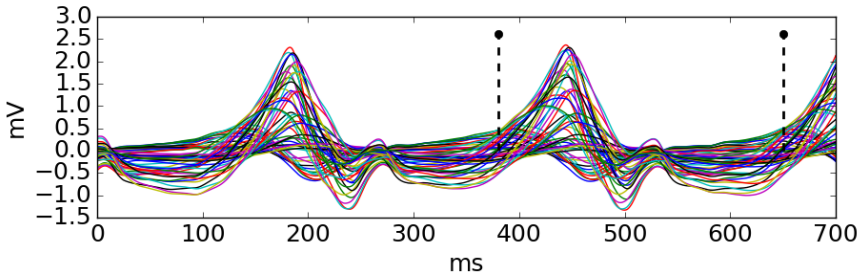

Figure 13.1: Repetitive BSPM pattern for the case of monomorphic VT. Annotated is the time span used for the inverse reconstructions.

13.2.3 Validation Data

For recording endocardial signals, a non-contact mapping system with a multi-electrode array (MEA) positioned in the left ventricular cavity was used [200]. From the obtained MEA measurements, activation maps for a simplified endocardial shell were computed with the EnSite system™[201, 202] of St. Jude Medical, Inc. The shell co-registration with the cardiac magnetic resonance (CMR) model was accomplished using anatomical landmarks [77].

Ventricular scar was obtained from delayed Gadolinium enhancement CMR [203].

13.3 Results

A temporal sequence of TMV reconstructed with the constraint optimization approach is shown in Fig. 13.2. In all plots, TMV distributions are scaled according to their individual maxima and minima. Although these color-coded temporal changes revealed a clear rotational pattern of the depolarization wavefront, calculation of activation times as time

instances exhibiting the largest positive derivative of TMV resulted in big clusters of points with the same AT values and, therewith, failed to reflect the observed propagation feature.

To overcome this challenge and qualitatively assess reconstruction quality in terms of AT, they were assigned point-wise as the first time instances when the local TMP exceeded the 80% value of its maximum. Thus calculated activation times map along with data obtained from the EnSite system are visualized in Fig. 13.3. Similar to the EnSite map, reconstructed AT feature large areas with almost identical activation times. Compared to the validation data projected on the heart model used for inverse calculations (see Fig. 13.3a), the region with earliest activation is shifted to the anterior basal part of the LV.

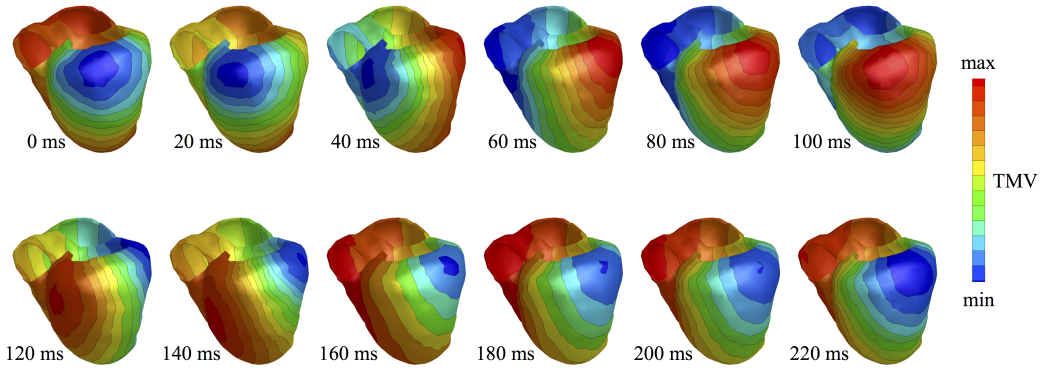

Figure 13.2: Sequence of reconstructed TMV for the sustained VT. Color-coded TMV distributions exhibit a clear rotational pattern.

With regard to the scar area, analysis of amplitudes and morphology for the reconstructed TMV did not reveal any significant discrepancies between scar and healthy nodes.

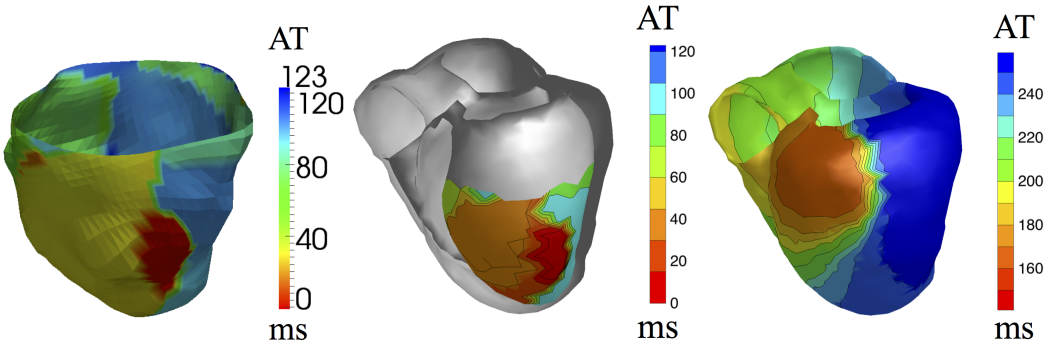

(a) EnSite AT **(b)** Projected AT **(c)** Reconstructed AT

Figure 13.3: Activation time sequences. (a) activation times delivered by the EnSite system; (b) Ensite data projected onto the heart model; (c) activation times derived from the reconstructed TMV values.

13.4 Discussion

The present results should be considered in the context of previous work accomplished at our institute. In [35], the preprocessing steps including co-registration of imaging modalities and model generation are described in detail. Furthermore, the spatio-temporal Tikhonov-Greensite algorithm had been applied for noninvasive imaging of sustained VT. In this study, a BEM model for numerical calculations was created and the inverse analysis was extended by a constraint optimization algorithm.

The considered inverse procedure imposes nondecreasing temporal behavior on the sought TMV. This monotonicity assumption is not valid for a reentrant VT, as in this case the heart does not fully achieve resting state and some cells get electrically re-excited before the depolarization wavefront cover complete heart. However, this violation forced by the inverse algorithm occurs only at the end of a reentrant beat, which explains its ability to realistically reconstruct the underlying activation sequence. The reconstructed rotational pattern of AT is in good agreement with both validation data and results obtained with the Tikhonov-Greensite method [35]. The regularization algorithm based on the low-order BSPM parametrization with splines was also tested in the scope of this work [46]. However, the calculated solutions could not catch the propagation pattern as well as the presented method and are, therefore, not displayed here. This observation suggests necessity of further investigations on the solution quality in terms of endo/epicardial potentials (EP). On one hand, EP imaging impedes direct inclusion of cellular electrophysiological properties into the inverse scheme as it is possible for the well-defined temporal TMV course. On the other hand, presence of scar would not violate assumptions underlying the pericardial potentials source model, which might lead to some improvements in localization of scar and VT exit point. As it was reported in [173], EP-derived activation times resulted in isochronal crowding on the scar contour for induced VT cases. In the present study, however, no information on scar location could be revealed from the calculated TMV values. It might be the algorithm's assumption that hindered such localization by imposing too strong temporal constraints, whereas TMV amplitude analysis performed for Tikhonov-Greensite reconstructions was able to create a hypothesis concerning scar properties [35]. Nevertheless, the threshold values introduced for this purpose ([35]) seem to be rather empirical and the proposed approach should be first confirmed by other experiments before making any strong claims on the performance of different inverse techniques.

With regard to validation data provided by the EnSite system, note that activation times were reconstructed by this commercial software from the electrograms measured by an intracavitary baloon. This procedure represents another inverse problem that delivers highly reliable results only when the baloon surface is proximal to the endocardial surface. As seen in Fig. 13.3a, the activation pattern delivered by the EnSite system exhibited step-like propagation with quite big areas depolarized at approximately the same time, whereas one would rather expect a continuous wavefront.

In order to support the noninvasive imaging by fully exploiting information available from other imaging modalities, one should definitely consider inclusion of the scar into

the numerical model for forward calculations. It could potentially lead to significant improvements when used for generation of a patient-specific transfer matrix and would also enable application of promising model-based methods. In [187], a feasibility study was reported on image-based simulations to estimate ablation target for VT cases. The scar zone and heterogeneous zone hypothesized to be responsible for reentry evolution were defined according to the signal intensity of MR images with late gadolinium enhancement (LGE). In image-based stimulation protocols performed for 13 patients, VT was inducible for 12 patients. Of 11 patients who underwent ablation, in 8 patients the *in silico* estimated target region was associated with success in the standard ablation procedure [187]. However, no quantitative analysis was possible, as it was not possible to retrospectively identify the ablation lesions that led to VT termination. Although the patient group was small and the outcome of such simulation studies might heavily depend on the LGE image quality, these limitations only emphasize importance of synergy between noninvasive imaging modalities. Further steps are necessary to combine image-based heart simulations with the volume conductor model, BSPM recordings and the 'classical' inverse problem of ECG.

CHAPTER 14

Conclusion

In this thesis, performance of noninvasive imaging was evaluated in simulation and clinical scenarios. Furthermore, some aspects of forward ECG modeling were covered.

First, simulation of magnetocardiograms (MCG) was considered within the bidomain model. ECG and MCG signals were calculated for a realistic human torso model in presence of ischemia exhibiting varying transmural extent. As well-known, ECG is a standard tool for diagnosis of acute myocardial ischemia with the diagnosis mostly made according to the shifts of ST segment. One simulated intermediate setup resulted in an ST segment of ECG almost indistinguishable from the control case. However, MCG was also not able to detect any abnormalities compared to the healthy setup, which was probably caused by simplified elliptical form of the modeled ischemia leading to currents compensation. Although one could create some virtual ischemia configurations that produce zero electric but nonvanishing magnetic fields and vice versa, clinical studies are required for better understanding of underlying mechanisms. Besides, further investigations should be devoted to efficient combination of both modalities and development of robust spatio-temporal features that would improve detection rate of electrically silent acute ischemia.

Next, a novel method for estimating BSPM changes in case of varying conductivities was presented. Electric potentials as function of conductivities were approximated by a Taylor expansion around the default value. A numerically calculated gradient was revealed to grasp the main direction of BSPM changes in case of variation in a single tissue. Subsequently, simultaneous variation of conductivity values in three tissue classes was analyzed. Corresponding BSPM changes could be well described by assuming additive characteristics of single ECG variations. As gradients were computed for the whole body volume, one of the main advantages of the presented first-order approximation consists in its capability of visualizing regions most sensitive to uncertainty in conductivity values.

With regard to the noninvasive electrocardiographic imaging, several new techniques were proposed and evaluated in terms of PVC localization accuracy in a simulation study. Activation sequences were calculated with a monodomain model. Subsequently, BSPM were forwardly computed based on bidomain theory with an anisotropic heart model. In order to keep the study more realistic, inverse reconstructions were performed for TMV on

the heart surface, thus neglecting cardiac anisotropy. Some of the proposed methods were constructed for detection of early excitation site based on ECG signals corresponding to a QRS initial time instant. Other methods enabled a sequential solution of the inverse problem over the whole temporal domain and reconstruction of activation patterns. Nevertheless, it is believed that some methodologies, e.g. the binary optimization approach, could be seamlessly extended to corresponding spatio-temporal analogues.

Said that, one can reasonably conjecture that regularization algorithms accounting for temporal solution dynamics should in general perform best for ECG imaging. In the scope of this thesis, performance of two state-of-the-art spatio-temporal regularization techniques was investigated.

Noninvasive imaging of cardiac AT poses a nonlinear least-square optimization problem that is highly sensitive to the initialization due to multiple local minima. Recently, promising results have been reported for an initial estimate calculated with the fastest route algorithm (FRA). In this thesis, the robustness of FRA-based initialization was shown with respect to the common modeling errors: volume conductor simplifications, omission of cardiac anisotropy, geometrical errors. The analysis was conducted under the assumption of knowing conduction velocities (CV), which suggests further investigations on more realistic CV values and their incorporation into a propagation model for inverse calculations. In addition, the correlation maps provided by FRA represent a valuable tool on its own, as they enable quantification of possible inverse solution uncertainties without involving complex stochastic models. They are easily interpretable and could be of immediate importance in the clinical daily practice.

Next, influence of cardiac anisotropy on the ECG imaging results was investigated. For this project, no knowledge about CVs was employed in the estimation of surface TMP-based sources. Along with a rule-based FRA, a constraint optimization approach imposing temporal nondecreasing behavior on TMV was considered for inverse computations. Performance of both algorithms was evaluated for three cases of bidomain conductivity tensors: isotropic, equal and unequal anisotropy ratios in the intra- and extracellular domains. The study revealed comparable performance of the examined solvers across the conductivity setups and localization accuracy was found to be rather dependent on the focal site origin. These effects should be further investigated in order to amend an uncertainty map of PVC localization. Although the spatio-temporal data-driven approach resulted in smaller euclidean distance errors, FRA-computed activation sequences performed superior in classification of being either of endo- or epicardial origin. The overall solution quality demonstrated the ability of the surface TMV source model to produce results comparable to an idealized case of FEM reconstructions. These observations suggested that cardiac anisotropy might be neglected and surface-based TMP models with BEM can be employed in clinical application of the considered inverse procedures.

Subsequently, performance of these two regularization approaches was evaluated in the clinical context of PVC localization. Despite presence of outliers and higher localization errors, the obtained results could indicate limitations of both methods and give some insights on possible imaging improvements. Due to clinical restrictions, placement of electrodes

was possible only on the anterior chest wall in this study. Furthermore, some channels were dismissed due to very poor signal-to-noise ratio. In case of very limited ECG information (27 leads for Patient 19), Tikhonov regularization exhibited performance superior over the correlation-based approach. However, localization accuracy of the considered methods was qualitatively not consistent over the patients. This observation suggests strong dependency on the data quality rather than on intrinsic properties of regularization schemes. With this respect, further attempts should target more efficient combination of both approaches while preserving their best reconstruction features. Note that this validation study was the first of its kind in our institute. Therefore, it is believed that all steps in the processing pipeline could and should be optimized in order to achieve an imaging performance similar to the *in silico* investigations presented in this thesis.

Within another project, accuracy of inverse reconstructions was evaluated for localization of scar-related PVC. Presence of scar had been previously reported to impair performance of the noninvasive imaging, which incited the presented analysis. While the scar was simulated as passive tissue and, therefore, excluded from the excitation propagation model, no corresponding assumptions were accounted for in the inverse procedure. The obtained localization results could be regarded as the proof-of-concept for applicability of the surface TMP source model in noninvasive imaging of scar-related ectopic beats. One possible direction of further research would be the creation of a more realistic scar model and its proper integration into the inverse procedure.

Finally, noninvasive imaging was applied to a beat of sustained ventricular tachycardia (VT). The calculated inverse results were in good qualitative agreement with both validation data and previously reported solutions for this dataset. However, further improvements are needed for more accurate localization of VT exit point. Besides that, integration of fibrotic substrate bearing arrhythmogenic properties should be considered for forward as well as inverse calculations.

To conclude, many aspects of the forward and inverse ECG modeling have been covered in this thesis. Novel regularization techniques were presented and their possible improvements outlined. Performance of two state-of-the-art spatio-temporal approaches was evaluated in highly realistic simulation scenarios. In addition, noninvasive imaging was considered in clinical context of two validation studies that conveyed current limitations of this technique and future prospectives of research. Summarizing, ECG imaging could contribute to all stages of clinical treatment, including decision making, planning of invasive intervention and real-time monitoring of heart condition. In the near future, this technology might become a novel clinical standard facilitating improved diagnostic and increased therapy success.

References

[1] F. H. Martini, *Fundamentals of anatomy & physiology*, L. Berriman, Ed. Prentice Hall, Inc. Upper Saddle River, NJ: Benjamin-Cummings Publishing Company, 2006.

[2] D. U. J. Keller, *Multiscale modeling of the ventricles: from cellular electrophysiology to body surface electrocardiograms*. Karlsruhe: KIT Scientific Publishing, 2011.

[3] G. Seemann, *Modeling of electrophysiology and tension development in the human heart*. Universitätsverlag Karlsruhe, 2005.

[4] T. Fritz, *Biomechanical modeling of the human heart - modeling of the ventricles, the atria and the pericardium and the inverse problem of cardiac mechanics*, Karlsruhe, 2015.

[5] S. Yuan, P. Blomström, S. Pehrson, et al., "Localization of cardiac arrhythmias: conventional noninvasive methods," *Int J Card Imag*, vol. 7, no. 3-4, pp. 193–205, 1991.

[6] M. Fereniec, G. Stix, M. Kania, et al., "Risk assessment of ventricular arrhythmia using new parameters based on high resolution body surface potential mapping," *Med Sci Monit*, vol. 17, no. 3, pp. Mt26–33, 2011.

[7] A. J. J. McClelland, C. G. Owens, I. B. A. Menown, et al., "Comparison of the 80-lead body surface map to physician and to 12-lead electrocardiogram in detection of acute myocardial infarction," *Am J Cardiol*, vol. 92, no. 3, pp. 252–257, 2003.

[8] A. S. Revishvili, E. Wissner, D. S. Lebedev, et al., "Validation of the mapping accuracy of a novel non-invasive epicardial and endocardial electrophysiology system," *Europace*, vol. 17, no. 8, pp. 1282–1288, 2015.

[9] D. Erkapic, H. Greiss, D. Pajitnev, et al., "Clinical impact of a novel three-dimensional electrocardiographic imaging for non-invasive mapping of ventricular arrhythmias?a prospective randomized trial," *Europace*, vol. 17, no. 4, pp. 591–597, 2015.

[10] L. Tung, *A bidomain model for describing ischemic myocardial DC potentials*. Massachusetss Institute of Technology, 1978.

[11] K. H. W. J. ten Tusscher and A. V. Panfilov, "Alternans and spiral breakup in a human ventricular tissue model," *Am J Physiol Heart Circ Physiol*, vol. 291, no. 3, pp. H1088–1100, 2006.

[12] J. Keener and J. Sneyd, "Mathematical physiology i: Cellular physiology, II: Systems physiology," 2009.

[13] M. Potse, B. Dubé, J. Richter, et al., "A comparison of monodomain and bidomain reaction-diffusion models for action potential propagation in the human heart," *IEEE Trans Biomed Eng*, vol. 53, no. 12, pp. 2425–2435, 2006.

[14] G. Seemann, F. B. Sachse, M. Karl, et al., "Framework for modular, flexible and efficient solving the cardiac bidomain equation using PETSc," *Math Ind*, vol. 15, no. 2, pp. 363–369, 2010.

[15] O. Skipa, *Linear inverse problem of electrocardiography: epicardial potentials and transmembrane voltages*. Helmes Verlag Karlsruhe, 2004.

[16] A. van Oosterom and T. F. Oostendorp, *Electric volume conduction in bio-medicine, syllabus at Radboud University Nijmegen*, the Netherlands, 2015.

[17] D. B. Geselowitz, "Description of cardiac sources in anisotropic cardiac muscle. application of bidomain model," *J Electrocardiol*, vol. 25, no. Suppl, pp. 65–67, 1992.

[18] T. Oostendorp and A. Van Oosterom, "Source parameter estimation in inhomogeneous volume conductors of arbitrary shape," *IEEE Trans Biomed Eng*, vol. 36, no. 3, pp. 382–391, 1989.

[19] M. Lynn and W. Timlake, "The use of multiple deflations in the numerical solution of singular systems of equations, with applications to potential theory," *SIAM J Numer Anal*, vol. 5, no. 2, pp. 303–322, 1968.

[20] J. J. M. Cuppen and A. Van Oosterom, "Model studies with the inversely calculated lsochrones of ventricular depolarization," *IEEE Trans Biomed Eng*, pp. 652–659, 1984.

[21] G. J. M. Huiskamp and A. v. Oosterom, "The depolarization sequence of the human heart surface computed from measured body surface potentials," *IEEE Trans Biomed Eng*, vol. 35, no. 12, pp. 1047–1058, 1988.

[22] A. van Oosterom, "Genesis of the T wave as based on an equivalent surface source model," *J Electrocardiol*, vol. 34 Suppl, pp. 217–227, 2001.

[23] A. van Oosterom and V. Jacquemet, "Genesis of the P wave: atrial signals as generated by the equivalent double layer source model," *Europace*, vol. 7 Suppl 2, pp. 21–29, 2005.

[24] J. S. Hadamard, "Sur les problèmes aux dérivées partielles et leur signification physique," *Princeton University Bulletin*, vol. 13, pp. 49–52, 1902.

[25] R. C. Barr, M. Ramsey III, and M. S. Spach, "Relating epicardial to body surface potential distributions by means of transfer coefficients based on geometry measurements," *IEEE Trans Biomed Eng*, no. 1, pp. 1–11, 1977.

[26] M. C. MacLachlan, B. F. Nielsen, M. Lysaker, et al., "Computing the size and location of myocardial ischemia using measurements of ST-segment shift," *IEEE Trans Biomed Eng*, vol. 53, no. 6, pp. 1024–1031, 2006.

[27] Z. Liu, C. Liu, and B. He, "Noninvasive reconstruction of three-dimensional ventricular activation sequence from the inverse solution of distributed equivalent current density," *IEEE Trans Med Imag*, vol. 25, no. 10, pp. 1307–1318, 2006.

[28] B. Tilg, G. Fischer, R. Modre, et al., "Model-based imaging of cardiac electrical excitation in humans," *IEEE Trans Med Imag*, vol. 21, no. 9, pp. 1031–1039, 2002.

[29] M. P. Nash and A. J. Pullan, "Challenges facing validation of noninvasive electrical imaging of the heart," *Ann Noninvasive Electrocardiol*, vol. 10, no. 1, pp. 73–82, 2005.

[30] P. M. van Dam, T. F. Oostendorp, A. C. Linnenbank, et al., "Non-invasive imaging of cardiac activation and recovery," *Ann Biomed Eng*, vol. 37, no. 9, pp. 1739–1756, 2009.

[31] Y. Rudy, "Noninvasive electrocardiographic imaging of arrhythmogenic substrates in humans," *Circ Res*, vol. 112, no. 5, pp. 863–874, 2013.

[32] B. He, G. Li, and X. Zhang, "Noninvasive imaging of cardiac transmembrane potentials within three-dimensional myocardium by means of a realistic geometry anisotropic heart model," *IEEE Trans Biomed Eng*, vol. 50, no. 10, pp. 1190–1202, 2003.

[33] B. F. Nielsen, M. Lysaker, and P. Grottum, "Computing ischemic regions in the heart with the bidomain model-first steps towards validation," *IEEE Trans Med Imag*, vol. 32, no. 6, pp. 1085–1096, 2013.

[34] L. Wang, F. Dawoud, S.-K. Yeung, et al., "Transmural imaging of ventricular action potentials and post-infarction scars in swine hearts," *IEEE Trans Med Imag*, vol. 32, no. 4, pp. 731–747, 2013.

[35] W. H. W. Schulze, *ECG imaging of ventricular activity in clinical applications*. Karlsruhe: KIT Scientific Publishing, 2015.

[36] L. Yu, Z. Zhou, and B. He, "Temporal sparse promoting three dimensional imaging of cardiac activation," *IEEE Trans Med Imag*, 2015.

[37] B. Messnarz, B. Tilg, R. Modre, et al., "A new spatiotemporal regularization approach for reconstruction of cardiac transmembrane potential patterns," *IEEE Trans Biomed Eng*, vol. 51, no. 2, pp. 273–281, 2004.

[38] J. Coll-Font, D. Potyagayo, W. Schulze, et al., "Comparison of temporal dimensionality reduction methods for constrained inverse in cardiac electrical imaging," in *Comput Cardiol*, 2015, pp. 237–240.

[39] R. Modre, B. Tilg, G. Fischer, et al., "Noninvasive myocardial activation time imaging: a novel inverse algorithm applied to clinical ECG mapping data," *IEEE Trans. Biomed. Eng.*, vol. 49, no. 10, pp. 1153–1161, 2002.

[40] B. Erem, P. M. van Dam, and D. H. Brooks, "Identifying model inaccuracies and solution uncertainties in noninvasive activation-based imaging of cardiac excitation using convex relaxation," *IEEE Trans Med Imag*, vol. 33, no. 4, pp. 902–912, 2014.

[41] T. F. Oostendorp, A. van Oosterom, and G. Fischer, "Multi foci based initial estimate for cardiac activation time mapping," in *Proc Int Cong Electrocardiol*, 2006, p. 18.

[42] B. Erem, P. van Dam, A. Keely, et al., "Methods for initialization of activation based inverse electrocardiography using graphs derived from heart surface geometry," in *Comput Cardiol*, 2009, pp. 189–192.

[43] P. M. van Dam, T. F. Oostendorp, and A. van Oosterom, "Application of the fastest route algorithm in the interactive simulation of the effect of local ischemia on the ECG," *Med Biol Eng Comput*, vol. 47, no. 1, pp. 11–20, 2009.

[44] P. M. van Dam, R. Tung, K. Shivkumar, et al., "Quantitative localization of premature ventricular contractions using myocardial activation ECGI from the standard 12-lead electrocardiogram," *J Electrocardiol*, vol. 46, no. 6, pp. 574–579, 2013.

[45] B. Erem, D. H. Brooks, P. M. van Dam, et al., "Spatiotemporal estimation of activation times of fractionated ECGs on complex heart surfaces," in *Conf Proc IEEE Eng Med Biol Soc*, 2011, pp. 5884–5887.

[46] B. Erem, J. Coll-Font, R. M. Orellana, et al., "Using transmural regularization and dynamic modeling for noninvasive cardiac potential imaging of endocardial pacing with imprecise thoracic geometry," *IEEE Trans Med Imag*, vol. 33, no. 3, pp. 726–738, 2014.

[47] P. C. Hansen and P. C. O'Leary, "The use of the l-curve in the regularization of discrete ill-posed problems," *SIAM J. Scientific Computing*, vol. 14, no. 6, pp. 1487–1503, 1993.

[48] H. M. Bolooki and A. Askari, "Acute myocardial infarction," *Disease Manag Proj*, 2010.

[49] W. E. Cascio, H. Yang, B. J. Muller-Borer, et al., "Ischemia-induced arrhythmia: the role of connexins, gap junctions, and attendant changes in impulse propagation," *J Electrocardiol*, vol. 38, no. 4 Suppl, pp. 55–59, 2005.

[50] M. Wilhelms, O. Dössel, and G. Seemann, "In silico investigation of electrically silent acute cardiac ischemia in the human ventricles," *IEEE Trans Biomed Eng*, vol. 58, no. 10, pp. 2961–2964, 2011.

[51] B. Rodriguez, B. M. Tice, J. C. Eason, et al., "Cardiac vulnerability to electric shocks during phase 1a of acute global ischemia," *Heart Rhythm : the Official Journal of the Heart Rhythm Society*, vol. 1, no. 6, pp. 695–703, 2004.

[52] D. Potyagaylo, G. Seemann, W. Schulze, et al., "Magnetocardiography did not uncover electrically silent ischemia in an in-silico study case," in *Comput Cardiol*, vol. 42, 2015, pp. 1145–1148.

[53] P. Takala, H. Hanninen, J. Montone, et al., "Magnetocardiographic and electrocardiographic exercise mapping in healthy subjects," *Ann Biomed Eng*, vol. 29, no. 6, pp. 501–509, 2001.

[54] V. Mantynen, T. Konttila, and M. Stenroos, "Investigations of sensitivity and resolution of ECG and MCG in a realistically shaped thorax model," *Phys Med Biol*, vol. 59, no. 23, pp. 7141–7158, 2014.

[55] B. J. Roth and J. P. J. Wikswo, "Electrically silent magnetic fields," *Biophys J*, vol. 50, no. 4, pp. 739–745, 1986.

[56] J. Lant, G. Stroink, and B. J. tenVoorde, "Complementary nature of electrocardiographic and magnetocardiographic data in patients with ischemic heart disease," *J Electrocardiol*, vol. 23, no. 4, pp. 315–322, 1990.

[57] D. U. J. Keller, F. M. Weber, G. Seemann, et al., "Ranking the influence of tissue conductivities on forward-calculated ECGs," *IEEE Trans Biomed Eng*, vol. 57, no. 7, pp. 1568–1576, 2010.

[58] H.-H. Osterhues, V. Hombach, and A. J. Moss, *Advances in noninvasive electrocardiographic monitoring techniques*, vol. 229. Springer Science & Business Media, 2000.

[59] J.-W. Park, P. M. Hill, N. Chung, et al., "Magnetocardiography predicts coronary artery disease in patients with acute chest pain," *Ann Noninvasive Electrocardiol*, 2005.

[60] H. Kyoon Lim, K. Kim, Y.-H. Lee, et al., "Detection of non-st-elevation myocardial infarction using magnetocardiogram: New information from spatiotemporal electrical activation map," *Ann Med*, vol. 41, no. 7, pp. 533–546, 2009.

[61] A. Loewe, W. H. W. Schulze, Y. Jiang, et al., "ECG-based detection of early myocardial ischemia in a computational model: impact of additional electrodes, optimal placement, and a new feature for st deviation," *BioMed Res Int*, 2015.

[62] C. P. Bradley, A. J. Pullan, and P. J. Hunter, "Effects of material properties and geometry on electrocardiographic forward simulations," *Ann Biomed Eng*, vol. 28, no. 7, pp. 721–741, 2000.

[63] Y. Rudy, R. Plonsey, and J. Liebman, "The effects of variations in conductivity and geometrical parameters on the electrocardiogram, using an eccentric spheres model," *Circ Res*, vol. 44, no. 1, pp. 104–111, 1979.

[64] T. J. C. Faes, H. A. v. d. Meij, J. C. d. Munck, et al., "The electric resistivity of human tissues (100 Hz-10 MHz) a meta-analysis of review studies," *Physiol Meas*, vol. 20, no. 4, p. R1, 1999.

[65] R. N. Klepfer, C. R. Johnson, and R. S. MacLeod, "The effects of inhomogeneities and anisotropies on electrocardiographic fields: a 3-d finite-element study," *IEEE Trans Biomed Eng*, vol. 44, no. 8, pp. 706–719, 1997.

[66] S. E. Geneser, R. M. Kirby, and R. S. MacLeod, "Application of stochastic finite element methods to study the sensitivity of ECG forward modeling to organ conductivity," *IEEE Trans Biomed Eng*, vol. 55, no. 1, pp. 31–40, 2008.

[67] F. M. Weber, D. U. J. Keller, S. Bauer, et al., "Predicting tissue conductivity influences on body surface potentials-an efficient approach based on principal component analysis," *IEEE Trans Biomed Eng*, vol. 58, no. 2, pp. 265–273, 2011.

[68] J. A. Nelder and R. Mead, "A simplex method for function minimization," *The computer journal*, vol. 7, no. 4, pp. 308–313, 1965.

[69] D. Potyagaylo, O. Dössel, and P. van Dam, "Influence of modeling errors on the initial estimate for nonlinear myocardial activation times imaging calculated with fastest route algorithm," *IEEE Trans Biomed Eng*, vol. PP, no. 99, pp. 1–1, 2016.

[70] M. Haissaguerre, M. Hocini, A. J. Shah, et al., "Noninvasive panoramic mapping of human atrial fibrillation mechanisms: a feasibility report," *J Cardiovasc Electrophysiol*, vol. 24, no. 6, pp. 711–717, 2013.

[71] R. Dubois, A. J. Shah, M. Hocini, et al., "Non-invasive cardiac mapping in clinical practice: Application to the ablation of cardiac arrhythmias," *J Electrocardiol*, vol. 48, no. 6, pp. 966–974, 2015.

[72] B. Erem, P. M. van Dam, and D. H. Brooks, "Analysis of the criteria of activation-based inverse electrocardiography using convex optimization," in *Conf Proc IEEE Eng Med Biol Soc*, 2011, pp. 3913–3916.

[73] B. Erem, P. M. van Dam, and D. H. Brooks, "A convex relaxation framework for initialization of activation-based inverse electrocardiography," in *Conf Proc IEEE Eng Med Biol Soc*, 2011, pp. 12–17.

[74] S. Gabriel, R. W. Lau, and C. Gabriel, "The dielectric properties of biological tissues: Iii. parametric models for the dielectric spectrum of tissues," *Phys Med Biol*, vol. 41, pp. 2271–2293, 1996.

[75] A. Oosterom van and P. M. van Dam, "The intra-myocardial distance function as used in the inverse computation of the timing of depolarization and repolarization," in *Comput Cardiol*, 2005.

[76] R. N. Ghanem, C. Ramanathan, P. Jia, et al., "Heart-surface reconstruction and ECG electrodes localization using fluoroscopy, epipolar geometry and stereovision: application to noninvasive imaging of cardiac electrical activity," *IEEE Trans Med Imag*, vol. 22, no. 10, pp. 1307–1318, 2003.

[77] M. YingLiang, U. Mistry, A. Thorpe, et al., "Automatic electrode and CT/MR image co-localisation for electrocardiographic imaging," in *FIMH, LNCS 7945*, S. Ourselin, D. Rueckert, and N. Smith, Eds. Springer, 2013, pp. 268–275.

[78] C. Ramanathan and Y. Rudy, "Electrocardiographic imaging: I. effect of torso inhomogeneities on body surface electrocardiographic potentials," *J Cardiovasc Electrophysiol*, vol. 12, no. 2, pp. 229–240, 2001.

[79] M. Potse, B. Dube, and A. Vinet, "Cardiac anisotropy in boundary-element models for the electrocardiogram," *Med Biol Eng Comput*, vol. 47, no. 7, pp. 719–729, 2009.

[80] G. Fischer, B. Tilg, R. Modre, et al., "A bidomain model based BEM-FEM coupling formulation for anisotropic cardiac tissue," *Ann Biomed Eng*, vol. 28, no. 10, pp. 1229–1243, 2000.

[81] H. S. Oster, B. Taccardi, R. L. Lux, et al., "Electrocardiographic imaging noninvasive characterization of intramural myocardial activation from inverse-reconstructed epicardial potentials and electrograms," *Circulation*, vol. 97, no. 15, pp. 1496–1507, 1998.

[82] C. Liu and B. He, "Effects of cardiac anisotropy on three-dimensional ECG localization inverse solutions: a model study," *IJBEM*, vol. 7, pp. 221–222, 2005.

[83] R. Modre, M. Seger, G. Fischer, et al., "Cardiac anisotropy: is it negligible regarding non-invasive activation time imaging?" *IEEE Trans Biomed Eng*, vol. 53, no. 4, pp. 569–580,

2006.

[84] G. J. Huiskamp and A. van Oosterom, "Heart position and orientation in forward and inverse electrocardiography," *Med Biol Eng Comput*, vol. 30, no. 6, pp. 613–620, 1992.

[85] B. He, G. Li, and X. Zhang, "Noninvasive three-dimensional activation time imaging of ventricular excitation by means of a heart-excitation model," *Phys Med Biol*, vol. 47, no. 22, pp. 4063–4078, 2002.

[86] M. Jiang, L. Xia, G. Shou, et al., "Combination of the LSQR method and a genetic algorithm for solving the electrocardiography inverse problem," *Phys Med Biol*, vol. 52, no. 5, p. 1277, 2007.

[87] Y. Jiang, *Solving the inverse problem of electrocardiography in a realistic environment*. KIT Scientific Publishing, 2010.

[88] U. C. Nguyen, M. Potse, F. Regoli, et al., "An in-silico analysis of the effect of heart position and orientation on the ECG morphology and vectorcardiogram parameters in patients with heart failure and intraventricular conduction defects," *J Electrocardiol*, vol. 48, no. 4, pp. 617–625, 2015.

[89] J. E. Burnes, B. Taccardi, and Y. Rudy, "A noninvasive imaging modality for cardiac arrhythmias," *Circulation*, vol. 102, pp. 2152–2158, 2000.

[90] P. van Dam, J. Gordon, and M. Laks, "Sensitivity of CIPS-computed PVC location to measurement errors in ECG electrode position: the need for the 3d camera," *J Electrocardiol*, vol. 47, no. 6, pp. 788–793, 2014.

[91] P. M. van Dam, J. P. Gordon, M. M. Laks, et al., "Development of new anatomy reconstruction software to localize cardiac isochrones to the cardiac surface from the 12 lead ECG," *J Electrocardiol*, vol. 48, no. 6, pp. 959–965, 2015.

[92] A. SippensGroenewegen, H. Spekhorst, N. M. v. Hemel, et al., "Body surface mapping of ectopic left and right ventricular activation - QRS spectrum in patients without structural heart disease," *Circulation*, vol. 82, pp. 879–896, 1990.

[93] M. Wallman, N. P. Smith, and B. Rodriguez, "A comparative study of graph-based, eikonal, and monodomain simulations for the estimation of cardiac activation times," *IEEE Trans Biomed Eng*, vol. 59, no. 6, pp. 1739–1748, 2012.

[94] J. Xu, A. R. Dehaghani, F. Gao, et al., "Noninvasive transmural electrophysiological imaging based on minimization of total-variation functional," *IEEE Trans Med Imag*, vol. 33, no. 9, pp. 1860–1874, 2014.

[95] Z. Zhou, C. Han, T. Yang, et al., "Noninvasive imaging of 3-dimensional myocardial infarction from the inverse solution of equivalent current density in pathological hearts," *IEEE Trans Biomed Eng*, vol. 62, no. 2, pp. 468–476, 2015.

[96] P. C. Franzone, L. F. Pavarino, and B. Taccardi, "Simulating patterns of excitation, repolarization and action potential duration with cardiac bidomain and monodomain models," *Math Biosc*, vol. 197, no. 1, pp. 35–66, 2005.

[97] B. J. Roth, "Electrical conductivity values used with the bidomain nodel of cardiac tissue," *IEEE Trans Biomed Eng*, vol. 44, no. 4, pp. 326–328, 1997.

[98] A. N. Tikhonov and V. Y. Arsenin, *Solutions of ill-posed problem*. Winston&Sons, New York, 1977.

[99] D. Potyagaylo, W. H. W. Schulze, and O. Dössel, "Local regularization of endocardial and epicardial surfaces for better localization of ectopic beats in the inverse problem of ECG," in *Comput Cardiol*, vol. 41, 2014, pp. 837–840.

[100] F. Bauer and M. A. Lukas, "Comparing parameter choice methods for regularization of ill-posed problems," *Math Comput Simulat*, vol. 81, no. 9, pp. 1795–1841, 2011.

[101] Y. Voskoboinikov and A. Micel, "Modern problems of applied mathematics, part 1," *Tomsk State University*, 2010.

[102] D. H. Brooks, G. F. Ahmad, R. S. MacLeod, et al., "Inverse electrocardiography by simultaneous imposition of multiple constraints," *IEEE Trans Biomed Eng*, vol. 46, no. 1, pp. 3–18, 1999.

[103] P. C. Hansen, *Computational inverse problems in electrocardiography*. WIT Press, 2001, ch. The L-curve and its use in the numerical treatment of inverse problems, pp. 119–142.

[104] H. S. Oster and Y. Rudy, "Regional regularization of the electrocardiographic inverse problem: A model study using spherical geometry," *IEEE Trans Biomed Eng*, vol. 44, no. 2, pp. 188–199, 1997.

[105] G. F. Ahmad, D. H. Brooks, and R. S. MacLeod, "An admissible solution approach to inverse electrocardiography," *Ann Biomed Eng*, vol. 26, no. 2, pp. 278–292, 1998.

[106] C. R. Johnson and R. S. MacLeod, "Adaptive local regularization methods for the inverse ECG problem," *Prog Biophys Mol Biol*, vol. 69, no. 2, pp. 405–423, 1998.

[107] D. Lesnic, L. Elliott, and D. Ingham, "An iterative boundary element method for solving numerically the cauchy problem for the laplace equation," *Eng Anal Bound Elem*, vol. 20, pp. 123–133, 1997.

[108] M. Lavrentiev, V. Romanov, and V. Vasiliev, *Multidimensional inverse problems for differential equations*, vol. 167. Springer-Verlag, American Elsevier Publishing Co., 1970.

[109] A. Bakushinsky and M. Kokurin, *Iterative methods for approximate solution of inverse problems*, vol. 577. Springer Science & Business Media, 2005.

[110] V. Kozlov, V. Maz'ya, and A. Fomin, "An iterative method for solving the cauchy problem for elliptic equations," *Zhurnal Vychislitel'noi Matematiki i Matematicheskoi Fiziki*, vol. 31, no. 1, pp. 64–74, 1991.

[111] L. Marin, L. Elliott, P. Heggs, et al., "An alternating iterative algorithm for the cauchy problem associated to the helmholtz equation," *Comput Methed Appl Mech Eng*, vol. 192, no. 5, pp. 709–722, 2003.

[112] D. Maxwell, M. Truffer, S. Avdonin, et al., "An iterative scheme for determining glacier velocities and stresses," *J Glaciol*, vol. 54, no. 188, pp. 888–898, 2008.

[113] F. Belgacem and H. El Fekih, "On cauchy's problem: I. a variational steklov–poincaré theory," *Inverse Problems*, vol. 21, no. 6, p. 1915, 2005.

[114] N. Zemzemi, "A steklov-poincaré approach to solve the inverse problem in electrocardiography," in *Comput Cardiol*, 2013, pp. 703–06.

[115] N. Zemzemi, H. Bourenane, and H. Cochet, "An iterative method for solving the inverse problem in electrocardiography imaging: From body surface to heart potential," in *Comput Cardiol*, 2014, pp. 717–720.

[116] M. Burger, K.-A. Mardal, and B. F. Nielsen, "Stability analysis of the inverse transmembrane potential problem in electrocardiography," *Inverse Problems*, vol. 26, no. 10, p. 105012, 2010.

[117] D. Wang, R. M. Kirby, R. S. Macleod, et al., "An optimization framework for inversely estimating myocardial transmembrane potentials and localizing ischemia," in *Conf Proc IEEE Eng Med Biol Soc*, vol. 2011, 2011, pp. 1680–1683.

[118] D. Potyagaylo, M. Segel, W. H. W. Schulze, et al., "Noninvasive localization of ectopic foci: a new optimization approach for simultaneous reconstruction of transmembrane voltages and

epicardial potentials," in *FIMH, LNCS 7945*. Spinger-Verlag Berlin Heidelberg, 2013, pp. 166–173.

[119] L. Reichel and Q. Ye, "Simple square smoothing regularization operators," *Electron Trans Numer Anal*, vol. 33, pp. 63–83, 2009.

[120] A. Chambolle, "An algorithm for total variation minimization and applications," *J Math Imag Vision*, vol. 20, no. 1-2, pp. 89–97, 2004.

[121] E. Candes and J. Romberg, "l1-magic: Recovery of sparse signals via convex programming," *www.acm.caltech.edu/l1magic/downloads/l1magic.pdf*, vol. 4, p. 46, 2005.

[122] E. J. Candès and Y. Plan, "Near-ideal model selection by âĎŞ1 minimization," *Ann Statist*, vol. 37, no. 5A, pp. 2145–2177, 2009.

[123] S. Ghosh and Y. Rudy, "Application of l1-norm regularization to epicardial potential solution of the inverse electrocardiography problem," *Ann Biomed Eng*, vol. 37, no. 5, pp. 902–912, 2009.

[124] L. Wang, J. Qin, T. T. Wong, et al., "Application of l1-norm regularization to epicardial potential reconstruction based on gradient projection," *Phys Med Biol*, vol. 56, no. 19, p. 6291, 2011.

[125] L. Wang, H. Zhang, K. C. L. Wong, et al., "Physiological-model-constrained noninvasive reconstruction of volumetric myocardial transmembrane potentials," *IEEE Trans Biomed Eng*, vol. 57, no. 2, pp. 296–315, 2010.

[126] L. Wang, K. C. L. Wong, H. Zhang, et al., "Noninvasive computational imaging of cardiac electrophysiology for 3-d infarct," *IEEE Trans Biomed Eng*, vol. 58, no. 4, pp. 1033–1043, 2011.

[127] J. Xu, A. R. Dehaghani, F. Gao, et al., "Noninvasive transmural electrophysiological imaging based on minimization of total-variation functional," *IEEE Trans Med Imag*, vol. 33, no. 9, pp. 1860–1874, 2014.

[128] Y. Wang and W. Yin, "Sparse signal reconstruction via iterative support detection," *SIAM J Imag Sci*, vol. 3, no. 3, pp. 462–491, 2010.

[129] S. Nam, M. E. Davies, M. Elad, et al., "The cosparse analysis model and algorithms," *Appl Comput Harmonic Analys*, vol. 34, no. 1, pp. 30–56, 2013.

[130] S. Ghosh and Y. Rudy, "Application of l1-norm regularization to epicardial potential solution of the inverse electrocardiography problem," *Annals of Biomedical Engineering*, vol. 37, no. 5, pp. 902–912, 2009.

[131] G. Shou, L. Xia, F. Liu, et al., "On epicardial potential reconstruction using regularization schemes with the l1-norm data term," *Phys Med Biol*, vol. 56, no. 1, p. 57, 2011.

[132] D. Wang, R. M. Kirby, R. S. MacLeod, et al., "Inverse electrocardiographic source localization of ischemia: An optimization framework and finite element solution," *J Comput Phys*, vol. 250, pp. 403–424, 2013.

[133] S. Boyd and L. Vandenberghe, *Convex optimization*. Cambridge university press, 2004.

[134] B. Messnarz, B. Tilg, R. Modre, et al., "A new spatiotemporal regularization approach for reconstruction of cardiac transmembrane potential patterns," *IEEE Trans Biomed Eng*, vol. 51, no. 2, pp. 273–281, 2004.

[135] G. Fischer, B. Pfeifer, M. Seger, et al., "Computationally efficient noninvasive cardiac activation time imaging," *Meth Inform Med*, vol. 44, no. 5, p. 674, 2005.

[136] P. M. Pardalos and G. P. Rodgers, "Computational aspects of a branch and bound algorithm for quadratic zero-one programming," *Computing*, vol. 45, no. 2, pp. 131–144, 1990.

[137] C. Helmberg and F. Rendl, "Solving quadratic (0, 1)-problems by semidefinite programs and cutting planes," *Mathematical Programming*, vol. 82, no. 3, pp. 291–315, 1998.

[138] F. Glover, G. A. Kochenberger, and B. Alidaee, "Adaptive memory tabu search for binary quadratic programs," *Manag Sci*, vol. 44, no. 3, pp. 336–345, 1998.

[139] G. Palubeckis, "Iterated tabu search for the unconstrained binary quadratic optimization problem," *Informatica*, vol. 17, no. 2, pp. 279–296, 2006.

[140] K. Katayama and H. Narihisa, "Performance of simulated annealing-based heuristic for the unconstrained binary quadratic programming problem," *Eur J Oper Res*, vol. 134, no. 1, pp. 103–119, 2001.

[141] S. Weber, A. Nagy, T. Schüle, et al., "A benchmark evaluation of large-scale optimization approaches to binary tomography," in *LNCS*, 2006, pp. 146–156.

[142] J. Kennedy and R. C. Eberhart, "A discrete binary version of the particle swarm algorithm," in *IEEE Sys Man Cybern*, vol. 5, 1997, pp. 4104–4108.

[143] P. Merz and B. Freisleben, "Genetic algorithms for binary quadratic programming," in *Genet Evol Comput Conf*, vol. 1, 1999, pp. 417–424.

[144] K. Katayama, M. Tani, and H. Narihisa, "Solving large binary quadratic programming problems by effective genetic local search algorithm," in *Gecco*, 2000, pp. 643–650.

[145] T. Schüle, C. Schnörr, S. Weber, et al., "Discrete tomography by convex-concave regularization and dc programming," *Discrete Appl Math*, vol. 151, pp. 229–243, 2005.

[146] T. Schüle, S. Weber, and C. Schnörr, "Adaptive reconstruction of discrete-valued objects from few projections," *Electron Notes Discrete Math*, vol. 20, pp. 365–384, 2005.

[147] D. Potyagaylo, E. G. Cortes, W. H. W. Schulze, et al., "Binary optimization for source localization in the inverse problem of ECG," *Med Biol Eng Comput*, vol. 52, no. 9, pp. 717–728, 2014.

[148] P. D. Tao and L. T. H. An, "A dc optimization algorithm for solving the trust-region subproblem," *SIAM J Optimiz*, vol. 8, no. 2, pp. 476–505, 1998.

[149] R. T. Rockafellar, *Convex analysis*. Princeton university press, 2015.

[150] L. Wang, "Computational reduction for noninvasive transmural electrophysiological imaging," *Comput Biol Med*, vol. 43, no. 3, pp. 184–199, 2013.

[151] O. Dössel, Y. Jiang, and W. H. W. Schulze, "Localization of the origin of premature beats using an integral method," in *Int J Bioelectromagn*, vol. 13, no. 4, 2011, pp. 178–183.

[152] C. Han, S. M. Pogwizd, C. R. Killingsworth, et al., "Noninvasive reconstruction of the three-dimensional ventricular activation sequence during pacing and ventricular tachycardia in the canine heart," *Am J Physiol*, vol. 302, pp. H244–52, 2012.

[153] H. S. Oster, B. Taccardi, R. L. Lux, et al., "Noninvasive electrocardiographic imaging. reconstruction of epicardial potentials, electrograms and isochrones and localization of single and multiple electrocardiac events," *Circulation*, vol. 96, no. 3, pp. 1012–1024, 1997.

[154] C. Ramanathan, R. N. Ghanem, P. Jia, et al., "Noninvasive electrocardiographic imaging for cardiac electrophysiology and arrhythmia," *Nat Med*, vol. 10, pp. 422–428, 2004.

[155] D. B. Geselowitz, "On the theory of the electrocardiogram," in *IEEE Proc*, vol. 77, no. 6, 1989, pp. 857–876.

[156] D. B. Geselowitz, "Use of time integrals of the ECG to solve the inverse problem," *IEEE Trans Biomed Eng*, vol. BME-32, no. 1, pp. 73–75, 1985.

[157] D. B. Geselowitz and T. W. Miller, "A bidomain model for anisotropic cardiac muscle," *Ann Biomed Eng*, vol. 11, no. 3-4, pp. 191–206, 1983.

[158] B. Taccardi, E. Macchi, R. L. Lux, et al., "Effect of myocardial fiber direction on epicardial potentials," *Circulation*, vol. 90, pp. 3076–3090, 1994.

[159] P. Colli-Franzone, L. Guerri, M. Pennacchio, et al., "Anisotropic mechanisms for multiphasic unipolar electrograms: simulation studies and experimental recordings," *Ann Biomed Eng*, vol. 28, no. 11, pp. 1326–1342, 2000.

[160] A. M. Janssen, D. Potyagaylo, O. Dössel, et al., "Assessment of the equivalent dipole layer source model in the reconstruction of cardiac activation times on the basis of ECGs produced by an anisotropic model of the heart," *Submitted*, 2016.

[161] P. Colli Franzone, L. F. Pavarino, and B. Taccardi, "Simulating patterns of excitation, repolarization and action potential duration with cardiac bidomain and monodomain models," *Math Biosc*, vol. 197, no. 1, pp. 35–66, 2005.

[162] M. Hocini, A. J. Shah, T. Neumann, et al., "Focal arrhythmia ablation determined by high resolution non-invasive maps: Multicenter feasibility study," *J Cardiovasc Electrophysiol*, 2015.

[163] R. Killmann, P. Wach, and F. Dienstl, "Three-dimensional computer model of the entire human heart for simulation of reentry and tachycardia: gap phenomenon and wolff-parkinson-white syndrome," *Basic Res. Cardiol.*, vol. 86, pp. 485–501, 1991.

[164] D. Wang, R. Kirby, and C. Johnson, "Resolution strategies for the finite-element-based solution of the ECG inverse problem," *IEEE Trans Biomed Eng*, vol. 57, no. 2, pp. 220–237, 2010.

[165] C. Hintermüller, M. Seger, B. Pfeifer, et al., *Biomed sim*. Springer, 2006, ch. Simulation of cardiac activation patterns for checking suggestions about the suitability of multi-lead ECG electrode arrays, pp. 105–112.

[166] P. M. van Dam and A. van Oosterom, "Volume conductor effects involved in the genesis of the P wave," *Europace*, vol. 7 Suppl 2, pp. 30–38, 2005.

[167] C. D. Werner, F. B. Sachse, and O. Dössel, "Electrical excitation propagation in the human heart," *Int J Bioelectromagn*, vol. 2, no. 2, 2000.

[168] G. Fischer, B. Tilg, R. Modre, et al., "A bidomain model based BEM-FEM coupling formulation for anisotropic cardiac tissue," *Ann Biomed Eng*, vol. 28, no. 10, pp. 1229–1243, 2000.

[169] N. Toussaint, C. T. Stoeck, T. Schaeffter, et al., "In vivo human cardiac fibre architecture estimation using shape-based diffusion tensor processing," *Med Imag Anal*, vol. 17, no. 8, pp. 1243–1255, 2013.

[170] H. Cochet, R. Dubois, F. Sacher, et al., "Cardiac arrythmias: multimodal assessment integrating body surface ECG mapping into cardiac imaging," *Radiology*, vol. 271, no. 1, pp. 239–247, 2013.

[171] A. J. Shah, H. S. Lim, S. Yamashita, et al., "Non invasive ECG mapping to guide catheter ablation," *J Atr Fibrillation*, vol. 7, no. 3, 2014.

[172] R. N. Ghanem, P. Jia, C. Ramanathan, et al., "Noninvasive electrocardiographic imaging (ECGI): comparison to intraoperative mapping in patients," *Heart Rhythm*, vol. 2, no. 4, pp. 339–354, 2005.

[173] J. L. Sapp, F. Dawoud, J. C. Clements, et al., "Inverse solution mapping of epicardial potentials quantitative comparison with epicardial contact mapping," *Circ Arrhyth Electrophysiol*, vol. 5, pp. 1001–1009, 2012.

[174] C. Han, S. M. Pogwizd, C. R. Killingsworth, et al., "Noninvasive imaging of three-dimensional cardiac activation sequence during pacing and ventricular tachycardia," *Heart Rhythm*, vol. 8, pp. 1266–1272, 2011.

[175] W. H. W. Schulze, P. Mackens, D. Potyagaylo, et al., "Automatic camera-based identification and 3-d reconstruction of electrode positions in electrocardiographic imaging," *Biomed Eng / Biomed Technik*, vol. 59, no. 6, pp. 515–528, 2014.

[176] F. Greesite and G. Huiskamp, "An improved method for estimatimg epicardial potential from the body surface," *IEEE Transactions on Biomedical Engineering*, vol. 45, no. 1, pp. 98–104, 1998.

[177] G. Huiskamp and F. Greensite, "A new method for myocardial activation imaging," *IEEE Trans Biomed Eng*, vol. 44, no. 6, pp. 433–446, 1997.

[178] Y. Jiang, D. Farina, and O. Dössel, "Localization of the origin of ventricular premature beats by reconstruction of electrical sources using spatio-temporal map-based regularization," in *IFMBE Proc*, vol. 22, 2008, pp. 2511–2514.

[179] J. Coll-Font, B. Erem, P. Štóvíček, et al., "A statistical approach to incorporate multiple ECG or EEG recordings with artifactual variability into inverse solutions," in *Proc ISBI*, 2015, pp. 1053–1056.

[180] R. Martinez Orellana, B. Erem, and D. Brooks, "Time invariant multi electrode averaging for biomedical signals," in *ICASSP*. IEEE, 2013, pp. 1242–1246.

[181] J. Coll-Font, B. Erem, P. Štóvíček, et al., "Using a new time-independent average method for non-invasive cardiac potential imaging of endocardial pacing with imprecise thorax geometry," in *Comput Cardiol*, 2014, pp. 825–828.

[182] A. C. Metting van Rijn, A. Peper, and C. A. Grimbergen, "High-quality recording of bioelectric events. part 2. low-noise, low-power multichannel amplifier design," *Med Biol Eng Comput*, vol. 29, no. 4, pp. 433–440, 1991.

[183] S. Twomey, "On the numerical solution of fredholm integral equations of the first kind by inversion of the linear system produced by quadrature," *J ACM*, vol. 10, no. 1, pp. 79–118, 1963.

[184] H. S. Oster and Y. Rudy, "The use of temporal information in the regularization of the inverse problem of electrocardiography," *IEEE Trans Biomed Eng*, vol. 39, no. 1, pp. 64–75, 1992.

[185] A. Schmidt, C. Azevedo, A. Cheng, et al., "Infarct tissue heterogeneity by magnetic resonance imaging identifies enhanced cardiac arrhythmia susceptibility in patients with left ventricular dysfunction," *Circulation*, vol. 115, no. 15, pp. 2006–2014, 2007.

[186] H. Arevalo, G. Plank, P. Helm, et al., "Tachycardia in post-infarction hearts: insights from 3d image-based ventricular models," *PloS One*, vol. 8, no. 7, p. e68872, 2013.

[187] H. Ashikaga, H. Arevalo, F. Vadakkumpadan, et al., "Feasibility of image-based simulation to estimate ablation target in human ventricular arrhythmia," *Heart Rhythm*, vol. 10, no. 8, pp. 1109–1116, 2013.

[188] J. Ringenberg, M. Deo, D. Filgueiras-Rama, et al., "Effects of fibrosis morphology on reentrant ventricular tachycardia inducibility and simulation fidelity in patient-derived models," *Clinical Med Insights*, vol. 8, no. Suppl 1, p. 1, 2014.

[189] N. Trayanova, P. Boyle, H. Arevalo, et al., "Exploring susceptibility to atrial and ventricular arrhythmias resulting from remodeling of the passive electrical properties in the heart: a simulation approach," vol. 5, no. 435, p. 77, 2014.

[190] J. E. Burnes, B. Taccardi, P. R. Ershler, et al., "Noninvasive electrocardiogram imaging of substrate and intramural ventricular tachycardia in infarcted hearts," *J Am Coll Cardiol*, vol. 38, no. 7, pp. 2071–2078, 2001.

[191] A. Intini, R. N. Goldstein, P. Jia, et al., "Electrocardiographic imaging (ECGI), a novel diagnostic modality used for mapping of focal left ventricular tachycardia in a young athlete," *Heart Rhythm*, vol. 2, pp. 1250–1252, 2005.

[192] Y. Wang, P. S. Cuculich, J. Zhang, et al., "Noninvasive electroanatomic mapping of human ventricular arrhythmias with electrocardiographic imaging," *Sci Transl Med*, vol. 3, p. 98ra84, 2011.

[193] I. Cakulev, J. Sahadevan, M. Arruda, et al., "Confirmation of novel noninvasive high-density electrocardiographic mapping with electrophysiology study implications for therapy," *Circ Arrhythm Electrophysiol*, vol. 6, pp. 68–75, 2013.

[194] T. Oostendorp, J. Nenonen, and P. Korhonen, "Noninvasive determination of the activation sequence of the heart: application to patients with previous myocardial infarctions," *J Electrocardiol*, vol. 35 Suppl, pp. 75–80, 2002.

[195] W. H. W. Schulze, D. Potyagaylo, and O. Dössel, "Activation time imaging in the presence of myocardial ischemia: Choice of initial estimates for iterative solvers," in *Comput Cardiol*, vol. 39, 2012, pp. 961–964.

[196] J. M. De Bakker, F. J. Van Capelle, M. J. Janse, et al., "Slow conduction in the infarcted human heart.'zigzag'course of activation," *Circulation*, vol. 88, no. 3, pp. 915–926, 1993.

[197] W. G. Stevenson, "Ventricular scars and ventricular tachycardia," *Trans Am Clin Climatol Assoc*, vol. 120, p. 403, 2009.

[198] F. Greensite and G. Huiskamp, "An improved method for estimating epicardial potentials from the body surface," *IEEE Trans Biomed Eng*, vol. 45, no. 1, pp. 98–104, 1998.

[199] H. J. J. Wellens, P. Brugada, and W. G. Stevenson, "Programmed electrical stimulation of the heart in patients with life-threatening ventricular arrhythmias: what is the significance of induced arrhythmias and what is the correct stimulaton protocol?" *Circulation*, vol. 72, no. 1, pp. 1–7, 1985.

[200] P. A. Friedman, "Novel mapping techniques for cardiac electrophysiology," *Heart (British Cardiac Society)*, vol. 87, no. 6, pp. 575–582, 2002.

[201] R. J. Schilling, N. S. Peters, and D. W. Davies, "Simultaneous endocardial mapping in the human left ventricle using a noncontact catheter," *Circulation*, vol. 98, pp. 887–898, 1998.

[202] C. C. Gornick, S. W. Adler, B. Pederson, et al., "Validation of a new noncontact catheter system for electroanatomic mapping of left ventricular endocardium," *Circulation*, vol. 1999, pp. 829–835, 1999.

[203] Z. Chen, J. Relan, W. Schulze, et al., "Simultaneous non-contact mapping fused with cmr derived grey zone to explore the relationship with ventricular tachycardia substrate in ischaemic cardiomyopathy," in *J Cardiovasc Magn Res*, vol. 15, no. Suppl 1, 2013, p. P64.

List of Publications and Supervised Theses

Journal Articles

- Walther HW Schulze, Patrick Mackens, **Danila Potyagaylo**, Kawal Rhode, Erol Tülümen, Rainer Schimpf, Theano Papavassiliu, Martin Borggrefe, Olaf Dössel, *Automatic Camera-Based Identification and 3-D Reconstruction of Electrode Positions in Electrocardiographic Imaging*, Biomed Eng / Biomed Technik 2014, 59(6): 515-528
- **Danila Potyagaylo**, Elisenda Gil Cortés, Walther HW Schulze, Olaf Dössel, *Binary Optimization for Source Localization in the Inverse Problem of ECG*, Med Biol Eng Comput 2014, 52(9): 717-728
- Kedar Aras, Wilson Good, Jess Tate, Brett Burton, Dana Brooks, Jaume Coll-Font, Olaf Dössel, Walther HW Schulze, **Danila Potyagaylo**, Linwei Wang, Peter van Dam, Rob MacLeod, *Experimental Data and Geometric Analysis Repository - EDGAR*, J Electrocardiol 2015, 48(6): 975-981
- **Danila Potyagaylo**, Olaf Dössel, Peter van Dam, *Influence of Modeling Errors on the Initial Estimate for Nonlinear Myocardial Activation Times Imaging Calculated with Fastest Route Algorithm*, IEEE Trans Biomed Eng 2016, *Accepted*
- Arno M. Janssen*, **Danila Potyagaylo***, Olaf Dössel, Thom F. Oostendorp, *Assessment of the Equivalent Dipole Layer Source Model in the Reconstruction of Cardiac Activation Times on the Basis of ECGs Produced by an Anisotropic Model of the Heart*, *Submitted*
- Walther HW Schulze, Zhong Chen, Jatin Relan, **Danila Potyagaylo**, Martin W Krueger, Rashed Karim, Manav Sohal, Anoop Shetty, YingLiang Ma, Nicholas Ayache, Maxime Sermesant, Herve Delingette, Julian Bostock, Reza Razavi, Kawal Rhode, Aldo Rinaldi, Olaf Dössel, *ECG Imaging of Ventricular Tachycardia: Evaluation Against Simultaneous Non-Contact Mapping and CMR Derived Grey Zone*, Med Biol Eng Comput, *Major Revisions*

* The first two authors contributed equally to the study.

Refereed Conference Articles

- **Danila Potyagaylo**, Walther HW Schulze, Olaf Dössel, *A New Method for Choosing the Regularization Parameter in the Transmembrane Potential Based Inverse Problem of ECG*, Comput Cardiol 2012, (39):29-32
- **Danila Potyagaylo**, Max Segel, Walther HW Schulze, Olaf Dössel, *Noninvasive Localization of Ectopic Foci: a New Optimization Approach for Simultaneous Reconstruction of Transmembrane Voltages and Epicardial Potentials*, FIMH 2013, 7945: 166-173
- **Danila Potyagaylo**, Walther HW Schulze, Olaf Dössel, *Local Regularization of Endocardial and Epicardial Surfaces for Better Localization of Ectopic Beats in the Inverse Problem of ECG*, Comput Cardiol 2014, (41):837-840
- **Danila Potyagaylo**, Elisenda Gil Cortés, Walther HW Schulze, Olaf Dössel, *Synthesis and Analysis Models for Sparse Signal Reconstruction in the Inverse Problem of ECG*, Biomed Eng / Biomed Technik 2014, (59):941-944
- **Danila Potyagaylo**, Gunnar Seemann, Walther HW Schulze, Olaf Dössel, *Magnetocardiography did not Uncover Electrically Silent Ischemia in an in-silico Study Case*, Comput Cardiol 2015, (42):1145-1148
- Walther HW Schulze, **Danila Potyagaylo**, Olaf Dössel, *Activation Time Imaging in the Presence of Myocardial Ischemia: Choice of Initial Estimates for Iterative Solvers*, Comput Cardiol 2012, (39):961-964
- Walther HW Schulze, Francesc E Henar, **Danila Potyagaylo**, Axel Loewe, Matti Stenroos, Olaf Dössel, *Kalman Filter with Augmented Measurement Model: an ECG Imaging Simulation Study*, FIMH 2013, 7945: 200-207
- Dan-Timon Rudolph, Walther HW Schulze, **Danila Potyagaylo**, Martin W Krueger, Olaf Dössel, *Reconstruction of Atrial Excitation Conduction Velocities and Implementation into the Inverse Problem of Electrocardiography*, Biomed Eng / Biomed Technik 2012, (57):179-182
- Walther HW Schulze, **Danila Potyagaylo**, Biao Wang, Olaf Dössel, *Use of a Tolerance Operator in Wavefront-Based ECG Imaging of Transmembrane Voltages*, IFMBE Proc World Cong Med Phys Biomed Eng 2012, (39):422-425
- Walther HW Schulze, Thomas Fritz, **Danila Potyagaylo**, Julia Trächtler, Rainer Schimpf, Theano Papavassiliu, Erol Tülümen, Boris Rudic, Volker Liebe, Christina Doesch, Martin Borggrefe, Olaf Dössel, *Effect of Mesh Resolution on Forward Calculations of the Electrocardiogram in a Simplified Thorax Model*, Biomed Eng / Biomed Technik 2014, (59):945–948
- Antonia Reinke, **Danila Potyagaylo**, Walther HW Schulze, Olaf Dössel, *Geometrical Model and Corresponding Conductivities for Solving the Inverse Problem of ECG*, Biomed Eng / Biomed Technik 2014, (59):937-940
- Christian Ritter, Walther HW Schulze, **Danila Potyagaylo**, Olaf Dössel, *An Ideally Parameterized Unscented Kalman Filter for the Inverse Problem of Electrocardiography*, Cur Dir Biomed Eng 2015, (1):395-399

- Jaume Coll-Font, **Danila Potyagaylo**, Walther HW Schulze, Olaf Dössel, Dana H Brooks, *Comparison of Temporal Dimensionality Reduction Methods for Constrained Inverse in Cardiac Electrical Imaging*, Comput Cardiol 2015, (41):237-240
- Christian Ritter, Gustavo Lenis, Walther HW Schulze, **Danila Potyagaylo**, Olaf Dössel, *Offset Removal Methods for the Body Surface Potential Map to Improve the ECG Imaging of Ventricular Ectopic Beats*, Biosignalverarbeitung und Magnetische Methoden in der Medizin 2016, (1):1-4

Refereed Conference Abstracts

- **Danila Potyagaylo**, Walther HW Schulze, Olaf Dössel, *Solving the Transmembrane Potential Based Inverse Problem of ECG Under Physiological Constraints on the Solution Range*, Biomed Eng / Biomed Technik 2012
- **Danila Potyagaylo**, Walther HW Schulze, Olaf Dössel, *Local Regularization in the Inverse Problem of Electrocardiography*, Biomed Eng / Biomed Technik 2013
- **Danila Potyagaylo**, Walther HW Schulze, Olaf Dössel, *Predicting the Influence of Electrical Conductivities in Forward ECG Modelling by Taylor-Series Approximation of Potentials using the Finite Element Method*, BaCi 2015
- **Danila Potyagaylo**, Walther HW Schulze, Olaf Dössel, *Method of Fundamental Solutions in the Inverse Problem of ECG*, Biomed Eng / Biomed Technik 2015
- Walther HW Schulze, **Danila Potyagaylo**, Francesc E Henar, Olaf Dössel, *Training of a Kalman Filter with Augmented Measurement Model on Scar Data for Noninvasive Cardiac Imaging*, Biomed Eng / Biomed Technik 2012
- Walther HW Schulze, Rainer Schimpf, Theano Papavassiliu, **Danila Potyagaylo**, Erol Tülümen, Boris Rudic, Volker Liebe, Christina Doesch, Torsten Konrad, Christian Veltmann, Martin Borggrefe, Olaf Dössel, *Electrode Arrangements for ECG Imaging Under Practical Constraints of a Catheter Lab Setting*, Biomed Eng / Biomed Technik 2013
- Walther HW Schulze, **Danila Potyagaylo**, Olaf Dössel, *Predicting the Accuracy of Cardiac Pace Mapping from Lead Field Matrix Characteristics*, Proc Int Cong Electrocardiol 2013
- Rasmus T Jones, Walther HW Schulze, **Danila Potyagaylo**, Olaf Dössel, Frank M Weber, *Computing Lead-Field Matrices for a Body Tissue Conductivity Range*, Biomed Eng / Biomed Technik 2013

Conference Presentations

- **Danila Potyagaylo**, Walther HW Schulze, Olaf Dössel, *Binary Optimization Approach in the TMV-Based Inverse Problem of ECG*, ECG Imaging Workshop, Bad Herrenalb, Germany, 2015

- Walther HW Schulze, **Danila Potyagaylo**, Olaf Dössel, *ECG Imaging - Workflow and Mathematical Concepts*, Integrating Modalities and Scales in Life Science Imaging, Karlsruhe, Germany, 2014
- Walther HW Schulze, **Danila Potyagaylo**, Rainer Schimpf, Martin Borggrefe, Olaf Dössel, *Clinical Validation of ECG Imaging: Ventricular Activity*, ECG Imaging Workshop, Bad Herrenalb, Germany, 2015
- Walther HW Schulze, **Danila Potyagaylo**, Rainer Schimpf, Theano Papavassiliu, Erol Tülümen, Boris Rudic, Volker Liebe, Christina Doesch, Julia Trächtler, Martin Borggrefe, Olaf Dössel, *A Simulation Dataset for ECG Imaging of Paced Beats with Models for Transmural, Endo- and Epicardial and Pericardial Source Imaging*, ECG Imaging Workshop, Bad Herrenalb, Germany, 2015

Reports

Danila Potyagaylo, Thomas Fritz, *Introduction into Numerical Methods for Electromagnetic Field Calculation*, hands-on module for the class "Electromagnetics and Numerical Calculation of Fields", Institute of Biomedical Engineering, Karlsruhe Institute of Technology (KIT), 2014

Supervised Student Theses

First Supervisor

- Vynnie Kong, *ECG Imaging of Surface Transmembrane Voltages Using the Maximum A-Posteriori Method*, Student research project, Massachusetts Institute of Technology (MIT), 2014
- A. Reinke, *Regularization Parameter Estimation for the Inverse Problem of ECG*, Bachelor's thesis, Institute of Biomedical Engineering, Karlsruhe Institute of Technology (KIT), 2013
- E. Gil Cortés, *Spatio-Temporal Optimization Approaches to the Transmembrane Potential Based Inverse Problem of ECG*, Master's thesis, Universitat Politècnica de Catalunya / KIT, 2013
- M. Segel, *Improving ECG Imaging: Combined Regularization in Extracellular Space and the Space of Transmembrane Voltages*, Bachelor's thesis, Karlsruhe Institute of Technology (KIT), 2013

Second Supervisor

- C. Ritter, *Imposition of Dynamic Model Based Regularization on the Solution in ECG Imaging*, Bachelor's thesis, Institute of Biomedical Engineering, Karlsruhe Institute of Technology (KIT), 2013

- E. R. Khaled Fattoh, *Solving the inverse problem of ECG for realistic atrial excitation propagation*, Student research project, Cairo University, 2013
- R. Jones, *Towards a Personalized Volume Conductor Parameterization in ECG Imaging*, Bachelor's thesis, Institute of Biomedical Engineering, Karlsruhe Institute of Technology (KIT), 2013
- K. Vogel, *Wavefront-Preserving Regularization in Noninvasive Electrocardiographic Imaging of Ventricular Extrasystoles*, Student research project, Massachusetts Institute of Technology (MIT), 2012
- P. Mackens, *3D Reconstruction of ECG Electrode Positions from Multiple Photographic Images*, Bachelor's thesis, Institute of Biomedical Engineering, Karlsruhe Institute of Technology (KIT), 2012
- D.-T. Rudolph, *Non-Invasive Imaging of Cardiac Excitation Conduction Velocities*, Bachelor's thesis, Institute of Biomedical Engineering, Karlsruhe Institute of Technology (KIT), 2012

Awards & Grants

- Best Poster Award Computing in Cardiology 2012 for
- Networking Scholarship, Karlsruhe House of Young Scientists (KHYS), 2014